

ADVANCED MORPHOMETRY OF MESIOTEMPORAL STRUCTURES IN TEMPORAL LOBE EPILEPSY

Hosung Kim
Department of Biomedical Engineering
McGill University, Montreal, Canada

August 2011

A thesis submitted to McGill University
in partial fulfillment of the requirements for the degree of Doctor of Philosophy

© Hosung Kim, 2011

To

Dearest Hey Jin, Daniel, Rachel, my parents and parents-in-law

가장 사랑하는 아내 혜진과 보석 같은 다니엘과 다혜, 그리고 물심양면으로
도우신 부모님과 장인장모님에게 바칩니다.

Acknowledgements

First and above all, I praise God, the almighty for the wisdom and perseverance that He has bestowed upon me during my Ph.D. project, and indeed, throughout my life: "*I can do everything through him who gives me strength.*" (Philippians 4: 13). I also thank Him for providing me this opportunity and granting me the capability to proceed successfully.

This Thesis appears in its current form due to the assistance and guidance of several people. I would therefore like to show my sincere thanks to all of them.

I have been indebted in the completion of my Ph.D. project and this Thesis to Dr. Neda Ladbon-Bernasconi and Andrea Bernasconi. I am deeply grateful to them for their patience, warmth, kind and insightful advices, generous supports in all aspects of life. They are truly a role model as supervisors by showing the best way to conduct wise studies and to write manuscripts, as well as to take care of students with sincere affection.

I thank my co-supervisor Dr. Alan Evans for his guidance, support, encouragement and good humour. He has inspired me and given me insightful technical advice.

My committee member Dr. Bruce Pike provided wise and generous advice to improve the quality of this work.

Many thanks to my colleagues and friends from the laboratory for their countless discussions and friendships: Boris Bernhardt, Thomas Mansi, Daisuke Nakajima, Linda Horwood, Seok-Jun Hong, Mark Keezer, Denis Rivière, Jessie Kulaga-Yoskovitch, Pierre Besson, Luis Concha, Olivier Colliot, Dewi Schrader, and Natalie Voets. Further thanks to the superb scientists and friends in the Brain

Imaging Centre (BIC) and the Montreal Neurological Institute, who directly and indirectly encouraged this Thesis and endeavour to make an extraordinary working environment for neuroimaging in the BIC: Budhachandra Khundrakpam, Cedric Clochoux, Claude Lepage, Gaolang Gong, Jean-François Malouin, Jahyun Koo, Junki Lee, June Sik Kim, Kevin Larcher, Louis Collins, Natalya Portman, Nicolas Guizard, Oliver Lyttelton, Pedro Rosa-Neto, Reza Adalat, Sylvain Milot, Uichel Yoon, Vladimir Fonov, Yong He, and Zhang Chen. Among them, I especially thank Denis for helping me to translate the abstract of this Thesis into French.

I also would like to thank the administrative staff of the MNI for lending a helping hand whenever needed: Anna Stabile, Jennifer Chew, Pina Sorrini, Nancy Abate, and Zia Jacob Merchant.

Rev. Timothy Hwang and Rev. Seong Soo Kim who have ceaselessly supported and prayed for me and my family deserve my gratitude.

The biggest appreciation goes to my family who have been a constant source of support – emotional, moral and financial – during my postgraduate years, and this Thesis would certainly not have existed without them: My beloved Hye Jin, Daniel and Rachel, my parents and parents-in-law, my only brother Shin-chul, my sisters-in-law, Hyun Jin and Hyo Jin. I give special thanks to my mother-in-law, Mrs. Chung-Gum Kim who has overcome her battle with uterine cancer and visited Montreal to help me and my wife take care of our children during the busiest time of my Ph.D.

Contributions of Authors

I'm the first author of all five manuscripts included in this Thesis. In a close collaboration with my PhD supervisors **Dr. Andrea Bernasconi** and **Dr. Alan Evans**, I have performed all of the data analysis. In particular, I participated to the conceptual design of all studies, performed all stages of software design and development, image processing, quality control, statistical analysis, visualization, and actively contributed to the interpretation of results.

The following list summarizes the contributions of the other co-authors situated.

1. **Neda Ladbon-Bernasconi**. Played a pivotal role in the conceptual design, statistical analysis and interpretation of findings for all experiments included in this Thesis. She also provided manual labels of mesiotemporal structures that were used in Manuscript 1, 2, 4 and 5. She assisted in the preparing and the analysis of the clinical information, and was instrumental in the interpretation of findings in all experiments.
2. **Tommaso Mansi**. *Image Analytics and Informatics, Princeton, NJ, USA*. Provided advice on development of surface-based Jacobian determinant and mean medial axis in Manuscript 1, and surface-based multi-template segmentation in Manuscript 5. He also aided in interpretation of results in Manuscript 1 and 5.
3. **Boris C Bernhardt**. Provided advice on the design of statistical analysis and the interpretation of results in Manuscript 2 and 4. Provided matlab scripts to facilitate statistical analyses in Manuscript 2, independently classified the pattern of sulcal morphology to assess inter-rater agreement in Manuscript 3.

4. **Marie Chupin.** *Université Pierre et Marie Curie-Paris 6, CNRS, UMR-S7225, Paris, France.* Provided SACHA, an automatic hippocampal segmentation algorithm for the evaluation of automated segmentation accuracy in Manuscript 4. Aided in interpretation of results in Manuscript 4.
5. **Olivier Colliot.** *Université Pierre et Marie Curie-Paris 6, CNRS, UMR-S7225, Paris, France.* Aided in interpretation of results in Manuscript 4.

Related Publications

Articles in Peer-reviewed Journals

a. Published

1. [H. Kim](#), N. Bernasconi, B.C. Bernhardt, O. Colliot and A. Bernasconi (2008). Temporal lobe epilepsy is associated with a single-branch collateral sulcus. *Neurology* 70(22 Pt 2): 2159-65.
2. [H. Kim](#), P. Besson, O. Colliot, A. Bernasconi, N. Bernasconi (2008). Surface-based vector analysis using heat equation interpolation: a new approach to quantify local hippocampal volume changes, *Med. Image. Comp. Comp. Assist. Interv.* 5241(Pt 1)
3. T. Sankar, N. Bernasconi, [H. Kim](#), A. Bernasconi (2008). Temporal lobe epilepsy: Differential pattern of damage in temporopolar cortex and white matter, *Human Brain Mapping* 29(8).
4. B.C. Bernhardt, K.J. Worsley, [H. Kim](#), A.C. Evans, A. Bernasconi, N. Bernasconi (2009). Longitudinal and cross-sectional analysis of atrophy in pharmaco-resistant temporal lobe epilepsy. *Neurology* 72(20): 1747-54.
5. E. Gerardin, G. Chételat, M. Chupin, R. Cuingnet, B. Desgranges, [H.S. Kim](#), M. Niethammer, B. Dubois, L. Garnero, S. Lehericy, F. Eustache, O. Colliot, The ADNI, (2009). Multidimensional classification of hippocampal shape features discriminates Alzheimer's disease and mild cognitive impairment from normal aging, *Neuroimage* 47(4).
6. [H. Kim](#), T. Mansi, A. Bernasconi, N. Bernasconi (2011). Vertex wise shape analysis of the hippocampus: disentangling positional differences from volume changes, *Med. Image. Comp. Comp. Assist. Interv.* 6892(Pt 2).
7. [H. Kim](#), T. Mansi, N. Bernasconi, A. Bernasconi (2011). Robust Surface-Based Multi-Template Automated Algorithm to Segment Healthy and Pathological Hippocampi, *Med. Image. Comp. Comp. Assist. Interv.* 6893(Pt 3).
8. N.L. Voets, B.C. Bernhardt, [H. Kim](#), U. Yoon, N. Bernasconi (2011). Increased temporo-limbic cortical folding complexity in temporal lobe pilepsy. *Neurology* 76(2)

9. H. Kim, M. Chupin, B.C. Bernhardt, N. Bernasconi, O. Colliot, A. Bernasconi. The impact of developmental abnormalities on Automatic hippocampal segmentation in temporal lobe epilepsy, *Neuroimage* (in press).

b. Submitted

10. H. Kim, T. Mansi, A. Bernasconi, N. Bernasconi. Surface-based multi-template automated algorithm to segment hippocampi without impact of malrotation, *Neuroimage*
11. H. Kim, T. Mansi, N. Bernasconi, A. Bernasconi. Surface-based shape analysis of the hippocampus: disentangling positional differences from volume changes, *Neuroimage*
12. BC Bernhardt, H. Kim, N. Bernasconi, A. Bernasconi. Mapping thalamo-cortical network pathology in temporal lobe epilepsy, *Neurology*

c. Manuscript in preparation

13. H. Kim, B.C. Bernhardt, N. Voets, A. Bernasconi, N. Bernasconi. Patterns of mesiotemporal subfield pathology in temporal lobe epilepsy: dynamics and relation to surgical outcome

Abstracts

a. Published

1. H. Kim, O. Colliot, N. Bernasconi, and A. Bernasconi (2006). Quantitative Analysis of Shape and Positioning of the Hippocampal Formation in Temporal Lobe Epilepsy. 60th Annual Meeting of the American Epilepsy Society, Boston, MA, USA.
2. B.C. Bernhardt, H. Kim, U. Yoon, N. Bernasconi, A. Bernasconi (2008). TLE is associated with reduced folding of the temporal neocortex. ISMRM 16th scientific meeting and exhibition, Toronto, Canada, May 2008.
3. H. Kim, M. Niethammer, B. C. Bernhardt, S. Bouix, N. Bernasconi, and A. Bernasconi (2008). SPHARM detects hippocampal subfield pathology in temporal lobe epilepsy. ISMRM 16th scientific meeting and exhibition, Toronto, Canada

4. L. Concha, H. Kim, B.C. Bernhardt, N. Bernasconi (2009). Spatial localization of diffusion abnormalities along DTI tracts in temporal lobe epilepsy. MICCAI Workshop, London.
5. L. Concha, H. Kim, B.C. Bernhardt, N. Bernasconi (2009). Distance based analysis of DTI Tractography: Evidence for Focal Pathology in Temporal Lobe Epilepsy. 63rd Annual Meeting of the American Epilepsy Society, Boston, MA, USA.
6. B.C. Bernhardt, H. Kim, J. Natsume, A. Bernasconi (2009). Mapping thalamic nuclear pathology in temporal lobe epilepsy. 63rd Annual Meeting of the American Epilepsy Society, Boston, MA, USA.
7. A. Bernasconi, B.C. Bernhardt, H. Kim, J. Natsume, N. Bernasconi (2009). Idiopathic generalized epilepsy is associated with atrophy in pulvinar and somatomotor thalamic nuclei. 28th International Epilepsy Congress, Budapest, Hungary
8. B.C. Bernhardt, H. Kim, J. Natsume, N. Bernasconi, A. Bernasconi (2009). Temporal lobe epilepsy is associated with atrophy of limbic thalamic nuclei. 15th Annual Meeting of Human Brain Mapping, San Francisco, California
9. S. Hong, B.C. Bernhardt, H. Kim, N. Bernasconi and A. Bernasconi (2011). MRI-Based Cortical Thickness Analysis in Drug-Resistant Cryptogenic Epilepsy, 17th Annual Meeting of Human Brain Mapping, Quebec city, Canada.
10. B.C. Bernhardt, S.J. Hong, H. Kim, A. Bernasconi, N. Bernasconi (2011). Diffusion abnormalities of fiber tracts underlying cortical regions in temporal lobe epilepsy, 17th Annual Meeting of Human Brain Mapping, Quebec city, Canada.
11. D. Riviere, B.C. Bernhardt, H. Kim, S.J. Hong, M. Perrot, J.F. Mangin, J. Regis, N. Bernasconi, A. Bernasconi (2011). Diffuse sulcal anomalies associated with focal epileptogenic malformations of cortical development, 17th Annual Meeting of Human Brain Mapping, Quebec city, Canada.
12. H. Kim, B.C. Bernhardt, J. Natsume, N. Bernasconi (2011). Mapping thalamic pathology in idiopathic generalized epilepsy and temporal lobe epilepsy, 64th Annual Meeting of the American Epilepsy Society, San Antonio, TX, USA. *Winner of Young Investigator Travel Award of the American Epilepsy Society*
13. H. Kim, T. Mansi, S. Hong, A. Bernasconi, N. Bernasconi (2011). Robust automatic hippocampal segmentation in temporal lobe epilepsy, 65th Annual Meeting of the American Epilepsy Society

14. S. Hong, H. Kim, M. Chupin, O. Colliot, N. Bernasconi, A. Bernasconi (2011). Automatic hippocampal segmentations in temporal lobe epilepsy perform poorer in the presence of developmental abnormalities, 65th Annual Meeting of the American Epilepsy Society
15. M.R. Keezer, H. Kim, B.C. Bernhardt, A. Bernasconi, N. Bernasconi (2011), Shape analysis in temporal lobe epilepsy with amygdalar enlargement, 65th Annual Meeting of the American Epilepsy Society, Baltimore, MD, USA. *Winner of Young Investigator Travel Award of the American Epilepsy Society*

Abstract

Background. Temporal lobe epilepsy (TLE) is the most common drug-resistant epilepsy in adults. While TLE is typically associated with mesiotemporal atrophy on MRI, hippocampal volumes are normal in 30% of patients. Moreover, there is growing evidence that developmental abnormalities altering hippocampal morphology as well as inferiotemporal sulco-gyral patterns participate in the pathogenesis of this condition. Indeed, about 40% of TLE patients show atypical shape and positioning of the hippocampus and collateral sulcus, commonly referred to as malrotation. To date, morphometric analysis of the mesiotemporal lobe pathology in TLE has been limited to MR volumetry.

Objectives. The overall goal of this Thesis was to develop advanced morphometric methods to statistically model aspects of pathology that have not been previously assessed on MRI and that are not evident in measurement of total volume. We first developed surface-based techniques that independently quantify small-scale focal atrophy, positional changes and sulcal variants, and investigated their clinical significance. We then quantitatively evaluated the impact of these morphological features (*i.e.*, atrophy and developmental shape and positioning anomalies) on the performance of state-of-the-art hippocampal segmentation algorithms. Lastly, we developed a novel hippocampal segmentation method based on a multi-template approach that relies on statistical parametric surface models and locoregional texture features.

Methods. We carried out the following experiments: 1) After extracting the spherical harmonics combined with point distribution models (SPHARM-PDM) from manual hippocampal labels, we computed displacement vectors between

individual surfaces and the template. Then, we computed surface-based Jacobian determinants (SJD) from these vectors to localize volume changes. To analyze positional variants, we constructed a mean meridian axis (MEMAX), inheriting the shape-constrained point correspondences of SPHARM, on which we compute local curvatures and position vectors. We validated our method on synthetic shapes. 2) Using the metrics developed in (1), we investigated patterns of mesiotemporal pathology in TLE, by performing point-wise group comparisons between patients with hippocampal atrophy (TLE-HA), those with normal hippocampal volume (TLE-NV), and healthy controls. In addition, we assessed the yield of our 3D surface-based shape modeling to lateralize the seizure focus and predict seizure outcome after surgery. 3) Brain sulci were automatically identified and labeled on MRI using a congregation of neural networks. 3D sulcal models mapped on the cortical surface were inspected visually. We used four sulcal patterns classes to describe the sulcal arrangement in the inferior surface of the temporal lobe. 4) We segmented the hippocampus in controls and TLE patients using SACHA, a region-growing algorithm constrained by anatomical priors, and FreeSurfer, a freely available atlas-based software. To quantify malrotation, 3D models were created from manual hippocampal labels and automatically extracted collateral sulci. Segmentation accuracy of automated techniques was evaluated relative to manual labeling using the Dice similarity index and surface-based shape mapping, for which we computed vertex-wise displacement vectors between automated and manual segmentations. We then correlated segmentation accuracy with malrotation features and atrophy. 5) We developed a novel segmentation algorithm (SurfMulti) to statistically estimate locoregional texture and shape using a surface-based approach that guarantees shape-inherent point-wise correspondences. To account for inter-subject variability, including shape variants, we used a multi-template library derived from a large database of controls and patients. We compared the performance of SurfMulti to SACHA and FreeSurfer and against manual labeling.

Results. We were able to unambiguously disentangle local volume from positional changes by quantifying independently both morphological

characteristics. Our analysis showed that in TLE patients atrophy and positional changes co-occurred at the level of the posterior hippocampus. Compared to standard volumetry, our technique showed increased sensitivity by unveiling subtle ipsilateral hippocampal atrophy in TLE-NV, ipsilateral amygdalar and contralateral hippocampal and entorhinal pathology in both TLE groups. A combined surface-based analysis of all three mesiotemporal lobe structures correctly lateralized the seizure focus in 94% of patients with TLE-NV, as opposed to 73% using standard volumetry. 3D analysis of basal temporal sulcal morphology revealed that the majority of TLE patients exhibit a single-branch, unbroken long collateral sulcus as compared to healthy control subjects. With respect to the influence of morphological anomalies on the performance of automated techniques, we found that SACHA overestimated the volume of the lateral convexity of the hippocampus in cases with malrotation, but behaved relatively well in the presence of atrophy. The performance of FreeSurfer, on the other hand, was affected by both hippocampal malrotation and atrophy. We also found that the automated procedures detected smaller effect sizes of hippocampal atrophy and tended to be less accurate for seizure focus lateralization compared to manual volumetry. Our proposed hippocampal segmentation method integrating deformable parametric surfaces and multiple templates in a unified framework achieved a level of accuracy in TLE patients virtually identical to healthy controls, with a Dice index of 86.1%. Such performance has not yet been paralleled in epilepsy. Vertex-wise surface-based shape mapping showed that SurfMulti with adaptive weight had an excellent overlap with manual labels, with sub-millimetric precision. Furthermore, we achieved the same sensitivity than manual volumetry in detecting atrophy ipsilateral to the seizure focus.

Significance. The analytical framework we developed is intended to substantially improve MRI analysis so that it can fulfill its role for surgical target localization and post-surgical outcome prediction, the two main challenges of contemporary epilepsy surgery. Our results show that a better understanding of mesiotemporal lobe pathology lies in the evaluation of various brain

morphological characteristics. By statistically modeling and localizing aspects of mesiotemporal pathology related to atrophy, positional changes and sulcal variants across the spectrum of drug-resistant TLE, we showed the ability of advanced post-processing of anatomical MRI to unveil anomalies not otherwise detected on visual evaluation or volumetric analysis. The developed methodology and techniques can be extended to assess structural changes in neurological and neuropsychiatric disorders in which the temporal lobe is involved.

Résumé

Contexte. L'épilepsie du lobe temporal (ELT) est l'épilepsie pharmaco-résistante la plus commune chez l'adulte. Généralement associée à une atrophie temporo-mésiale visible par IRM, les volumes hippocampiques sont pourtant normaux dans 30% des cas d'ELT. De plus, il y a de plus en plus d'indices montrant que des anomalies du développement, qui altèrent la morphologie hippocampique et les motifs sulco-gyreaux temporo-mésiaux, participent à la pathogénèse de cette épilepsie. En effet, 40% des ELT exhibent une forme et un positionnement atypiques de l'hippocampe et du sillon collatéral, effet communément appelé "malrotation". Jusqu'à présent, l'analyse morphométrique de la pathologie ELT du lobe mésiotemporal s'est limitée à de la volumétrie sur IRM.

Objectifs. Le but général de cette thèse a été le développement de méthodes de morphométrie avancées qui permettront de modéliser statistiquement des aspects de la pathologie qui n'ont pas été évalués antérieurement par IRM, et qui n'apparaissent pas de manière évidente par des mesures de volume total. Nous avons tout d'abord développé des techniques surfaciques qui quantifient, indépendamment, des atrophies focales de petite étendue, des écarts de position ainsi que des variantes de formes de sillons, et nous avons étudié leur significativité clinique. Nous avons ensuite évalué quantitativement l'impact de ces caractéristiques morphologiques (l'atrophie et les anomalies développementales de forme et de position) sur la performance des algorithmes de segmentation de l'hippocampe les plus avancés du moment. Enfin, nous avons développé une nouvelle méthode de segmentation de l'hippocampe basée sur une approche de type "multi-templates" (modèles multiples), qui s'appuie sur des modèles statistiques paramétriques surfaciques et des caractéristiques locorégionales de textures.

Méthodes. Nous avons réalisé les expériences suivantes: 1) Après avoir extrait les harmoniques sphériques combinées à des modèles de distribution de points (SPHARM-PDM) à partir de segmentations hippocampiques manuelles, nous avons calculé des vecteurs de déplacement entre les surfaces individuelles et le modèle. Nous avons alors calculé des déterminants jacobiens surfaciques (SJD, Surface-based Jacobian Determinants) à partir de ces vecteurs afin de localiser des changements de volume. Pour analyser les différences de position, nous avons construit un axe méridien médian (MEMAX), qui reprend les correspondances de points, contraintes par la forme, de SPHARM, et sur lequel les courbures locales et les vecteurs de positions sont calculés. Notre méthode a été validée sur des formes synthétiques. 2) A l'aide des métriques développées en (1), nous avons étudié les motifs de pathologie mésiotemporale chez les patients ELT, en effectuant des comparaisons de groupes, point à point, entre des patients atteints d'une atrophie hippocampique (TLE-HA), ceux dont le volume hippocampique est normal (TLE-NV), et des contrôles sains. De plus, nous avons évalué la capacité de notre modélisation de formes surfacique 3D à latéraliser le foyer épileptogène et à prédire l'issue de la chirurgie. 3) Les sillons corticaux ont été automatiquement extraits et identifiés à partir d'images IRM grâce à un modèle utilisant une assemblée de réseaux neuronaux artificiels. Nous avons inspecté visuellement en 3D les arrangements sulcaux de la face inférieure du lobe temporal, et les avons décrits en quatre classes de motifs. 4) Nous avons segmenté l'hippocampe des sujets contrôle et des patients ELT en utilisant SACHA, un algorithme de croissance de région contraint par des a priori anatomiques, et FreeSurfer, un logiciel libre se basant sur un atlas. Pour quantifier les malrotations, des modèles 3D ont été créés à partir des segmentations manuelles d'hippocampes et des sillons collatéraux extraits automatiquement. La précision de la segmentation de l'hippocampe par les techniques automatiques a été évaluée en comparaison à la segmentation manuelle, en utilisant l'indice de similarité de Dice, ainsi qu'une analyse surfacique de formes, pour laquelle nous avons calculé noeud par noeud des vecteurs de déplacement entre les segmentations automatiques et manuelles.

Nous avons ensuite corrélé la précision des segmentations aux caractéristiques de malrotation et d'atrophie. 5) Nous avons développé un nouvel algorithme de segmentation (SurfMulti) qui estime statistiquement la texture locorégionale et la forme, à l'aide d'une approche surfacique qui garantit des correspondances point à point basées sur les formes. Pour prendre en compte la variabilité inter-individuelle, y compris les variantes de formes, nous avons utilisé une bibliothèque de modèles multiples établie à partir d'une large base de données de sujets contrôles et de patients. Nous avons comparé la performance de SurfMulti à celles de SACHA et de FreeSurfer, ainsi qu'aux segmentations manuelles.

Résultats. Nous avons pu clairement dissocier les changements du volume local des changements de position en quantifiant indépendamment ces deux caractéristiques morphologiques. Notre analyse a montré que chez les patients ELT, une atrophie et des changements de position existent conjointement, au niveau postérieur de l'hippocampe. En comparaison à la volumétrie classique, notre technique a montré une meilleure sensibilité en dévoilant des atrophies ipsilatérales subtiles chez les sujets TLE-NV, des pathologies amygdalaires ipsilatérales ainsi qu'hippocampiques controlatérales, et entorhinales, dans les deux groupes de patients ELT. Une analyse surfacique combinée des trois structures du lobe temporo-mésial ont pu latéraliser le foyer des crises chez 94% des patients ELT-NV, contre 73% en utilisant la volumétrie classique. L'analyse 3D de la morphologie sulcale du lobe temporal basal a révélé que la majorité des patients ELT présentent un sillon collatéral ininterrompu, d'une seule longue branche, contrairement à de nombreux sujets sains. Concernant l'influence des anomalies morphologiques sur la performance des techniques automatiques, nous avons observé que SACHA surestime le volume de la convexité latérale de l'hippocampe dans les cas de malrotation, mais se comporte relativement bien en présence d'atrophies. L'efficacité de FreeSurfer est en revanche affectée à la fois par la malrotation de l'hippocampe et par l'atrophie. Nous avons également observé que les procédures automatiques affichent de plus faibles effets d'atrophie hippocampique et ont tendance à être moins précis pour latéraliser les

foyers des crises que la volumétrie manuelle. La méthode de segmentation hippocampique que nous proposons, qui intègre des surfaces paramétriques déformables et des modèles multiples dans un cadre unifié, obtient un niveau d'efficacité pratiquement identique chez les patients ELT et chez les sujets contrôles, avec un indice Dice de 86,1%. Une telle performance n'a jamais été égalée en épilepsie. L'analyse de forme surfacique au niveau des noeuds a révélé que SurfMulti avec une pondération adaptative obtenait un excellent recouvrement avec les segmentations manuelles, d'une précision plus fine que le millimètre. De plus, nous obtenons la même sensibilité que la volumétrie manuelle pour la détection d'atrophies ipsilatérales au foyer épileptogène.

Significativité. Le cadre d'analyse que nous avons développé a pour but d'améliorer sensiblement l'analyse des IRM de manière à permettre son application à la localisation de cibles pour la chirurgie ainsi que pour la prédiction des conséquences post-chirurgicales. Ces applications constituent les deux principaux défis de la chirurgie de l'épilepsie contemporaine. Les résultats montrent qu'une meilleure compréhension des pathologies du lobe temporo-mésial passe par l'évaluation de plusieurs caractéristiques morphologiques du cerveau. En modélisant statistiquement et en localisant divers aspects de la pathologie mésiotemporale reliés à l'atrophie, les changements de positions ainsi que les variantes sulcales, pour tout le spectre des ELT pharmaco-résistantes, nous avons montré que le post-traitement des IRM anatomiques est capable de dévoiler des anomalies qui ne sont pas détectées par l'analyse visuelle ou par l'analyse volumétrique. La méthodologie et les techniques développées pourront être étendues pour évaluer les changements structurels liés aux troubles neurologiques et neuropsychiatriques dans lesquels le lobe temporal est impliqué.

Original Contributions

Manuscript 1. Developing a surface-based framework to analyze independently volume and positioning using vertex-wise Jacobian determinants and a mean meridian axis (MEMAX), inheriting the shape-constrained point correspondences of SPHARM on which we compute local curvatures and position vectors.

Manuscript 2. Investigating *in vivo* static and dynamic patterns of mesiotemporal subfield pathology in TLE using 3D surface-based shape modeling. Performing linear regressions to assess the relation between vertex-wise volume changes and clinical parameters including post-surgical outcome. Performing seizure-focus lateralization in TLE based on the local asymmetrical atrophy of the mesiotemporal structures and an unbiased choice of a statistical threshold.

Manuscript 3. Classifying the morphological patterns of the collateral sulcus in TLE and healthy controls using an automated sulcal extraction method allowing the description of sulcal variability on brain surfaces on MRI.

Manuscript 4. Evaluating the impact of hippocampal malrotation and atrophy on the performance of automated segmentations. Localizing segmentation errors attributed to hippocampal malrotation using surface-based shape mapping based on spherical harmonic description and vertex-wise linear regression models.

Manuscript 5. Developing a novel hippocampal segmentation method to statistically estimate locoregional texture and shape using a surface-based multi-template approach that guarantees shape-inherent point-wise correspondences. Constructing a template library derived from a large database of controls and patients to account for inter-subject variability, including shape variants.

Table of Contents

Acknowledgements	3
Contributions of Authors	5
Related Publications	7
Abstract	11
Résumé	15
Original Contributions	19
Table of Contents	20
List of Figures	22
List of Tables	24
Chapter 1	27
Introduction	27
Chapter 2	31
Background	31
2.1 Epidemiology of temporal lobe epilepsy	31
2.2 Pathology and electrophysiology in temporal lobe epilepsy	32
2.3 Mesiotemporal lobe structures on MRI: morphological changes in TLE	34
2.3.1 <i>Quantitative MRI of mesiotemporal sclerosis</i>	35
2.3.2 <i>Hippocampal malrotation: a biological marker of developmental abnormalities</i> ..	38
2.4 Computational models of abnormal morphology	39
2.4.1 <i>Voxel-based morphometry</i>	40
2.4.2 <i>Deformation-based morphometry</i>	41
2.4.3 <i>Surface-based approaches</i>	43
2.4.4 <i>Descriptive models</i>	47
2.5 Performance of automated segmentation in healthy and pathological hippocampi	47
2.5.1 <i>Categorization of automatic segmentations</i>	48
2.5.2 <i>Multi-template based segmentation to statistically model shape variants</i>	51
2.5.3 <i>Performance in healthy hippocampi</i>	52
2.5.4 <i>Performance in pathological hippocampi</i>	54
Chapter 3	57
Quantitative analysis of morphological changes in mesiotemporal lobe structures using computational models	57

3.1 Unified preface	57
3.2 Manuscript 1	60
Abstract	61
Introduction	62
Methods	63
Experiments and Results	73
Discussion	79
3.3 Manuscript 2	83
Abstract	84
Introduction	85
Methods	86
Results	93
Discussion	100
3.4 Manuscript 3	105
Abstract	106
Introduction	107
Methods	109
Results	115
Discussion	117
Chapter 4	123
Assessment of the impact of morphological abnormalities on automatic hippocampal segmentation in TLE	123
4.1 Preface	123
4.2 Manuscript 4	125
Abstract	126
Introduction	128
Methods	129
Results	137
Discussion	145
Chapter 5	148
Automatic segmentation of hippocampal structures in TLE	148
5.1 Preface	148
5.2 Manuscript 5	150
Abstract	151
Introduction	152
Methods	154
Experiments and Results	160
Discussion	170
Chapter 6	173
Summary and Conclusions	173
Bibliography	177

List of Figures

Figure 2.1. Anatomy of the mesiotemporal structures.	35
Figure 2.2. MRI of a healthy subject and a patient with hippocampal sclerosis	36
Figure 2.3. Morphological characteristics of malrotation on MRI	38
Figure 2.4. Longitudinal DBM.	43
Figure 2.5. Displacement vector analysis.	46
Figure 3.1. Heat equation surface-to-volume interpolation on discrete space ...	67
Figure 3.2. Modeling mean meridian axis	71
Figure 3.3. Analysis of synthetic data.	73
Figure 3.4. Graphs displaying the relationship between the grid size of the heat equation interpolation and the sensitivity in detecting atrophy.....	75
Figure 3.5. Relationship between sampling points along MEMAX and sensitivity in detecting shifting and bending in TLE patients	76
Figure 3.6. Group comparisons between TLE and healthy controls	78
Figure 3.7. Group comparisons between heterotopia and healthy controls.	79
Figure 3.8. Cross-sectional vertex-wise analysis in TLE with hippocampal atrophy.	94
Figure 3.9. Cross-sectional vertex-wise analysis in TLE with normal hippocampal volume.....	95
Figure 3.10. Longitudinal analysis of standard volumetry	96
Figure 3.11. Longitudinal vertex-wise analysis.	97
Figure 3.12. Predictors of post-surgical outcome.....	98
Figure 3.13. Seizure focus lateralization in TLE patients with normal hippocampal volume.	99
Figure 3.14. 3D surface rendering and coronal MRI slices of the basal temporal lobe.	112

Figure 3.15. Basal view of the 3D MRI rendering of the brain with sulci mapped on the cortical surface.	113
Figure 4.1. Models of hippocampal malrotation	134
Figure 4.2. Correlation between manual and automated segmentation.....	137
Figure 4.3. Shape differences between manual and automated tracings	140
Figure 4.4. Surface-based analysis of contour accuracy	141
Figure 4.5. Impact of hippocampal malrotation on SACHA.....	142
Figure 4.6. Seizure focus lateralization in TLE.....	144
Figure 5.1. Flowchart of SurfMulti	154
Figure 5.2. Contribution of texture and shape features to SurfMulti segmentation performance.	165
Figure 5.3. Shape analysis of automated segmentation algorithms.....	167
Figure 5.4. Examples of the automated segmentation algorithms	168

List of Tables

Table 2.1. Performance of automatic hippocampal segmentations in healthy subjects	53
Table 2.2. Performance of automatic hippocampal segmentations in neurological disorders.....	56
Table 3.1. Demographic and clinical data of the cross-sectional cohort.....	88
Table 3.2. Demographic and clinical data of the longitudinal cohort.	89
Table 3.3. Volumetry of mesiotemporal structures in TLE.....	93
Table 3.4. Frequencies of sulcal patterns types in the basal temporal lobe in healthy normal controls and patients with temporal lobe epilepsy.....	116
Table 3.5. Proportion of patients with childhood febrile seizures and shape and positioning changes of the hippocampal formation for each sulcal pattern.	116
Table 4.1. Prevalence of hippocampal malrotation based on a 2 standard deviation cutoff from the distribution of healthy controls.....	135
Table 4.2. Evaluation of automated segmentation methods using Dice similarity index.....	138
Table 4.3. Correlations between automatic segmentation accuracy and hippocampal volume/malrotation features.....	139
Table 5.1. Prevalence of hippocampal malrotation in healthy controls and patients.....	164
Table 5.2. Segmentation accuracy as defined by Dice index (% mean \pm SD)...	164
Table 5.3. Hippocampal volumetry.....	166
Table 5.4. Association between automatic segmentation accuracy and hippocampal volume / malrotation features.....	169

Abbreviations

AM	Amygdala
CA	Cornu Ammonis
CS	Collateral sulcus
DG	Dentate gyrus
CSF	Cerebro-spinal fluid
DBM	Deformation-based morphometry
EC	Entorhinal cortex
EEG	Electroencephalography
FC	Febrile convulsions
FCD	Focal cortical dysplasia
FDR	False discovery rate
FOV	Field of view
GM	Gray matter
HET	Heterotopia
HF	Hippocampal formation
HS	Hippocampal sclerosis
ICBM	International consortium for brain mapping
MCD	Malformations of cortical development
MEMAX	Mean meridian axis
MRI	Magnetic resonance imaging
MTS	Mesiotemporal sclerosis
NEX	Number of images averaged
NSF	Non-seizure free patients after surgery
LTLE	Left temporal lobe epilepsy
NC	Normal healthy controls
Ns	Number of sample points
OTS	Occipitotemporal sulcus
PCA	Principal component analysis

PMG	Polymicrogyria
RS	Rhinal sulcus
ROI	Region of interest
RTLE	Right temporal lobe epilepsy
SD	Standard deviation
SF	Seizure free patients after surgery
SJD	Surface-based Jacobian determinant
SNV	Surface normal component of displacement vector
SPAM	Probabilistic spatial mapping
SPHARM-PDM	Spherical harmonic description and point-distribution Models
SurfMulti	Automatic segmentation using surface-based multi-template
TE	Echo time
TLE	Temporal lobe epilepsy
TLE-HA	TLE with hippocampal atrophy
TLE-NV	TLE with normal hippocampal volume
TE	Echo time
VBM	Voxel-based morphometry
VoIMulti	Automatic segmentation using volume-based multi-template
WM	White matter

Chapter 1

Introduction

Epilepsy, a brain disorder that affects 1% of the population, is characterized by recursive seizures that are episodes of abnormal, hypersynchronous neuronal activity in the brain, ultimately impairing a patient's social skills (Fisher et al., 2005). In pharmacologically intractable focal epilepsies, the epileptogenic zone generating seizures is associated with a structural brain lesion. The most common form of intractable focal epilepsy is temporal lobe epilepsy (TLE) related to mesiotemporal sclerosis (MTS), which appears as atrophy and signal changes on MRI (Berkovic et al., 1991; Jackson et al., 1990). Surgical removal of the MTS detected on MRI is the only effective treatment, offering seizure freedom in more than 70% of cases (Schramm and Clusmann, 2008).

In TLE, the majority of MRI studies have focused on volumetry of the mesiotemporal lobe (Bernasconi et al., 2003b; Jackson et al., 1993a; Kuzniecky et al., 1999). Although this technique allows for a correct lateralization of the seizure focus, hippocampal volumes are normal in 30% of TLE patients. In these patients, however, histopathology of surgical specimens reveals subtle sclerosis.

Moreover, it remains unclear whether mesiotemporal lobe structural atrophy is driven by widespread or focal morphological changes. Indeed, volumetry alone does not allow for the detection of focal abnormalities, which might be an important prognostic factor when determining the area of mesiotemporal lobe to be resected at surgery.

Advanced surface-based shape models, including deformation-based mapping (Csernansky et al., 2000; Hogan et al., 2006; Posener et al., 2003; Wang et al., 2001) and spherical harmonics description combined with point distribution models (SPHARM-PDM), have allowed for the localization of morphological changes that may not be readily visible on MRI (Styner et al., 2006), and have successfully identified hippocampal pathology in various brain disorders (Hogan et al., 2004; Styner et al., 2004). However, the displacement metric provided by these approaches is unable to differentiate volume changes from positional differences, making biological interpretations of findings difficult to ascertain.

Manual labeling is considered the gold standard to measure hippocampal volume, as it is accurate, reproducible, and sensitive (Bernasconi et al., 2003b; Jackson et al., 1993a; Kuzniecky et al., 1999). On the other hand, its time-consuming nature, rater-bias and the increased demand to study large cohorts of healthy and diseased populations have motivated the development of automated segmentation procedures. In TLE, automatic segmentation algorithms have generally shown worse agreement to manual labels than in controls (Akhondi-Asl et al., 2011; Avants et al., 2010; Chupin et al., 2009b; Hammers et al., 2007; Heckemann et al., 2010; Pardoe et al., 2009). The reduced performance may stem from factors other than atrophy, as previous approaches achieved similar accuracy in patients with Alzheimer's disease as in healthy subjects, a degenerative disorder associated with marked hippocampal atrophy (Barnes et al., 2008; Chupin et al., 2009b; Leung et al., 2010). In addition to atrophy, a significant proportion of TLE patients show hippocampal malrotation, the atypical morphology of the hippocampus and its surrounding structures (Bernasconi et al., 2005a; Voets et al., 2011), which is considered a marker of neurodevelopmental

anomalies (Baulac et al., 1998) and etiological factors contributing to the pathogenesis of this condition (Blumcke et al., 2002; Sloviter et al., 2004).

Furthermore, hippocampal malrotation may co-occur with unusual morphology of the collateral sulcus as early fetal pathologic mechanisms affecting hippocampal development may also trigger anomalies in the neighboring areas through cortico-cortical projection fibers. This hypothesis is supported by studies of various brain disorders including schizophrenia (Connor et al., 2004; Jou et al., 2005; Kikinis et al., 1994; Kulynych et al., 1997; Sallet et al., 2003) and autism (Levitt et al., 2003; Salmond et al., 2005) showing hippocampal malrotation coincident with abnormal cortical folding in the temporal lobe.

In the presence of such anatomical anomalies, automatic segmentation algorithms may fall into abnormal local minima when using a template based on healthy subjects or prior-knowledge of normal anatomy. Multi-template approaches offer an appropriate framework to account for structural variability by selecting a subset of atlases from a database, which best describe the anatomical characteristics of the target structure. To date, these techniques have been volume-based and applied to the segmentation of healthy hippocampi (Aljabar et al., 2009; Collins and Pruessner, 2010).

The three overall purposes of this Thesis are to: i) develop surface-based techniques that can independently quantify focal atrophy, positional variations and sulcations; ii) evaluate the impact of these morphometric anomalies on automatic segmentations; iii) propose a robust automated segmentation of mesiotemporal structures by taking into account temporal lobe morphological variants.

We addressed the following five specific objectives:

1. Developing surface-based analysis of the Jacobian determinant to allow for the quantification of focal volume changes and constructing a medial axis model to quantify fine-scale local position and curvature.

2. Investigating *in vivo* static and dynamic patterns of mesiotemporal subfield pathology in TLE using 3D surface-based shape modeling.
3. Categorizing the sulcal morphological patterns of the mesiotemporal region in patients and healthy controls.
4. Evaluating the impact of hippocampal malrotation on the performance of automated hippocampal segmentation algorithms.
5. Developing an automatic segmentation method based on a multi-template approach that statistically models parametric surfaces and locoregional texture features.

The Thesis is organized as follows: Chapter 2 reviews the relevant literature. Chapters 3 to 5 are a series of manuscripts that describe the proposed methods and the performed experiments. The final Chapter summarizes the key findings and highlights the significance of this work.

Chapter 2

Background

2.1 Epidemiology of temporal lobe epilepsy

Epilepsy is a serious health problem that affects people of all ages, races and socioeconomic backgrounds. It is the most prevalent chronic neurologic disorder in Canada and affects about 1% of the population (Hauser and Hesendorffer, 1990; Wiebe *et al.*, 1999). Epilepsy is the second most common cause of mental health disability, particularly among young adults (Murray *et al.*, 1994) and accounts for a worldwide burden of illness similar to that of breast cancer in women and lung cancer in men (Kale, 1997). Complex partial epilepsy of temporal lobe origin accounts for 40% of all epilepsies in adults (Engel, Jr., 1996). In the majority of patients with temporal lobe epilepsy (TLE), seizures occur with a sufficient frequency to impair the patient's quality of life despite optimal drug therapy. There are more than 20,000 candidates for assessment of possible surgical management across Canada (McLachlan, 2001). A recent randomized trial of surgery for TLE performed in Canada confirmed the superiority of surgery over medical therapy in terms of control of seizures, quality of life, rates of

employment and school attendance among patients with poorly controlled seizures (Wiebe *et al.*, 2001). Fortunately, the majority of these patients can be helped by surgery, providing the seizure generator can be identified.

2.2 Pathology and electrophysiology in temporal lobe epilepsy

Histopathological descriptions of hippocampal sclerosis are based on macroscopic examination of autopsy brain specimens (Margerison and Corsellis, 1966; Meencke and Veith, 1991), and have been refined through microscopic analysis (Bruton, 1988) and neuronal counts (Babb *et al.*, 1984; Blümcke *et al.*, 2007; de Lanerolle *et al.*, 2003; Thom *et al.*). In a semi-quantitative study of a large number of hippocampal specimens obtained at surgery, an unbiased clustering technique identified severe CA1 neuronal loss in the vast majority of cases, whereas the other subfields were only moderately affected (Blümcke *et al.*, 2007). The pathogenesis and functional significance of hippocampal sclerosis are still poorly understood.

Early studies of surgically resected specimens demonstrated that neuronal damage is not limited to the hippocampus, but extends to other mesiotemporal structures including the amygdala as well as the surrounding cortical areas, particularly the entorhinal cortex (Cavanagh and Meyer, 1956; Falconer *et al.*, 1964; Margerison and Corsellis, 1966; Bruton, 1988; Meencke and Veith, 1991). However, a comprehensive evaluation of the mesiotemporal structures is limited as tissue obtained from surgical resections may be incomplete due to partial resections or fragmented as a result of sub-pial aspiration (Braak and Braak, 1992; Schramm and Clusmann, 2008). Nevertheless, histological changes in the amygdala have been shown, either in the presence (Bruton, 1988; Falconer *et al.*, 1964) or absence (Hudson *et al.*, 1993) of hippocampal sclerosis. In a study based on the examination of surgical specimens, astrogliosis and neuronal loss was seen predominantly in layer III of the entorhinal cortex (Du *et al.*, 1993). More recently, histopathological examination of surgical specimen showed

variable degrees of pathological changes in all layers of the entorhinal cortex (Yilmazer-Hanke *et al.*, 2000) and significant inter-individual variation in the lesion distribution within layers.

Although electrophysiological studies have demonstrated that mesiotemporal seizures originate in the hippocampus, there has been abundant evidence that mesiotemporal structures other than hippocampus participate in seizure generation and propagation (Feindel and Penfield, 1954; Piredda and Gale, 1985; Hudson *et al.*, 1993). Mesial temporal lobe seizures may in fact involve multiple limbic generators (Wilson *et al.*, 1988; Spencer *et al.*, 1992).

In animal models of TLE, the entorhinal cortex has been shown to contribute to the development and maintenance of epileptiform activity in the temporal lobe (Du *et al.*, 1995b; Bragin *et al.*, 1997). In acute animal experiments, electrolytic lesions or electric stimulation and administration of chemoconvulsants to this region can effectively induce seizures in the hippocampus (Collins *et al.*, 1983). Furthermore, *in vitro* studies of focal epileptogenesis in combined hippocampal-entorhinal slices have demonstrated that the entorhinal cortex possesses an intrinsic capacity to generate epileptiform discharges (Bear and Lothman, 1993). On the other hand, damage to the entorhinal cortex may contribute to long-lasting changes in its excitability and may therefore play a primary role in the genesis of temporal lobe seizures (Scharfman *et al.*, 1998). After an extended seizure period, irreversible neuronal damage appears in the entorhinal cortex within 48 hours, and is followed by neuronal loss and gliosis in other areas such as the subiculum, CA1 subfield of the hippocampus and amygdala. Since entorhinal cortical neurons are heavily interconnected to the subiculum and CA1 subfield of the hippocampus (Witter *et al.*, 1988), it has been postulated that entorhinal neurodegeneration may secondarily result in hippocampal hyperexcitability and thus contribute to limbic seizures (Du *et al.*, 1995a). There is also evidence that by reducing hippocampal output activity and abolishing the inhibitory control over the entorhinal cortex, cell damage in the CA3-CA1 areas of the hippocampus releases entorhinal cortical network hyperexcitability (D'Antuono *et al.*, 2002). Therefore, a change in the network interaction between

the hippocampus and the entorhinal cortex is believed to confer properties to the damaged limbic system that allow for the production of recurrent limbic seizures.

Human electrophysiological data also indicate that the entorhinal cortex is part of the epileptogenic network in TLE (Rutecki *et al.*, 1989; Spencer and Spencer, 1994). Investigations with stereotaxically implanted electrodes have shown that seizures may originate not only in the amygdala and the hippocampus but also in the entorhinal cortex (Spencer and Spencer, 1994). Some studies have suggested that potentials recorded with scalp or depth electrodes may reflect seizure activity that begin in the hippocampus or be the result of hippocampal amplification of a signal from the entorhinal cortex (Spencer and Spencer, 1994; Swanson, 1995). It has also been shown that intraoperative stimulation of the entorhinal cortex may induce a hippocampal response identical to interictal spikes (Rutecki *et al.*, 1989; Wilson *et al.*, 1990). Moreover, analyzing limbic system pathways using neuronal responses evoked by electrical stimulation (Wilson *et al.*, 1990) found that the strongest functional connections were between hippocampus, entorhinal cortex and presubiculum, the latter two being in a critical position to modulate and control the activity of the hippocampus itself.

2.3 Mesiotemporal lobe structures on MRI: morphological changes in TLE

The increasing sophistication of MR image acquisition methods allows for *in vivo* visualization of brain structures in detail. This imaging technique has been demonstrated to provide a reliable morphological indicator of pathologic findings underlying TLE, including neurological damages in mesiotemporal structures (**Figure 2.1**). In this section, such morphological changes in TLE, which has been observed in previous studies, and their clinical implication are reviewed.

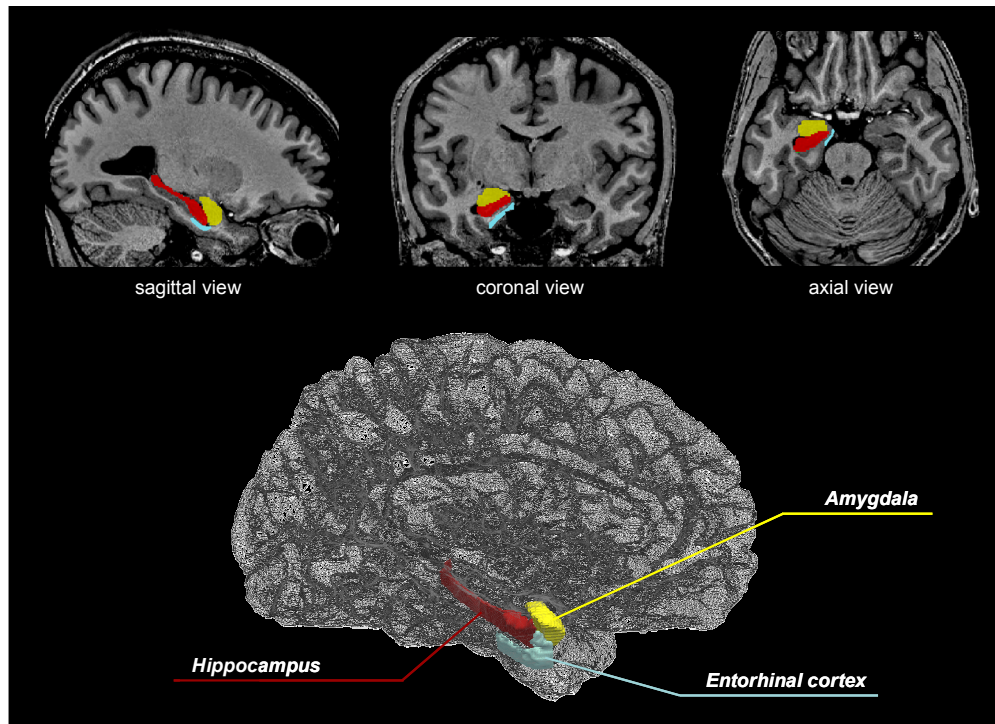


Figure 2.1. Anatomy of the mesiotemporal structures.

Manual segmentations of the hippocampus, amygdala and entorhinal cortex on 3T high resolution isotropic T1-weighted MRI (*top*), as well as their 3D surface rendering of a healthy subject (*bottom*).

2.3.1 Quantitative MRI of mesiotemporal sclerosis

The most common MRI-markers of hippocampal sclerosis include hippocampal atrophy (**Figure 2.2**), measured as a reduction in hippocampal volume on T1-weighted images (Cascino et al., 1991; Cendes et al., 1993a) and hippocampal hyperintensity on T2-weighted images (Berkovic et al., 1991; Jackson et al., 1990).

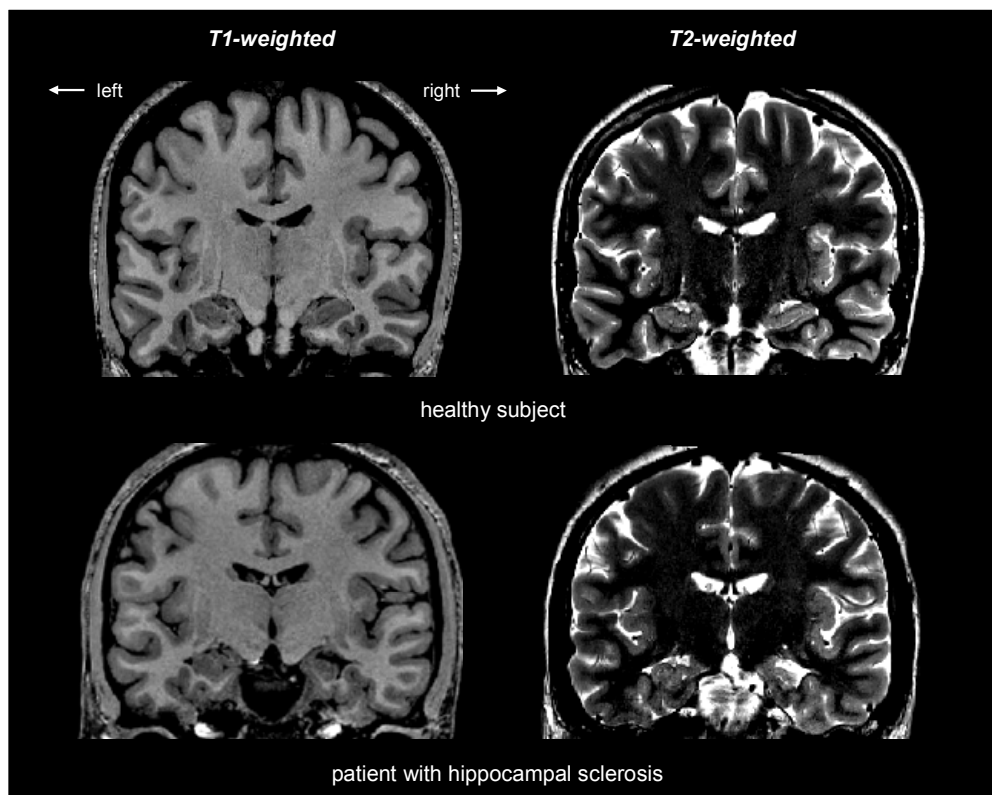


Figure 2.2. MRI of a healthy subject (*top*) and a patient with right sided hippocampal sclerosis (*bottom*). The most common MRI markers of hippocampal sclerosis are hippocampal atrophy or shrinkage on T1-weighted images (*left*) and hyperintensity of T2-weighted images (*right*).

Indeed, for the last two decades, MRI volumetry has been the most commonly employed quantitative technique to assess mesiotemporal lobe pathology. In TLE, hippocampal atrophy is considered a surrogate marker of hippocampal sclerosis, as the degree of atrophy correlates with the severity of neuronal loss in the *cornu Ammonis* (CA), particularly CA1 (Cascino et al., 1991).

The clinical utility of hippocampal volumetry stems from its ability to correctly lateralize the seizure focus in 70-80% of patients (Cascino et al., 1992b; Cendes et al., 1997; Jack et al., 1992), and its value in predicting post-surgical seizure outcome (Arruda et al., 1996; Berkovic et al., 1995; Cohen-Gadol et al., 2006; Jack et al., 1992; McIntosh et al., 2001; Schramm and Clusmann, 2008).

However, since this method provides a global estimate of atrophy, its sensitivity to detect subtle diffuse or focal anomalies is limited. Indeed, in up to 30% of patients with unambiguous electroclinical features of drug-resistant TLE, hippocampal volumetry is unremarkable, despite the presence of mild degrees of sclerosis on histology (Bernasconi et al., 2001; Jackson et al., 1994). Moreover, volumetry fails to predict a favorable outcome in about 30% of patients, even in the presence of hippocampal atrophy ipsilateral to the seizure focus (Antel et al., 2002b).

Atrophy in the entorhinal cortex is found in a large spectrum of TLE patients, including those with hippocampal atrophy (Bernasconi et al., 1999; Jutila et al., 2001) and normal hippocampal volumes (Bernasconi et al., 1999; Bernasconi et al., 2001), supporting the hypothesis that this structure plays a pivotal role in the epileptogenic network of this condition (Bartolomei et al., 2005; Roch et al., 2002).

Volumetric studies concur that damage to the mesiotemporal lobe involves not only the hippocampus, but also the amygdala, although the sensitivity of detecting atrophy in the latter is low (Bernasconi et al., 2003b; Bonilha et al., 2003; Silva et al., 2010).

In drug-resistant TLE, longer disease duration has been consistently associated with progressive atrophy of mesiotemporal lobe structures (Bernasconi et al., 2005b; Fuerst et al., 2003; O'Brien et al., 1999; Seidenberg et al., 2005; Theodore et al., 1999; Van Paesschen et al., 1998). Most studies have been based on cross-sectional analyses that generally offer the advantage of large sample sizes. The drawback of this approach is the confounding effect of age, because it is highly correlated to disease duration (Bernhardt et al., 2009). Alternatively, longitudinal designs based on relatively short interscan intervals remove potential aging confounds. Moreover, as they control for intersubject variability, statistical sensitivity to detect subtle changes increases (Bernhardt et al., 2009).

2.3.2 Hippocampal malrotation: a biological marker of developmental abnormalities

There is growing evidence that hippocampal developmental abnormalities participate in the pathogenesis of a number of disorders, including epilepsy (Baulac et al., 1998; Fernandez et al., 1998; Thom et al., 2002a), schizophrenia (Connor et al., 2004) and autism (Lord et al., 2000; Salmond et al., 2005). These abnormalities are thought to be secondary to the incomplete inversion of the fetal hippocampus and atypical folding process of adjacent cortices. To date, the *in vivo* identification of such changes, generally referred to as malrotation, have been based on the visual description on MRI.

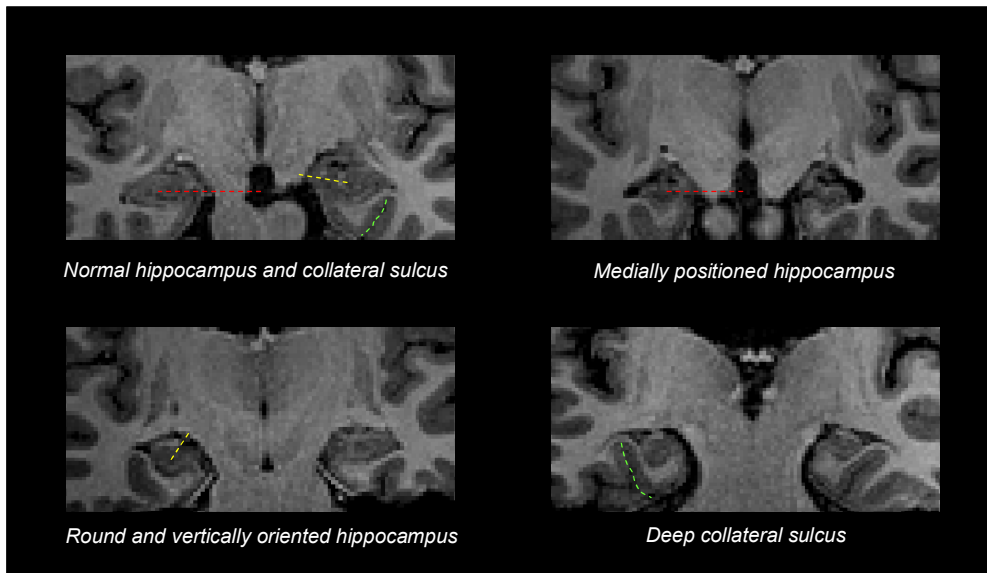


Figure 2.3. Morphological characteristics of malrotation on MRI: hippocampal medial positioning, roundness and vertical orientation, increased collateral sulcus depth. Dotted lines: distance between the midsagittal line and the centroid of the hippocampus in red; hippocampal sulcus in yellow; collateral sulcus in green

Malrotation is mainly characterized by a globular, and atypically orientated hippocampus, as well as an unusually deep and verticalized collateral sulcus (**Figure 2.3**) (Bajic et al., 2008; Barsi et al., 2000b; Baulac et al., 1998). Using

these criteria, we previously showed that hippocampal malrotation is more prevalent in patients with epilepsy than healthy controls (Bernasconi et al., 2005a). Indeed, it is present in 43% of patients with pharmaco-resistant TLE.

The visual analysis of malrotation, however, becomes challenging mainly due to the complex and convoluted anatomy of the hippocampal formation as well as its surrounding structures. Indeed, coincident anomalies in neighboring structures may influence the rater's judgment. For instance, an observer may perceive a collateral sulcus abnormally deep simply because it protrudes into an empty choroid fissure, and not because it is effectively deep. Previous visual evaluations have been performed in native MRI space, thus hindering an objective identification of morphological changes independent of head positioning and slice orientation. Furthermore, the terminology and selection of the evaluation criteria vary considerably, making an unbiased comparison across studies unlikely.

2.4 Computational models of abnormal morphology

A central factor in the increasingly widespread application of computational neuroanatomy approaches in medicine has been the development of sophisticated mathematical and algorithmic methods for extracting and modeling clinically significant and scientifically important information from image data.

Computational model-based techniques aim at quantifying morphological characteristics of brain structures and allow for the comparison of these features between controls and patients. These methods allow for the generation of 3D parametric maps that should be ultimately reproducible and rater-independent. Image processing methods are becoming increasingly sophisticated and the tendency is to develop as much automation as possible.

2.4.1 *Voxel-based morphometry*

Even though the most accurate volume measurement is achieved by manual delineation of a given brain structure, this process is time-consuming (*i.e.*, about 3 hours for both hippocampi and amygdalae), thus making it difficult to study large cohorts of healthy and diseased populations. Moreover, different criteria in defining anatomical boundaries between centres prevent the direct comparison across studies.

Voxel-based morphometry (VBM) (Ashburner and Friston, 2000, 2001; Good et al., 2001) has been extensively used to assess structural abnormalities in various types of brain disorders as it permits the automatic identification of regional differences in the amount of gray matter (GM) and white matter (WM) without a *priori* region of interest (Bernasconi et al., 2004; Chetelat et al., 2002; Keller et al., 2004; Wilke et al., 2004). After image preprocessing including intensity non-uniformity correction and linear spatial normalization, MR images are fed into an automated classifier that categorizes voxel intensities into GM, WM or cerebrospinal fluid (CSF). Binarized tissue-specific maps are blurred using an isotropic Gaussian kernel to generate tissue density estimates at each voxel, with which statistical inference is performed to assess differences of GM or WM tissue concentration between groups. To improve the sensitivity to detect changes in small regions, this standard VBM procedure underwent a set of major modifications, including an optimization based on the integration of tissue specific templates as well as a modulation step that adjusts tissue density estimates with Jacobian determinants computed in the nonlinear registration step (Good et al., 2001).

Both the traditional and optimized VBM techniques have been widely applied to TLE. In general, using VBM, findings in mesiotemporal lobe structures are not as marked as those detected by manual volumetry and are inconsistent between studies. Hippocampal atrophy has been reported in one initial study (Duncan, 1997). Yet, about 30% of subsequent VBM studies have not identified the epileptic focus in patients with unilateral hippocampal atrophy (Keller and

Roberts, 2008). Furthermore, a few TLE studies reported entorhinal volume reduction, even though this structure is often implicated in seizure generation and propagation (Gloveli et al., 1998; Miettinen et al., 1998; Schwarcz and Witter, 2002; Wozny et al., 2005) and has been consistently shown to be atrophic in studies based on manual volumetry (Bernasconi et al., 1999; Bernasconi et al., 2000; Bernasconi et al., 2003b; Bernasconi et al., 2001; Jutila et al., 2001).

The inconsistent results and lower sensitivity of VBM relative to volumetry may be explained by several factors. First, in most studies, the quantification of volume changes in small mesiotemporal lobe structures was done using with a smoothing kernel larger than 10mm, making the detection of volume variations in a region smaller than this kernel size unlikely. Second, it is possible that inaccurate spatial normalization, due to the fact that VBM relies on intensity-based correspondences, may increase inter-subject variability or misplace the loci of volume changes. Third, computation of tissue density in VBM is heavily dependent on accurate tissue segmentation. In particular, the optimized VBM approach uses tissue-specific templates in the nonlinear registration step (Good et al., 2001). However, due to noise and local intensity non-homogeneities that may persist even after corrections, automated procedures may still yield inaccurate tissue segmentation (Cardoso et al., 2011).

2.4.2 *Deformation-based morphometry*

To overcome the above-mentioned limitations of VBM, deformation-based morphometry (DBM) has been developed. DBM is a quantitative image analysis technique that evaluates information contained within the vector field generated by the nonlinear warping of an individual MRI scan to a reference template (Ashburner et al., 1998b; Bookstein, 1997; Chung et al., 2001a; Thompson et al., 2000). This technique has been employed broadly to assess morphological changes occurring in brain development or related to brain disorders (Ashburner et al., 1998a; Brambati et al., 2009; Cardenas et al., 2007; Chung et al., 2001a;

Gogtay et al., 2008; Whitford et al., 2007). In contrast to VBM, DBM does not require tissue segmentation, and mis-registration is minimized (Brambati et al., 2007; Lau et al., 2008; Pieperhoff et al., 2008; Tosun et al., 2011; Whitford et al., 2007), prompting its use for the analysis of longitudinal data (see **Figure 2.4**).

Longitudinal DBM studies in TLE have been limited, since only a fraction of patients with intractable seizures refuse surgical treatment. A recent DBM study analyzing children with newly diagnosed, mostly medically-tractable focal epilepsy found bilateral progressive hippocampal atrophy (Tosun et al., 2011), with no other structural changes in the mesiotemporal lobe.

Nevertheless, due to the isotropic Gaussian kernel-based smoothing, DBM suffers from limitations similar to those of general voxel-based analyses and has low sensitivity in detecting anomalies in small brain structures.

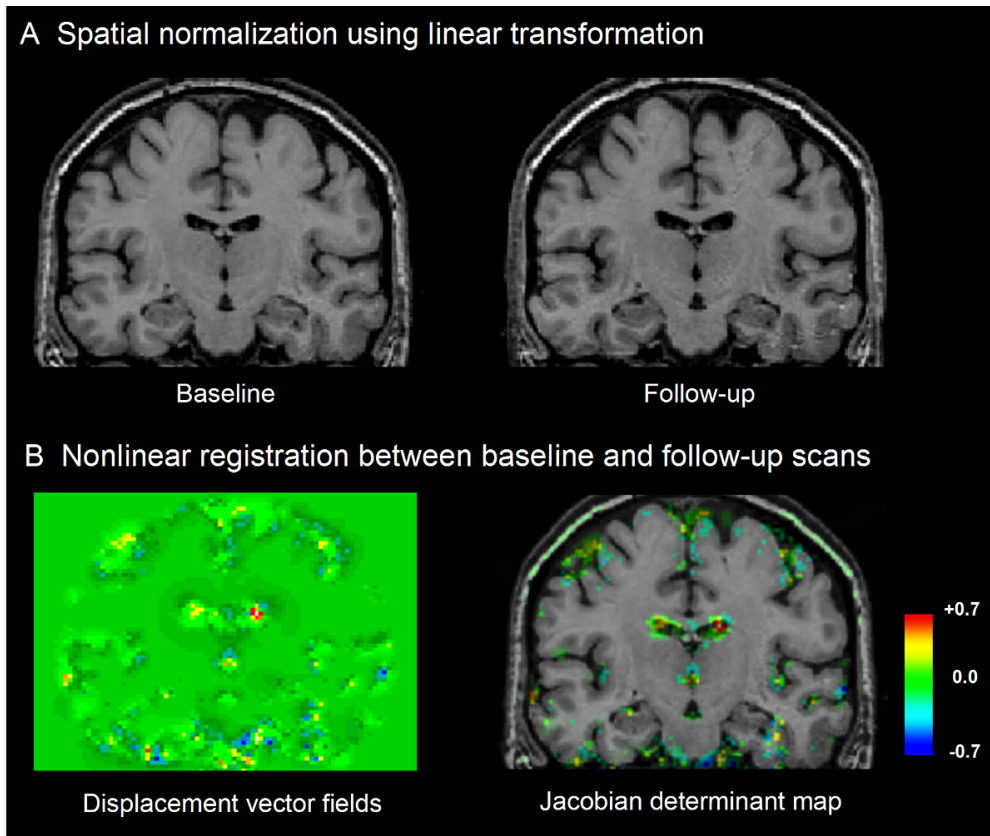


Figure 2.4. Longitudinal DBM. **A)** For each subject, the baseline MRI scan (*i.e.*, the 1st scan) is registered into Talairach space and the follow-up scan is linearly transformed to the same space using the affine matrix computed from the baseline scan. **B)** A nonlinear registration of follow-up MRI to the baseline-scan and subsequent inverse transformation computes displacement vector fields. Finally, on this vector fields, vertex-wise Jacobian determinants are calculated to assess morphological changes over time.

2.4.3 Surface-based approaches

Unlike traditional volumetric or voxel-based approaches, surface shape models and statistical maps permit the examination of highly localized morphological differences between groups while providing shape-constrained point-wise correspondences across subjects (Csernansky et al., 2002; Gerig et al., 2001; Hogan et al., 2004; Morra et al., 2009; Nicolson et al., 2006; Styner et al., 2004; Styner et al., 2006; Wang et al., 2001). Moreover, surface-based anisotropic

smoothing using heat diffusion reduces noise and normalizes data distribution along a manifold, thus increasing statistical power without loss in sensitivity (Chung et al., 2001b).

Surface-based techniques mainly include deformation-based mapping (Csernansky et al., 2000; Hogan et al., 2006; Posener et al., 2003; Wang et al., 2001), spherical harmonics description combined with point-distribution models (SPHARM-PDM) (Gerig et al., 2001; Styner et al., 2006) and central path-based thickness mapping (Narr et al., 2004; Nicolson et al., 2006). These vertex-wise computational methods have enabled the detection of regional alterations of hippocampal morphology in neurological conditions such as Alzheimer's disease (Csernansky et al., 2000; Wang et al., 2001), schizophrenia (Narr et al., 2004), depression (Posener et al., 2003), autism (Nicolson et al., 2006) and epilepsy (Hogan et al., 2004), even in the absence of significant volume reductions (Csernansky et al., 2002; Hogan et al., 2008; Styner et al., 2004).

The central path-based thickness mapping measures a radial distance between a vertex point and its corresponding point on the medial axis or surface (*i.e.*, the central path of a 3D object). In this method, the measurement is not biased towards a template built from a sample group. However, due to the metric's *symmetrical* nature, local atrophy in a given structure may be mirrored to the counterpart surface, thus obscuring the biological interpretation. Deformation-based mapping and SPHARM-PDM, on the other hand, allows localizing *asymmetrically* shape changes. In this approach, the signed surface normal components of the displacement vectors between a given surface and the template are generally used to describe inward/outward deformations, which have been interpreted as the result of local volume changes (**Figure 2.5**). Yet, this displacement metric is unable to differentiate volume changes from positional differences.

Another type of surface-based technique is shape mapping based on the medial surface. This method allows for the quantification of local positional changes by assessing morphological variations of the skeleton extracted from a given 3D object (Joshi et al., 2002; Styner et al., 2004). Since this approach generally

relies on coarse-scale sampling, it may lack sensitivity to assess high-dimensional features, making a plausible biological interpretation difficult.

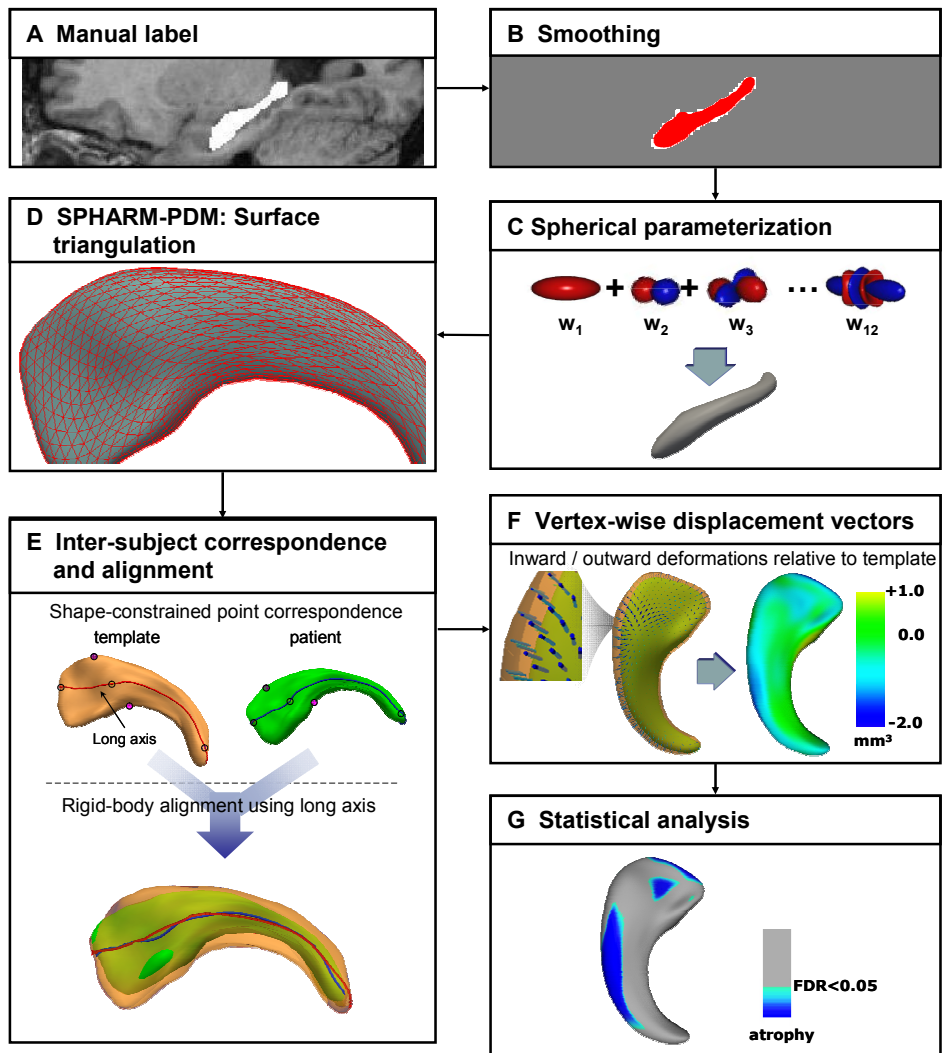


Figure 2.5. Displacement vector analysis. Manual labels are converted to surface meshes (A). After minimal smoothing (B), labels are parameterized using spherical harmonic description (C) and point-distribution models (D) (SPHARM-PDM) ensuring point-wise correspondence through an icosahedron subdivision (E top). Each individual surface is rigidly aligned to a template constructed from the mean surface of controls (E bottom). Vertex-wise displacement vectors are then calculated between each individual and the template. The surface normal components of these vectors are used to quantify inward and outward deformations (F). Vertex-wise t-tests statistically infer differences between patients and healthy controls (G).

2.4.4 Descriptive models

Although surface-based mathematical shape models (Bouix et al., 2005; Csernansky et al., 2002; Nicolson et al., 2006; Shenton et al., 2002; Styner et al., 2004) allow for the reliable assessment of local shape variations, correcting rotation and positioning through rigorous inter-subject registration steps may remove the inherent features of hippocampal malrotation.

On the other hand, descriptive models allow for the quantification of fundamental morphological characteristics, such as orientation (Dunteman, 1989), length (Ochiai et al., 2004), depth (Kochunov et al., 2005) and roundness (Rosin, 2003; Voss and Suesse, 1997). These models are easy to interpret, insensitive to noise and scaling (Rosin, 2003), and thus have the potential to detect subtle shape and positional changes that characterize hippocampal malrotation.

Descriptive models may be also useful to improve segmentation results. For example, use of kernel-based descriptive models identifying edges oriented at a predefined angle successfully identifies voxels surrounding the hippocampus. A region-growing based segmentation technique using these voxels to constrain segmentation deformation has accurately segmented the hippocampus in controls and patients with Alzheimer's disease (Chupin et al., 2007).

2.5 Performance of automated segmentation in healthy and pathological hippocampi

As discussed in section 2.3.1, temporal lobe epilepsy (TLE) is related to hippocampal sclerosis, which appears as atrophy on MRI (Cascino, 2008; Cendes et al., 1993b; Jackson et al., 1990). Detecting hippocampal atrophy is clinically relevant as it allows for the lateralization of the seizure focus and thus, the identification of the surgical target. Manual delineation of the hippocampus is considered to be the gold standard, as it is accurate, reproducible, and sensitive (Bernasconi et al., 2003b; Jackson et al., 1993b; Kuzniecky et al., 1999). On the

other hand, high time requirement, rater-bias, and the increased demand to study large cohorts of healthy and diseased populations have motivated the development of automated segmentation procedures. Although there have been numerous attempts to automate hippocampal segmentation, such procedures to delineate structures with boundaries of unclear intensity contrast, such as those of the hippocampus, have been considered a very challenging task.

2.5.1 Categorization of automatic segmentations

Most segmentation methods employ deformable surfaces, appearance-based or atlas-based approaches.

Deformable surfaces iteratively deform the boundaries of an initial shape to find the true border of the target structure while minimizing energy function. They take advantage of boundary forces that can model *locoregional* (on/inside/outside boundaries) intensity and texture features (Paragios, 2002; Pitiot et al., 2004). Moreover, they allow the integration of prior anatomical knowledge (e.g., shape, orientation, landmarks) (Kelemen et al., 1999; Leventon et al., 2000).

Ghanei and colleagues (Ghanei et al., 1998) attempted to incorporate statistical shape information using a deformable balloon model to segment *healthy* hippocampi. Two subsequent studies used the mean shape of *healthy* subjects in the initialization step and guided the deformation direction using principal component analysis (PCA) (Kelemen et al., 1999; Leventon et al., 2000). These methods constrained deformable surfaces to evolve within the range of normal shape variation, thus preventing from biologically unreasonable deformations as well as allowing the objective function to converge faster. However, in the presence of anatomical variants, automatic approaches may fall into *local minima* when using prior-information based on *healthy subjects*.

In the last decade, non-parametric deformable models using level-set formulations were broadly used as they allow for more flexible deformations against morphological and topological variations, thus enabling the simultaneous

segmentation of multiple structures (Tsai et al., 2003; Yang and Duncan, 2004). Earlier non-parametric deformable models were based on curve evolution and geometric vector flow (Caselles et al., 1997; Malladi et al., 1995). Later, Chan and Vese (Chan and Vese, 2001) proposed the use of a Mumford-Shah functional that enables the deformable model to detect objects with boundaries that are not necessarily fully defined by gradient data (i.e., with very smooth or even with discontinuous boundaries). To statistically model anatomical variability through these approaches, more recent studies combined geodesic active contouring with shape and intensity distribution information using principal component analysis (PCA) (Leventon et al., 2000; Yang and Duncan, 2004). Non-parametric deformable models, however, do not allow for point-wise inter-subject correspondences. This drawback complicates local sampling to capture texture and shape characteristics within separate regional compartments. Alternatively, the use of *deformable parametric surfaces* permits a vertex-wise sampling scheme (Kelemen et al., 1999; Pitiot et al., 2004).

Appearance-based (or deformable template-based) approaches have been developed to *statistically capture surrounding information* of a target structure (Cootes et al., 2001; Yang and Duncan, 2004). Texture and shape of the target structure and its surroundings are modeled by PCA (represented as a synthetic mean *volume* image) with incremental deformation of the initial segmentation along the principal axes representing anatomical variations of the training data. The segmentation strives to minimize differences between target and synthetic images. A previous study showed that these approaches decrease the computational time considerably, but do not enhance performances compared to atlas-based techniques (Duchesne et al., 2002).

Atlas-based techniques nonlinearly register an atlas, *i.e.*, a brain MR image on which target structures are manually labeled, to a query MRI. Warped atlas labels result in the final segmentation. This approach was pioneered by Bajcsy

et al. (Bajcsy et al., 1983). To avoid anatomical biases when using a single-subject template, the intensity average of a large cohort of healthy brains is used. Until the early 2000's, these techniques were developed mainly based on linear elastic models including AIR (Woods et al., 1998), SPM (Friston et al., 1995) and FLIRT (Jenkinson and Smith, 2001). Fischl and colleagues used probabilistic spatial mapping (SPAM) derived from a manually labeled training set combined with the Bayesian formula where probabilistic labels and their predicted image intensities serve as the prior probability term, while the intensity similarity between the target image and the template serves as the likelihood term (Fischl et al., 2002). However, these techniques have generally demonstrated poor segmentation accuracy for the hippocampus (Dice index<0.70) (Carmichael et al., 2005; Duchesne et al., 2002). A recent study has reported that the addition of an intensity normalization procedure improves segmentation accuracy (Han et al., 2006). More recently, viscous fluid model-based diffeomorphic registrations, allowing large deformations without losing topological information, have improved the segmentations in controls (Dice=0.75) (Khan et al., 2008).

Classification-based approaches have recently been increasingly used for the hippocampal segmentation in combination with multi-feature models that may enhance segmentation performance (Morra et al., 2008). Indeed, the use of voxel-wise shape and intensity features in Adaboost classifier that weights features depending on their inter-subject reliabilities has improved segmentation results in controls and patients with Alzheimer's disease compared to atlas-based methods (Morra et al., 2010). More recently, hybrid frameworks merging the three main segmentation approaches have been proposed (Avants et al., 2010; Wang et al., 2011).

2.5.2 Multi-template based segmentation to statistically model shape variants

In the presence of pathological anatomical variants, segmentation processes may fall into local minima when using a template that represents either a single healthy individual or the mean shape of healthy population. Such concern is valid for all the above-described automated methods since they use such a template. Moreover, deformations in appearance-based and deformable model-based approaches are generally constrained by shape priors obtained from healthy individuals.

Template library approaches represent an appealing alternative since they *automatically* select a *single atlas* that best describes anatomical characteristics of the target structure from a database (Barnes et al., 2008). In the study conducted by Barnes and colleagues, the most similar hippocampus from a group of 55 pre-labeled subjects was selected as an initial template (Barnes et al., 2008). Then, affine registration of this template mapped hippocampal labels to the test image. Finally eroding CSF voxels from these labels created the final segmentation. These approaches, however, may produce inconsistent segmentations due to lack of feature information obtained from a single source.

More recently developed multi-template (or template library and label fusion) techniques (Aljabar et al., 2009; Avants et al., 2010; Collins and Pruessner, 2009; Lotjonen et al., 2010) offer a more suitable framework that accounts for structural variability by selecting *a subset of atlases* that best describe anatomical characteristics of the target structure.

Rohlfing and colleagues explored the ability to select a *subset* among segmented bee brains on confocal microscopy images (Rohlfing et al., 2004). After they successfully achieved their goals, numerous studies applied this fascinating framework to the segmentation of human brain structures (Aljabar et al., 2009; Hammers et al., 2007; Heckemann et al., 2006). Heckmann and colleagues were the first group to evaluate hippocampal segmentation using this technique

(Heckemann et al., 2006). After nonlinearly registering all images in the library to the query image, templates were selected to construct an optimal subset. However, this approach is computationally time-consuming because of the recursive nonlinear registration procedure and is based on indirect selection criteria as it does not measure the similarity between the template and the test image to segment. To address this, Aljabar and colleagues omitted the nonlinear registration, measured mutual information between each individual template and the test image as a similarity value and used this value to rank the templates (Aljabar et al., 2009). Collins combined the multi-template approach with ANIMAL, a piece-wise linear coarse-to-fine deformation, and large database of healthy hippocampi (Collins and Pruessner, 2010) and provided the best results in segmenting healthy hippocampi as of yet.

The existing *volume-based* multi-template techniques generally rely on nonlinear registration procedures based on intensity-based point wise correspondences, which are prone to image noise and sensitive to the initial size and orientation. Thus, they may fail to accurately segment cases exhibiting atypical morphology.

2.5.3 Performance in healthy hippocampi

The performances of automatic segmentations in healthy subjects are summarized in **Table 2.1**. Early techniques showed poor agreement with manual labeling with Dice indices ranging from 72% to 80%. On the other hand, more recent techniques have produced excellent agreement with manual delineations, with Dice indices of 81-88% (Aljabar et al., 2009; Chupin et al., 2009b; Collins and Pruessner, 2010; Khan et al., 2008), reaching a degree of agreement with manual labelling comparable to inter-rater reliability (85-93%) (Chupin et al., 2007; Leung et al., 2010; Morra et al., 2008; Pohl et al., 2007; van der Lijn et al., 2008). In particular, techniques yielding Dice indices greater than 86% are mostly based on template library constructions (Barnes et al., 2008; Collins and Pruessner, 2010; Coupé et al., 2011; Gousias et al., 2008; Lötjönen et al., 2011).

Table 2.1. Automatic hippocampal segmentation in healthy subjects

Author, Journal (year)	Category	Method	Dice (%)
Fischl, Neuron (2002)	atlas	FreeSurfer:	72-82%
Morey, NI (2009)		Probabilistic atlas + Bayesian formula	
Pardoe, Epilepsia (2009)			
Kelemen, TMI (1999)	deform	Spherical harmonic description, PCA-based statistical shape model	75%
Hogan, JDI (2000)	atlas	landmark + fluid mechanics-based deformation model	75%
Firbank, HBM (2008)	atlas	SPM standard segmentation + rule-based morphological operation	75%
Khan NI, (2008)	atlas	FreeSurfer initialized, large deformation diffeomorphic mapping	75%
Klemencic, JIST (2004)	appear	Deformation variation modeled using PCA	80%
Avants, NI (2010)	atlas appear	Appearance model + diffeomorphic mapping	80%
Pohl, TMI (2009)	class	Hierarchical EM	81%
Heckemann, NI (2006)	m-atlas	Template library + label-fusion	82%
Aljabar, NI (2008)	m-atlas	Template library + label-fusion	84%
Morra, NI (2008)	class	Auto context model + adaboost	85%
Van der Lijn, NI (2008)	atlas	A priori + graph cuts	86%
Chupin, NI (2009)	deform	Detection of anatomical landmark + region growing	87%
Barnes, NI (2008)	m-atlas	Template library + morphological operation	87%
Wang, NI (2011)	atlas+ class	FreeSurfer + learning-based wrapper to correct systematic errors	87%
Gousias, NI (2008)	m-atlas	Template library + label-fusion, free-form deformation	88%, (pediatric data)
Lötjönen, NI (2010)	m-atlas	Template library + label-fusion	88%
Collins, NI (2010)	m-atlas	Template library + label-fusion, ANIMAL-based deformation	88% (median)
Coupé, NI (2011)	m-atlas	Template library + label-fusion, weighted average	88% (median)

Journal abbreviation: JDI=Journal Digital Imaging, NI=NeuroImage, HBM: Human Brain Mapping, TMI=IEEE Trans Medical Imaging, JIST=Journal of Imaging Science and Technology.

Segmentation category: atlas=atlas-based, appear=appearance-based, deform= deformation-based, class=classification-based, m-atlas=multi-template (or template library and label fusion)

2.5.4 Performance in pathological hippocampi

The performances of automatic hippocampal segmentations in disease populations are summarized in **Table 2.2**. Segmentation based on deformable surfaces, appearance-based or atlas-based approaches have so far resulted in poor performances. Alternatively, **texture modeling of the surrounding structures** improved the segmentations of *atrophic* hippocampi (Avants et al., 2010; Chupin et al., 2007). In particular, the *automated detection* of intensity- and geometry-invariant patterns of structures that *surround the hippocampus* (alveus, lateral ventricle, parahippocampal white matter) yielded promising results in Alzheimer's disease (**Dice=0.84**) (Chupin et al., 2009a).

Inadequate segmentation of pathological hippocampi, compared to healthy hippocampi, may stem from the fact that the features estimated from an initial, non-specific template may not represent adequately all shape variants. Initialization is therefore sub-optimal, which greatly increases the risk of convergence to local minima. So far, this problem has usually been addressed by *manual landmarking* (Pluta et al., 2009; Shen et al., 2002) or *manual initialization* (!!! INVALID CITATION !!!), which are both time-consuming, as they require neurological expertise (Shen et al., 2002), and are rater-sensitive (!!! INVALID CITATION !!!).

Alternatively, **multi-template approaches** that select template(s) most similar to the structure to segment provide optimal automated initialization. Indeed, excellent performances in segmenting atrophic hippocampi in Alzheimer's disease have been recently demonstrated using these techniques (Dice=81%-86%).

In TLE, automatic segmentation algorithms have shown lower agreement with manual labels than in healthy controls or in other disease populations, with kappa indices ranging from 63% to 77% (Akhondi-Asl et al., 2011; Avants et al., 2010; Chupin et al., 2009b; Hammers et al., 2007; Heckemann et al., 2010; Pardoe et

al., 2009). The reduced performance likely arises from factors other than atrophy, as previous approaches achieved accuracies comparable to healthy subjects when segmenting atrophic hippocampi (Barnes et al., 2008; Chupin et al., 2009a; Leung et al., 2010). Indeed, as discussed in section 2.3.2, in addition to atrophy, about 40% of TLE patients have atypical shape and positioning of the hippocampus referred to as malrotation (Bernasconi et al., 2005a; Voets et al., 2011). This anomaly not only alters the hippocampal morphology, but also modifies its spatial relationship with surrounding structures (Baulac et al., 1998; Bernasconi et al., 2005a).

Thus, current **texture modeling techniques** based on prior knowledge (e.g., parahippocampal WM located below the hippocampus, with a 45° interface) may be error-prone when a given structure and its surroundings are dissociated from predefined relationships, as in the presence of hippocampal malrotation (Avants et al., 2010; Chupin et al., 2007).

Alternatively, constructing a **library of texture and shape features** and **integrating this into multi-template frameworks** may overcome the hindrance of texture modeling. A precise delineation of structural boundaries and the creation of accurate point-correspondence should precede the construction of this feature library in order to accurately capture variations of locoregional characteristics.

Table 2.2. Automatic hippocampal segmentations in neurological disorders.

Author, Journal (year)	category	Method	(Dice %)
Temporal lobe epilepsy			
Pardoe, Epilepsia (2009)	atlas	First FreeSurfer	62% 66%
Avants, NI (2010)	appear	Appearance model + diffeomorphic mapping	74%
Akhondi-Asl, NI (2011)	atlas+ appear	Multi-atlas strategy, entropy-based optimization	72%
Chupin, NI (2009)	deform	Detection of anatomical landmark + region growing	79%
Alzheimer's disease			
Firbank, HBM (2008)	atlas	SPM standard segmentation + rule-based morphological operation	67%
Khan, NI (2008)	atlas	FreeSurfer initialized, large deformation diffeomorphic mapping	72%
Lötjönen, NI (2010)	m-atlas	Template library + label-fusion	81%
Wolz, NI (2010)	m-atlas	Template library + label-fusion, graph theory	85%, mixed with controls
Morra, NI (2008)	class	Auto context model + adaboost	85%, mixed with controls
Chupin, NI (2007)	deform	Manual seeding, detection of anatomical landmark	86%
Barnes, NI (2008)	m-atlas	Template library + morphological operation	86%
Schizophrenia			
Khan, NI (2008)	atlas	FreeSurfer initialized, large deformation diffeomorphic mapping	77%
Pohl, TMI (2007)	class	Hierarchical expectation-maximization	81%

Journal abbreviation: JDI=Journal Digital Imaging, NI=NeuroImage, HBM: Human Brain Mapping, TMI=IEEE Trans Medical Imaging, JIST=Journal of Imaging Science and Technology.

Segmentation Category: atlas=atlas-based, appear=appearance-based, deform=deformation-based, class=classification-based approach, m-atlas=multi-template (or template library and label fusion)-based

Chapter 3

Quantitative analysis of morphological changes in mesiotemporal lobe structures using computational models

3.1 Unified preface

For the last two decades, the most common quantitative tool to assess mesiotemporal lobe pathology in TLE has been MRI volumetry, as hippocampal atrophy is considered a marker of hippocampal sclerosis and detecting this abnormality correctly lateralizes the seizure focus in 70-80% of patients (Cascino et al., 1992a; Cendes et al., 1997; Jack et al., 1992). Since this method provides a global estimate of atrophy, however, its sensitivity to detect subtle diffuse or focal anomalies is limited. Indeed, in up to 30% of patients, hippocampal

volumetry is unremarkable despite the presence of mild degrees of sclerosis on histology (Bernasconi et al., 2001; Jackson et al., 1994).

Histopathological examination of autopsy brain specimens (Margerison and Corsellis, 1966; Meencke and Veith, 1991) and subsequent microscopic neuronal counting (Babb et al., 1984; Blümcke et al., 2007; Bruton, 1988; de Lanerolle et al., 2003; Thom et al., 2002a) have shown severe and selective CA1 neuronal loss in the vast majority of patients with hippocampal sclerosis. Non-uniform, focal neuronal loss and gliosis have also been found in the amygdala and the entorhinal cortex (Yilmazer-Hanke et al., 2000).

Since atrophy only reflects a single morphological characteristic, it may be insufficient to fully describe pathology. Indeed, malrotation, thought to be secondary to incomplete folding of the fetal hippocampus, may increase the susceptibility to TLE (Bernasconi et al., 2005a). On MRI, such developmental anomalies are characterized as atypical hippocampal shape and positioning, and an abnormally deep collateral sulcus (Bernasconi et al., 2005a). Furthermore, hippocampal malrotation may co-occur with unusual gyrifications in the surrounding cortices, as early fetal pathological mechanisms affecting its development may also trigger morphological alterations in neighboring areas. Notably, the complexity of brain anatomy hampers visual identification of these anomalies, particularly when they co-occur with atrophy.

Advanced surface-based shape models, including spherical harmonics description combined with point distribution models (SPHARM-PDM) (Styner et al., 2006), medial surface models (Styner et al., 2003), cortical surface models and sulcal ribbon models (Mangin et al., 2004), have allowed for the identification and the pattern classification of local morphological changes that might not be readily visible on MRI.

In this chapter, we developed advanced surface-based morphometric methods to statistically assess mesiotemporal pathology that have not been previously identifiable on MRI and that are not evident through the measurement of total volume or by visual evaluations. We first designed a surface-based framework

that allows independent quantification of small-scale focal atrophy, positional changes and sulcal alterations, and then investigated their clinical significance by applying them to a large database of TLE patients and healthy controls.

3.2 Manuscript 1

Published in *Med. Image. Comp. Comp. Assist. Interv.* 2008. 5241(Pt 1),
Med. Image. Comp. Comp. Assist. Interv. 2011. 6892(Pt 2)

Submitted to *Neuroimage*.

Hippocampal surface-based shape analysis: disentangle positional differences from volume changes

Hosung Kim^{1,2}, Tommaso Mansi³, Andrea Bernasconi², Neda Bernasconi²

¹Department of Biomedical Engineering, ²Department of Neurology and
Neurosurgery and Brain Imaging Center, McGill University, Montreal
Neurological Institute and Hospital, Montreal, Quebec, Canada and ³ Siemens
Corporate Research, Image Analytics and Informatics, Princeton, NJ, USA

Abstract

Hippocampal atrophy and developmental positional variants may co-occur in various neurological disorders. Advanced surface-based shape models including the spherical harmonics combined with point distribution models (SPHARM-PDM) accurately localize morphological changes that may not be readily visible. The displacement metric provided by these approaches, however, does not allow differentiating volume changes from positional differences. Here, we propose a surface-based framework to analyze independently volume and positioning. After extracting SPHARM-PDM from manual labels, we computed displacement vectors between individual surfaces and the template. Then, we computed surface-based Jacobian determinants (SJD) from these vectors to localize volume changes. To analyze positional variants, we constructed a mean meridian axis (MEMAX), inheriting the shape-constrained point correspondences of SPHARM, on which we compute local curvatures and position vectors. We validated our method on synthetic shapes and a large database of healthy subjects and patients with temporal lobe epilepsy (TLE). For synthetic data, our SJD and MEMAX accurately and separately quantified simulated local volume changes, shifting and bending. Also, varying kernel and sample sizes demonstrated that our approach is able to detect fine-scale subtle changes. For patients with temporal lobe epilepsy, our comprehensive analysis showed that atrophy and positional changes co-occurred at the level of the posterior hippocampus. In particular, while SPHARM-PDM showed mirrored deformations in that region, SJD detected atrophy, and shape analysis of MEMAX unveiled medial positioning due to bending. Such multiple shape abnormalities were detected also in patients with malformations of cortical development (MCD). Moreover, our metrics revealed the location of changes were more anterior than in TLE. Given that medial positioning is a known feature of developmental abnormalities and may emerge prior to hippocampal sclerosis, disentangling positioning anomalies from atrophy may provide new insights in the pathogenesis of a variety of other brain disorders, such as schizophrenia and autism, in which mesiotemporal lobe is implicated and these morphometric characteristics coexist.

Introduction

For the last two decades, MRI volumetry has been the most commonly employed quantitative technique to assess mesiotemporal lobe pathology. More recently, advanced surface-based shape models have been proposed to assess morphometric changes not evident in measurement of total volume. These techniques, including deformation-based mapping (Csernansky et al., 2000; Hogan et al., 2006; Posener et al., 2003; Wang et al., 2001) and spherical harmonics description combined with point distribution models (SPHARM-PDM) (Styner et al., 2006), have allowed localization of subtle pathology (Hogan et al., 2004). Yet, the displacement metric provided by these approaches is unable to differentiate volume changes from positional differences. Shape models based on the medial surface (*i.e.*, the central path of a 3D object), on the other hand, allow quantifying local positional variations (Joshi et al., 2002; Styner et al., 2004). Yet, as these methods rely on coarse-scale sampling, they may lack sensitivity to assess high-dimensional features, making a biologically meaningful interpretation of findings difficult.

Hippocampal atrophy and atypical shape and positioning of the hippocampus are prevalent in temporal lobe epilepsy (TLE) and epileptic syndromes related to malformations of cortical development (MCD) (Baulac et al., 1998; Bernasconi, 2006; Bernasconi et al., 2005b; Jackson et al., 1990; Kuchukhidze et al., 2010; Montenegro et al., 2006; Raymond et al., 1995; Voets et al., 2011). In addition, such morphometric anomalies have been reported in other neurological disorders, in which the pathogenetic mechanisms involve the temporal lobe, such as schizophrenia (Connor et al., 2004) and autism (Salmond et al., 2005). In a previous work, we proposed a methodology to quantify local volume changes based on the computation of surface-based Jacobian determinants (Kim et al., 2008b). Our preliminary results in a small cohort of TLE patients localized subtle atrophy successfully, but failed to dissociate volume from positional anomalies.

We propose a surface-based framework to analyze independently volume and positioning. To this purpose, we computed Jacobian determinants to measure local volume changes and constructed a medial axis model that inherits the shape-constrained point correspondence of SPHARM-PDM to quantify fine-scale local position and curvature. We first evaluated the sensitivity and specificity of our approach using synthetic shapes. We then statistically assessed morphological variations of the hippocampus in two large cohorts of epileptic patients with TLE and MCD, and compared them to healthy controls.

Methods

Subjects

From our database of patients referred to the Montreal Neurological Institute for the investigation of drug-resistant epilepsy, we selected 78 patients with TLE (34 males; mean age: 36 ± 10 , range: 17-57) and 91 patients with malformations of cortical development (MCD; 39 males; mean age: 29 ± 9 , range: 13-58) who had a high-resolution T1-weighted 3D MRI and hippocampal volumetry. The MCD population included patients with focal cortical dysplasia (FCD, $n=30$), heterotopia (HET, $n=41$), and polymicrogyria (PMG, $n=20$). In none of the MCD patients the cortical malformations invaded the hippocampal formation.

Demographic and clinical data were obtained through interviews with the patients and their relatives. Diagnosis and lateralization of the seizure focus were determined by a comprehensive evaluation including video-EEG recordings and MRI evaluation in all patients. In TLE, the seizure focus was left-sided in 34 patients and right-sided in 44. Sixty seven patients underwent surgery. Mean follow-up time was 3.4 ± 3.1 years. We determined surgical outcome according to Engel's classification (Engel et al., 1993). 51 (76%) patients had Class I outcome, 5 (8%) class II, 7 (10%) Class III, and 4 (6%) Class IV. Following qualitative histopathological analysis (Meencke and Veith, 1991), hippocampal sclerosis

was detected in all 44 patients in whom specimens were available. In the remaining 23 patients, hippocampal specimens were either incomplete or unsuitable for examination due to subpial aspiration.

The control group consisted of 46 age- and sex-matched (23 males; mean age: 32 ± 12 years, range: 20-56) healthy individuals. The Ethics Committee of the Montreal Neurological Institute and Hospital approved the study and written informed consent was obtained from all participants.

MRI acquisition and processing

MR images were acquired on a 1.5 T Gyroscan (Philips Medical Systems, Eindhoven, The Netherlands) using a 3D T1-fast field echo sequence (TR=18 ms; TE=10 ms; NEX=1; flip angle=30°; matrix size=256×256; FOV=256×256 mm²; slice thickness=1 mm), providing an isotropic voxel of 1mm³ volume. Prior to processing, images underwent automated correction for intensity non-uniformity and intensity standardization (Sled et al., 1998). The hippocampus was segmented manually according to our previously published protocol (Bernasconi et al., 2003b). Prior to segmentation, MR images were linearly registered into a standardized stereotaxic space based on the Talairach atlas (Collins et al., 1994). Hippocampal volumes were normalized through a z-transform relative to the corresponding distribution of healthy controls. Based on 2 standard deviations below mean absolute volume and inter-hemispheric asymmetry of healthy controls all TLE patients showed hippocampal atrophy ipsilateral to the seizure focus. Among MCD patients, 15% (9/30) with FCD, 20% (16/41) with HET, and 15% (6/20) with PMG had unilateral hippocampal atrophy.

Spherical harmonic description and point distribution model (SPHARM-PDM)

Manually segmented hippocampal labels were converted to surface meshes and parameterized using SPHARM-PDM, an area-preserving and distortion-

minimizing spherical mapping that ensures point-wise correspondence through an icosahedron subdivision (Styner et al., 2006). SPHARM-PDM surfaces of each individual were rigidly aligned to a template constructed from the mean surface of controls and patients with respect to the centroid and the longitudinal axis of the 1st order ellipsoid (Gerig et al., 2001). To correct for differences in overall interior head size across subjects, each individual surface were inversely scaled with respect to its intra-cranial volume (Styner et al., 2006). Vertex-wise displacement vectors were then calculated between each individual and the template (Styner et al., 2006). The surface normal components of these vectors are used to quantify inward and outward deformations. SPHARM-PDM was computed based on 12 degrees spherical basis functions and 10-level icosahedron subdivision (1002 vertices), as recommended by (Styner et al., 2006).

Surface-based analysis of volume changes

In the following sections, we describe the computation of vertex-wise Jacobian determinant metric to quantify volume changes. In brief, we apply the heat equation to interpolate the vertex-wise displacement vectors within the volume domain enclosed by the surface boundary. The Jacobian determinant is then calculated from this interpolated vector field and projected back onto the SPHARM-PDM surface. Finally, after subtracting 1 from the Jacobian determinant, growth ($J > 0$) or shrinkage ($J < 0$) of a unit-size cube is quantified along the surface-normal direction.

From surface-based displacement vectors to volume-based displacement field. We employ the heat equation, a partial differential equation that describes the propagation of a scalar value in a given region over time (Evans, 2010) For a scalar function u of three spatial variables x, y, z in the Cartesian coordinate system, and a time variable t , the heat equation is:

$$\frac{\partial u}{\partial t} = \alpha \left(\frac{\partial^2 u}{\partial x^2} + \frac{\partial^2 u}{\partial y^2} + \frac{\partial^2 u}{\partial z^2} \right) = \alpha \Delta u \quad (1)$$

where α is a constant called conductivity and Δ is the Laplacian operator.

This equation diffuses the scalar values located at a boundary (Dirichlet boundary condition) over a volume domain by minimizing the sum of gradient changes so that smooth fields are obtained at the equilibrium status. This equation can be extended to diffuse vectors. Let us $\mathbf{u} = (u_x, u_y, u_z)$ be a displacement vector at the spatial position (x,y,z) . The variation of \mathbf{u} at time t is defined as:

$$\frac{\partial \mathbf{u}}{\partial t} = \left(\frac{\partial u_x}{\partial t}, \frac{\partial u_y}{\partial t}, \frac{\partial u_z}{\partial t} \right) = (\alpha \Delta u_x, \alpha \Delta u_y, \alpha \Delta u_z) \quad (2)$$

Solving this equation until convergence ($\partial u / \partial t \rightarrow 0$) smoothly diffuses the displacement vectors \mathbf{u} within the volume enclosed by \mathbf{S} .

Implementation of heat equation surface-to-volume interpolation on discrete space. In practice, the heat equation is solved on a regular grid lattice that embeds the surface \mathbf{S} . Let $\{s_1, s_2, \dots, s_M\}$ be the set of M vertices of the surface \mathbf{S} in the 3D continuous coordinate system \mathbf{R}^3 and $\mathbf{\Omega} = (x,y,z)$ a 3D discrete control lattice overlaid on \mathbf{R}^3 . The origin $(0,0,0)$ coincides with these two coordinates. The unit lattice in $\mathbf{\Omega}$ is controlled by the spacing h , i.e., $\mathbf{R}^3 = (h a, h b, h c)$ is mapped at $\mathbf{\Omega} = (a, b, c)$ (**Figure 3.1A**).

We specify $\mathbf{u}_s = \{ \mathbf{u}_{s1}, \mathbf{u}_{s2}, \dots, \mathbf{u}_{sM} \}$ as a set of displacement vectors on \mathbf{S} (calculated using SPHARM-PDM) and a surface point \mathbf{s}_i located within the cube defined by its 8 adjacent control points on $\mathbf{\Omega}$. To compute the heat equation on $\mathbf{\Omega}$ with the boundary condition $\mathbf{u}_s(t) = \mathbf{u}_s$, we linearly interpolate \mathbf{u}_{s_i} at all neighboring control lattices in $\mathbf{\Omega}$. Let $\mathbf{x}=(x, y, z)$ on $\mathbf{\Omega}$ be one of the 8 neighboring points and $d(\mathbf{x}, \mathbf{s}_i)$ the Euclidean distance between \mathbf{x} and \mathbf{s}_i . Observe that \mathbf{x} may have one or more adjacent surface points (e.g., $\mathbf{s}_{i-1}, \mathbf{s}_i, \mathbf{s}_{i+1}$, **Figure 3.1B**).

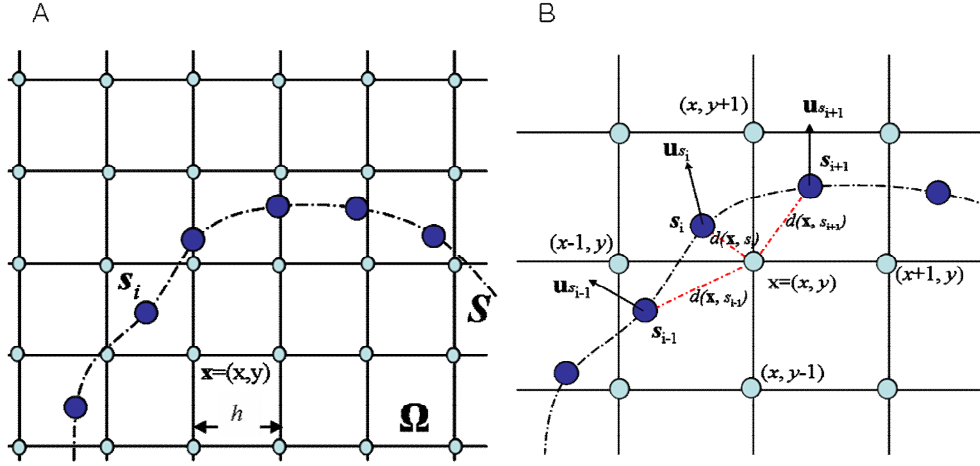


Figure 3.1. Heat equation surface-to-volume interpolation on discrete space.

A. Schematic 2D representation of surface vertices overlaid on a discrete rectangular control lattice Ω . 'h' indicates the lattice spacing. **B.** A vector \mathbf{u}_x is interpolated from displacement vectors on surface vertices ($\mathbf{u}_{s_{i-1}}$, \mathbf{u}_{s_i} , $\mathbf{u}_{s_{i+1}}$) adjacent to \mathbf{x} .

We adopt a general interpolation method to compute \mathbf{u}_x at \mathbf{x} by iteratively updating \mathbf{u}_x according to all the s_i of \mathbf{S} such that $d(\mathbf{x}, s_i) < h$. In the 1st iteration, \mathbf{u}_x^1 is determined as:

$$\mathbf{u}_x^1(t) = \mathbf{u}_{s_i}, A_d^1 = d(\mathbf{x}, s_i) \quad (3)$$

A_d^1 is used to update \mathbf{u}_x^2 as:

$$\mathbf{u}_x^2 = \frac{\mathbf{u}_{s_{i+1}} \cdot A_d^1 + \mathbf{u}_x^1 \cdot d(\mathbf{x}, s_{i+1})}{A_d^1 + d(\mathbf{x}, s_{i+1})} \quad (4)$$

At the n-th iteration, \mathbf{u}_x is updated from $\tilde{\mathbf{u}}_x$ according to:

$$\mathbf{u}_x^n = \frac{\mathbf{u}_{s_{i+n-1}} \cdot A_d^{n-1} + \mathbf{u}_x^{n-1} \cdot d(\mathbf{x}, s_{i+n-1})}{A_d^{n-1} + d(\mathbf{x}, s_{i+n-1})} \quad (5)$$

where A_d^{n-1} is given by:

$$A_d^{n-1} = \frac{A_d^{n-2} \cdot (n-2) + d(\mathbf{x}, \mathbf{s}_{i+n-2})}{n-1} \quad (6)$$

The recurrence is performed until $n=N$, where N is the number of vertices that satisfy $d(\mathbf{x}, \mathbf{s}) < h$. Under the boundary conditions determined by (5), the discrete heat equation on Ω is solved using finite differences:

$$\begin{aligned} \mathbf{u}_x(t) &= \mathbf{u}_x(t-1) + \Delta \mathbf{u}_x(t-1) \\ &= \mathbf{u}_x(t-1) + \frac{1}{6} (\mathbf{u}(x-1, y, z, t-1) + \mathbf{u}(x+1, y, z, t-1) + \\ &\quad \mathbf{u}(x, y-1, z, t-1) + \mathbf{u}(x, y+1, z, t-1) + \\ &\quad \mathbf{u}(x, y, z-1, t-1) + \mathbf{u}(x, y, z+1, t-1) - 6\mathbf{u}(x, y, z, t-1)) \end{aligned} \quad (7)$$

The final volume-based displacement fields on Ω are obtained at convergence, which is reached when:

$$\sum_{\Omega} \frac{\partial \mathbf{u}_x}{\partial t} = \sum_{\Omega} \|\mathbf{u}_x(t) - \mathbf{u}_x(t-1)\| < \alpha \quad (8)$$

In (8), the threshold α is set empirically as 10^{-5} .

Vertex-wise localization of volume changes. Local volume changes are quantified by calculating the Jacobian determinant J_s on the previously interpolated vector field, as defined by:

$$J_s = \det(\mathbf{I} + \nabla \mathbf{u}_s) = 1 + tr(\nabla \mathbf{u}_s) + \det_2(\nabla \mathbf{u}_s) + \det(\nabla \mathbf{u}_s) \quad (9)$$

where tr is the trace operator and $\det_2(\nabla \mathbf{u}_s)$ is the sum of 2x2 principal minors of $\nabla \mathbf{u}$.

For the vector fields produced by an isotropic diffusion, which assumes no shear deformation, the higher order terms approach zero (Chung et al., 2001a). Therefore, we can use the first order approximation $J \approx 1 + tr(\nabla \mathbf{u}_s)$. For the

analysis of directional changes along the surface normal, we simplify the approximated Jacobian at a surface point s_i as:

$$J_{s_i} = 1 + tr(\nabla \mathbf{u}_{s_i} \cdot \mathbf{n}_{s_i}) = 1 + (\mathbf{u}_{s_i} - \mathbf{u}_{s_i}) \cdot \mathbf{n}_{s_i} \quad (10)$$

where \mathbf{n} is the unit outward surface normal, $\hat{\mathbf{s}}_i = \mathbf{s}_i - \mathbf{n}$, and \mathbf{u}_{s_i} and \mathbf{u}_{s_i} are determined from the displacement fields on Ω (7) using tri-linear interpolation. Subtracting 1 from the equation (10) yields the modified Jacobian metric that explains growth ($J > 0$) or shrinkage ($J < 0$) of a unit-size cube through the surface-normal direction.

Construction of the medial axis

Conventional approaches create the central path of a 3D object by joining points that are equidistant from the object's boundary (Joshi et al., 2002; Styner et al., 2003; Styner et al., 2004). Inter-subject point correspondence is achieved through deformation of all individual skeletons into a common spatial frame by a thin plate registration (Styner et al., 2003). Registration and resampling may introduce biases in the subsequent analysis steps. In our approach, we parameterize the prime meridians of the object's two hemispheres using latitudes and longitudes parameters of SPHARM-PDM (**Figure 3.2A-B**). Finally, we create a central "route" by pair-wise averaging of the prime meridians. This process allows the central "route" to inherit the shape-constrained correspondence of the SPHARM-PDM, thus minimizing biases, mainly those related to registration.

Geometric parameters of SPHARM. The spherical harmonic basis functions Y_l^m of degree l and order $-l \leq m \leq l$ are defined by the spherical coordinates θ, ϕ as:

$$Y_l^m(\theta, \phi) = \sqrt{\frac{2l+1(l-m)!}{4\pi(l+m)!}} P_m^l(\cos\theta) e^{im\phi} \quad Y_l^{-m}(\theta, \phi) = (-1)^m Y_l^{m*}(\theta, \phi) \quad (11)$$

In (11), Y_l^{m*} denotes the complex conjugate of Y_l^m and P_l^m the associated Legendre polynomials (Styner et al., 2006). Summation of the spherical harmonics from 1 to L degree approximates a given structural boundary to a surface. A vertex point \bar{s} on \mathbf{S} is then uniquely determined by:

$$\bar{s}(x, y, z) = \bar{s}(x(\theta, \phi), y(\theta, \phi), z(\theta, \phi)) = \sum_{l=1}^L \sum_{m=-l}^l \bar{c}_l^m Y_l^m(\theta, \phi) \quad (12)$$

The 3D weight vectors \bar{c}_l^m are computed through least-square minimization. θ, ϕ define latitudes and longitudes, respectively (yellow and green in **Figure 3.2A-B**). Accordingly, $\bar{s}(0, \pi/2)$ and $\bar{s}(\pi, \pi/2)$ indicate the poles, and $\bar{s}(\pi/2, \phi)$ the equator (Styner et al., 2006).

Mean meridian axis (MEMAX). The functions $\bar{s}(\theta, 0)$ and $\bar{s}(\theta, \pi)$ in (12), describe a set of points that constitute the prime meridian (blue in **Figure 3.2A-B**). The prime meridian points on a given hemisphere $\mathbf{s}(\theta) = \bar{s}(\theta, 0 \text{ or } \pi)$ and their counterparts on its opposite side $\hat{\mathbf{s}}(\theta) = \bar{s}(\pi - \theta, 0 \text{ or } \pi)$ are averaged in a pair-wise fashion, thus yielding a mean meridian axis \mathbf{M} , henceforth called MEMAX (red in **Figure 3.2C**) as the skeleton of a shape. To perform shape analysis, we sample K points on \mathbf{M} . We define $\mathbf{M}(k)$, where $k = \{k \mid 1, 2, \dots, K\}$, using equidistant subdivisions of θ , that is:

$$\begin{aligned} \mathbf{M}(k) &= \left\{ \bar{s}\left(\frac{\pi}{2} - \frac{\pi}{2} \times \frac{2k}{K}, 0\right) + \bar{s}\left(\frac{\pi}{2} + \frac{\pi}{2} \times \frac{2k}{K}, 0\right) \right\} / 2, \text{ if } 1 \leq k \leq K/2 \\ &= \left\{ \bar{s}\left(\frac{\pi}{2} \times \frac{2(k - K/2)}{K}, \pi\right) + \bar{s}\left(\frac{\pi}{2} + \frac{\pi}{2} \times \frac{2(k - K/2)}{K}, \pi\right) \right\} / 2, \text{ if } K/2 \leq k \leq K \end{aligned} \quad (13)$$

$\mathbf{M}(k)$ is defined separately in the first and second half ranges of k to ensure the continuity of the MEMAX parameterization.

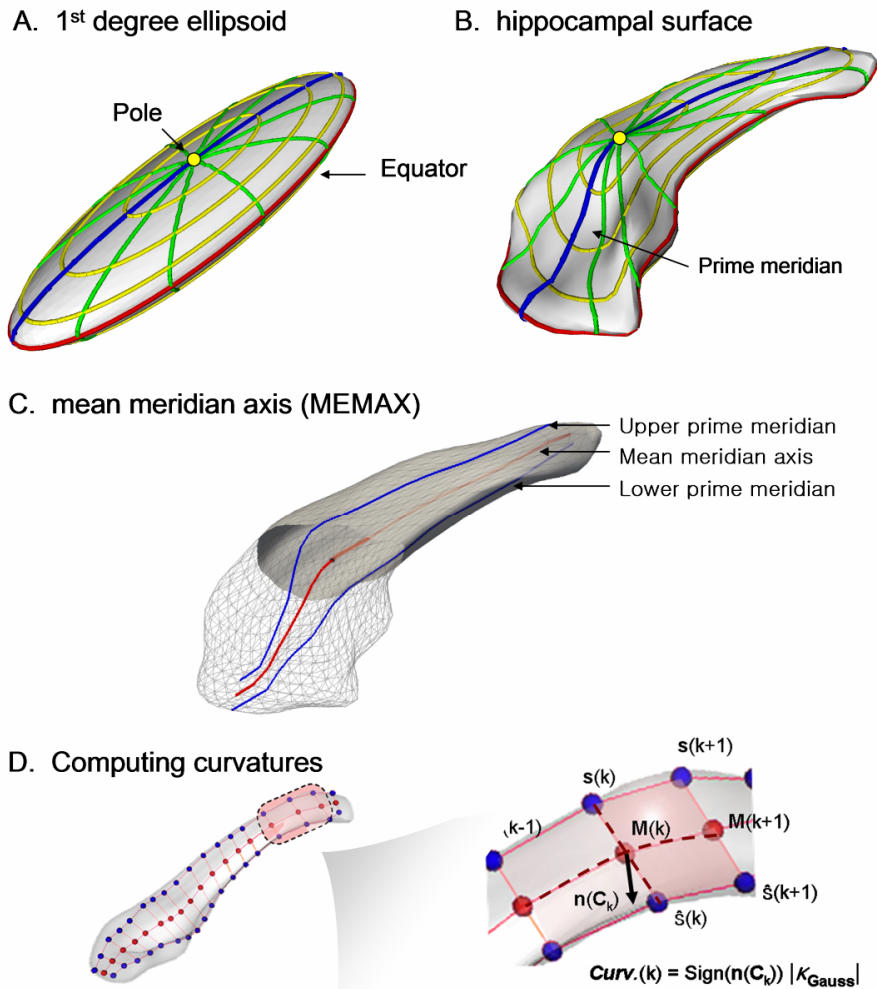


Figure 3.2. Modeling mean meridian axis.

A. The SPHARM function defined by two spherical harmonic coefficients $\bar{s}(\theta, \phi)$, representing the latitude (yellow) and the longitude (green) are mapped on the 1st degree ellipsoid surface. The prime meridian (blue) presents the longitude when $\phi = 0$ or π . **B.** After computing 12 degree spherical basis functions for the hippocampus, coefficients are repositioned while preserving shape-inherent properties. **C.** $\bar{s}(\theta, 0)$ and $\bar{s}(\theta, \pi)$ describe a set of points that constitute the upper and lower prime meridians (blue) on the surface, respectively. The geometric mean of the two half-meridians produces the mean meridian axis (MEMAX, red). **D.** To compute local curvature of the MEMAX, we first project the $\mathbf{M}(k)$ on a curved open surface C defined by the prime meridians $\mathbf{s}(k)$ and $\hat{\mathbf{s}}(k)$. We then calculate a surface-based Gaussian curvature κ_{Gauss} at each control point $\mathbf{M}(k)$ on C .

Assessing local positioning changes

To assess shifting, group analysis is performed by comparing the location of each sample point on the MEMAX's \mathbf{M} using Hotelling T^2 metric (Seber, 1984), defined by:

$$T^2 = (\mu_1 - \mu_2)' \left(\sum_1 \frac{1}{n_1} + \sum_2 \frac{1}{n_2} \right)^{-1} (\mu_1 - \mu_2) \quad (14)$$

In this equation, μ_1, μ_2 are the group mean position vectors, \sum_1, \sum_2 the group-separated covariance matrices and n_1, n_2 the number of samples in groups 1 and 2.

We also analyze MEMAX curvature. In general, the curvature of a 3D curve at a given point (x,y,z) is computed using the Frenet-Serret formula (Spivak, 1999). This measurement, however, provides only the degree of curving without distinguishing convexity from concavity, thus requiring additional visual inspection to fully understand its nature. Instead, we propose to measure the signed curvature varying along the normal directions of a surface defined by the prime meridians. We create an open surface \mathbf{C} where its boundaries are defined by the prime meridian $\mathbf{s}(k)$ and $\hat{\mathbf{s}}(k)$. Since the MEMAX $\mathbf{M}(k)$ is a geometric mean of the two prime meridians, $\mathbf{M}(k)$ is placed in the middle $\mathbf{s}(k)$ and $\hat{\mathbf{s}}(k)$ on the surface \mathbf{C} (**Figure 3.2D** left). We then calculate the Gaussian curvature κ_{Gauss} at each sample point $\mathbf{M}(k)$ on \mathbf{C} (**Figure 3.2D** right). To differentiate the convexity (+) from the concavity (-), signs are computed using the surface normal vector of the k_{th} facet on \mathbf{C} , $\mathbf{n}(\mathbf{C}_k) = (\mathbf{M}(k+1) - \mathbf{M}(k)) \times (\mathbf{s}(k) - \hat{\mathbf{s}}(k))$, as:

$$\text{Sign}(\mathbf{n}(\mathbf{C}_k)) = \text{Sign}(\mathbf{n}(\mathbf{C}_k) \bullet \mathbf{n}(\mathbf{C}_{k+1}) / \|\mathbf{n}(\mathbf{C}_k)\| \cdot \|\mathbf{n}(\mathbf{C}_{k+1})\|) \quad (15)$$

The signed curvature is finally determined as:

$$\kappa = \text{Sign}(\mathbf{n}(\mathbf{C}_k)) |\kappa_{\text{Gauss}}| \quad (16)$$

where κ_{Gauss} is the Gaussian curvature.

Experiments and Results

Synthetic data

We created a rounded cylindrical volume (**Figure 3.3A-C**) with a resolution of $0.25 \times 0.25 \times 0.25 \text{ mm}^3$ and applied: *i*) bending, *ii*) local shifting (4.0 mm), and *iii*) simultaneous local shrinking (0.5 mm) and shifting (4.0 mm).

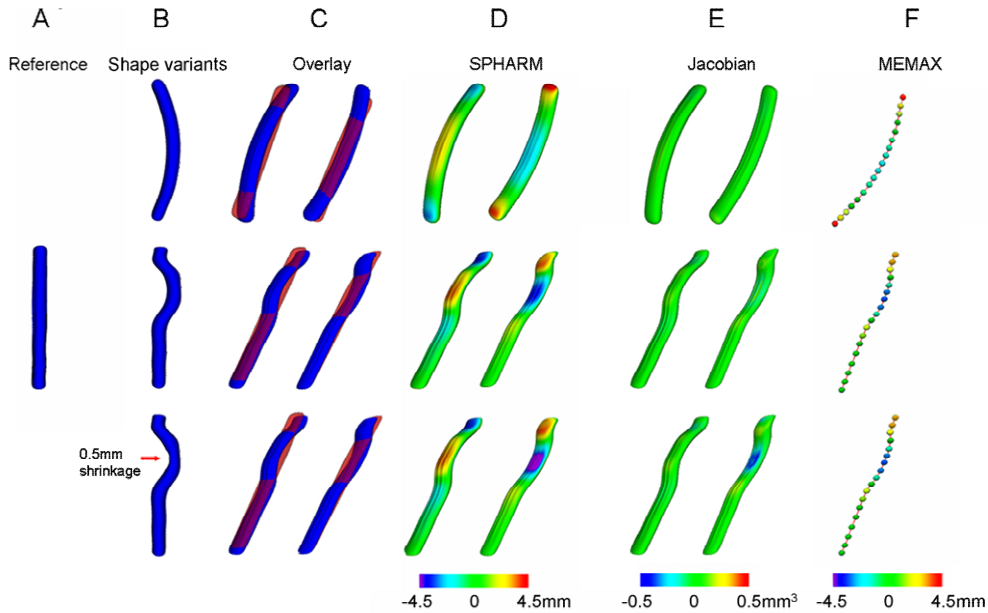


Figure 3.3. Analysis of synthetic data.

A. Reference object. **B.** Shape variants: bending (top), localized shifting (middle), simultaneous shifting and shrinkage (bottom). **C.** Deformed objects (solid blue) aligned to the reference (transparent red). **D.** Surface-normal components of the displacement vectors of SPHARM (in mm, $-/+$ indicate inward/outward deformation). **E.** Surface-based Jacobian determinant (in mm^3 , $-/+$ indicate volume loss/growth). **F.** MEMAX localizing positional changes (in mm) compared to the reference.

We first extracted the SPHARM-PDM surfaces and calculated the displacement vectors. In this experiment, we choose the number of SPHARM-PDM vertices by setting the mean inter-vertex distance approximately 0.25 mm to avoid any bias due to oversampling. Then, at each vertex, we computed a signed surface-normal component of the displacement vector (SNV) and a surface-based

Jacobian determinant (SJD) as a metric of local volume change. The MEMAX were extracted from all shapes. Finally, we quantified point-wise positioning of the variants compared to the reference.

To investigate the influence of the heat equation interpolation grid size (*i.e.*, the spacing h in the control lattice Ω) in detecting volume changes, we measured SJD with respect to different h ranging from 0.125 to 4.0mm. For this experiment, SJD was computed from the displacement vectors between the reference object and its variant deformed by the above-mentioned simultaneous local shifting and shrinkage. For each grid size, we measured the mean SJD in an ROI defined by the vertices on which we modeled the 0.5mm shrinkage, and computed the following modified standard error (MSE) over the entire object:

$$MSE = \sum_{ROI} |SJD - (-0.5)| / n_{ROI} + \sum_{\overline{ROI}} |SJD| / n_{\overline{ROI}} \quad (17)$$

where n is the number of vertices within the ROI or outside it (\overline{ROI}). The MSE tends to 0 when SJD maximally detects the expected 0.5mm shrinkage in ROI and minimally detects noises in non-ROI.

Influence of interpolation grid size on detecting predefined atrophy. The applied volume shrinkage was detected well with a grid size ranging from $0.25 \times 0.25 \times 0.25$ (mean SJD: 0.53) to $0.5 \times 0.5 \times 0.5 \text{ mm}^3$ (mean SJD: 0.49; **Figure 3.4A left**), in which mean SJD error did not exceeded 0.03 mm^3 (6%). The minimum MSE was obtained at the grid size of $0.5 \times 0.5 \times 0.5 \text{ mm}^3$ (**Figure 3.4A right**). Thus, for the subsequent analyses, we used spacing $h=0.5 \text{ mm}$.

Shape analysis. The SNV showed mirrored inward/outward deformations on facing surfaces reflecting bending and shifting (**Figure 3.3D**, top and middle). In case of simultaneous local shrinking and shifting, SNV did not enable one to differentiate shrinkage from shifting (**Figure 3.3D**, bottom). Contrary to SNV, SJD was not influenced by bending and shifting (**Figure 3.3E**, top and middle) and accurately localized the 0.5 mm local shrinkage (**Figure 3.3E**, bottom).

Analysis of MEMAX detected bending and local shifting only (**Figure 3.3F**), and was robust to shrinking (**Figure 3.3F**, middle and bottom).

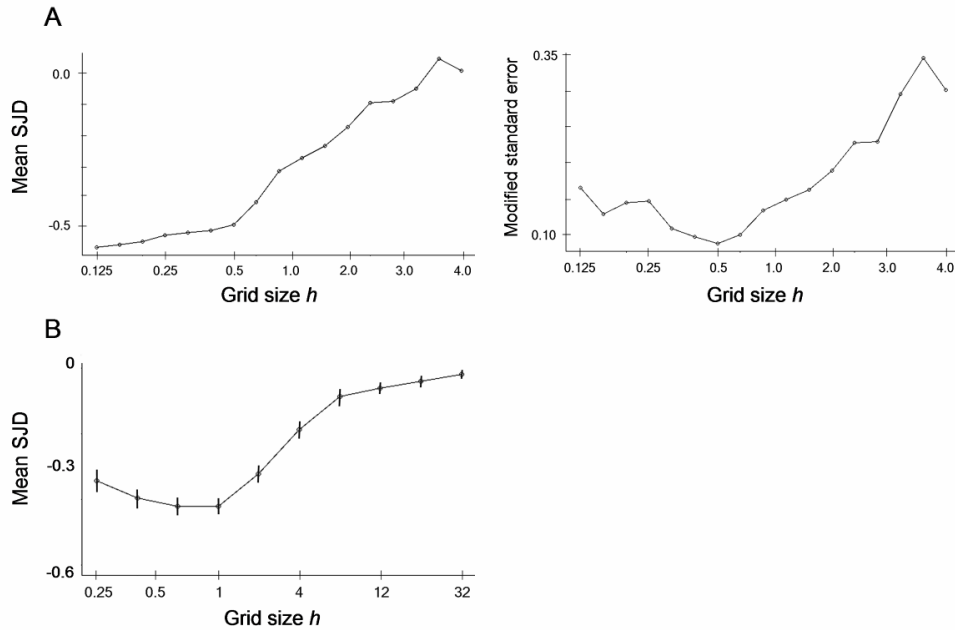


Figure 3.4. Graphs displaying the relationship between the grid size of the heat equation interpolation (h) and the sensitivity in detecting atrophy. In **A**, h is related to mean surface-based Jacobian determinant (SJD) computed in the ROI where the 0.5mm shrinkage was applied (see **Figure 3.3**). Modified standard error (MSE) over the entire object is minimized at $h=0.5$ mm. In **B**, h is related to mean SJD across all vertices in patients. The standard deviation is displayed at each grid size.

Shape analysis of the hippocampus in epilepsy

Parameter optimization

a. Interpolation of the grid size of the surface-based Jacobian determinant. We investigated the influence of the heat equation interpolation grid spacing h on the sensitivity to detect hippocampal atrophy. We iteratively varied h ranging from 0.25 to 32mm, that is the approximate average length of the hippocampus (MacMaster and Kusumakar, 2004). At each iteration, we computed the SJD between the ipsilateral hippocampus in each TLE patient and the template and measured mean and standard deviation (SD) across vertices.

The SJD was most sensitive and most reliable in detecting hippocampal atrophy at the grid spacing of 1 mm. Indeed using this grid size, we detected the maximum atrophy (-0.42mm^3), while keeping SD to a minimum (0.03mm^3) (**Figure 3.4B**). At a grid spacing $h \geq 8\text{mm}$, the detected atrophy was $<-0.1 \text{mm}^3$. Thus, for the subsequent analyses, we used $h=1 \text{mm}$.

b. Sampling scale along MEMAX. We first extracted the MEMAX of the right hippocampi in controls and patients with RTLE. We then evaluated the effect of varying the total number of sample points ($N_s = 2-36$) on the sensitivity to detect positional changes (*i.e.*, position vectors and Gaussian curvatures). For each individual and each metric, we averaged all sample points. We then performed group-wise Hotelling T^2 test on the mean position vectors and Student's t-test on the mean curvatures.

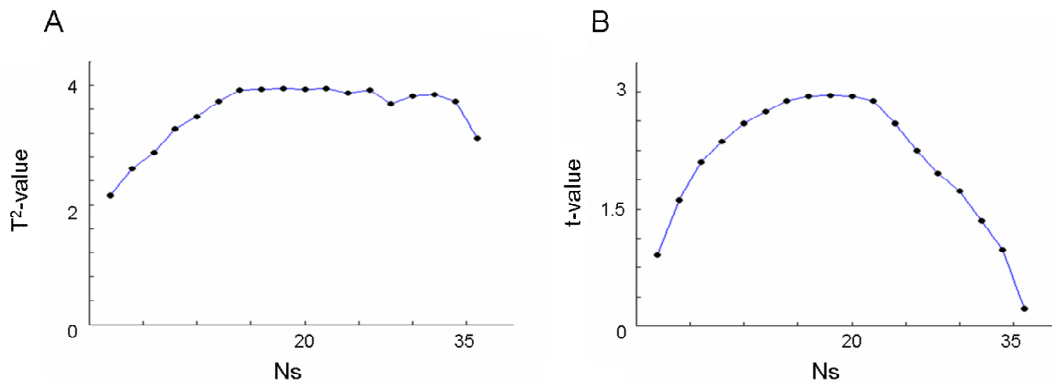


Figure 3.5. Relationship between sampling points (N_s) along MEMAX and sensitivity in detecting shifting (**A**) and bending (**B**) in TLE patients. See Text for details.

Results are shown in **Figure 3.5A** and **B**. Comparing groups, we detected shifting in TLE with N_s ranging from 14 to 34 ($T^2 > 3.6$) and bending with N_s ranging from 14 to 22 ($t > 2.82$). The mean inter-point distance spanned from 2.1 to 3.3 mm. The sampling along MEMAX that provided the most significant group differences was $N_s = 18$ ($T^2 = 3.71$; $t = 2.85$). Thus, for the subsequent analyses, we used 18 points, with a mean inter-point distance of 2.7 mm.

Group analysis in patients. We performed vertex-wise group comparisons (*i.e.*, each patient group vs. controls) of surface-normal component of the displacement vector (SNV), surface-based Jacobian determinant (SJD) and Gaussian curvatures using Student's t-test. We carried out point-wise comparisons of positional vectors using Hotelling T²-test. All analyses were corrected for multiple comparisons using the false discovery rate (FDR) (Benjamini and Hochberg, 1995). To localize changes, we schematically outlined hippocampal subfields on the surface template according to histological parcellations (Duvernoy, 2005).

Results in TLE are shown in **Figure 3.6**. Group-wise differences in shape were quite similar in patients with left and right TLE. Ipsilateral to the seizure focus, both SNV and SJD revealed widespread inward deformation and atrophy respectively corresponding to CA1 subfield in hippocampal head and body (FDR<0.001; **Figure 3.6A-B**). In the tail, the *mirrored* inward/outward deformations detected by SNV corresponded to atrophy as shown by the SJD analysis. In addition, SJD detected small areas of CA1 inward deformations (FDR<0.05) in the contralateral hippocampus.

Curvature analysis of the mean meridian axis (MEMAX) detected ipsilateral bending towards the mid-sagittal plane (LTLE: 1 sample point, FDR=0.04; RTLE: 2 sample points, FDR<0.05; **Figure 3.6D**), at the level of hippocampal tail. We also found ipsilateral medial shifting at the level of the tail (LTLE: 3 points, FDR<0.01; RTLE: 6 points, FDR<0.05; **Figure 3.6E**), which overlapped with the region of *mirrored* inward/outward deformations detected by SNV (**Figure 3.6A**).

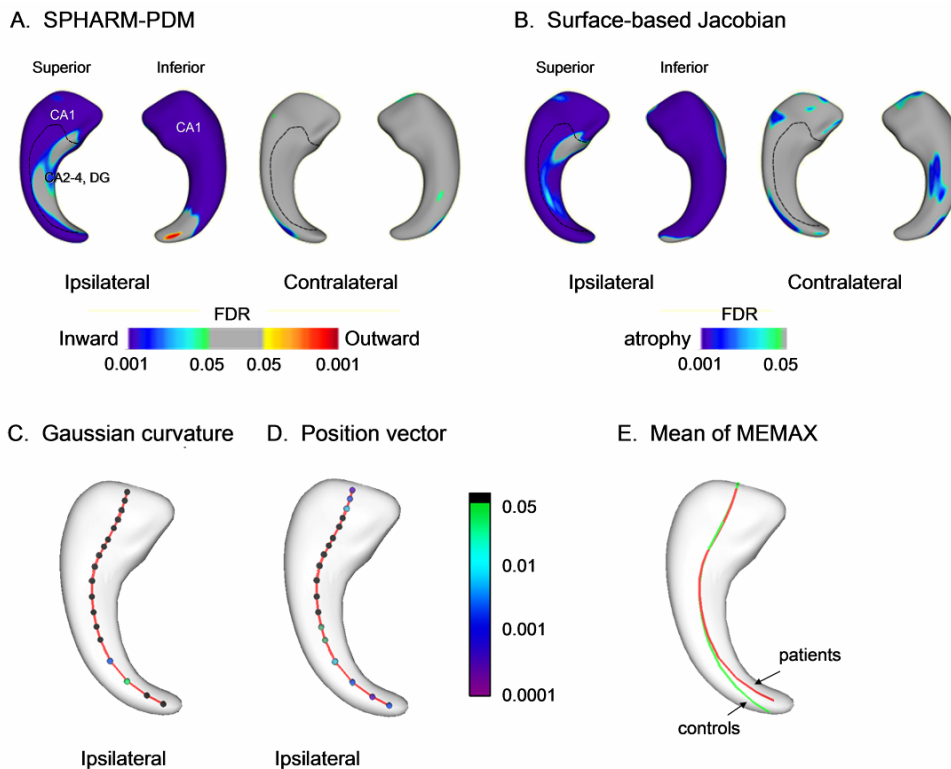


Figure 3.6. Group comparisons between patients with TLE and healthy controls. SPHARM-PDM (**A**), Surface-based Jacobian determinant (**B**), Gaussian curvature (**C**) and position vectors (**D**). The geometric means of MEMAX (**E**) is shown to facilitate the interpretation of C and D. Color-scales show FDR-corrected p-values.

Results in MCD are shown in **Figure 3.7**. While group-wise differences in shape between patients and controls were similar among groups, the extent and severity of abnormalities were more marked in patients with HET. SNV and SJD detected bilateral areas of inward deformation and atrophy distributed along the hippocampus and involving mainly CA1 (FDR<0.05). In addition, SNV detected bilateral outward deformations at the medial portion of hippocampal body corresponding to CA2-CA4 and DG. SJD on the other hand, revealed increased volume overlapping the outward deformation the left hippocampus only (FDR<0.05; **Figure 3.7A-B**).

Curvature analysis of the mean meridian axis (MEMAX) detected flattening (*i.e.*, decrease in curvature) at the level of the left hippocampal body (FCD: 1 sample

point, FDR=0.02; PMG: 2 sample points, FDR<0.001; HET: 3 sample points, FDR<0.05; **Figure 3.7C and E**). In the same location, we also observed medial shifting (FCD: 2 sample points, FDR<0.05; PMG: 3 sample points, FDR<0.001; HET: 6 sample points, FDR<0.0005; **Figure 3.7D**). The same findings were present in the right hippocampus, but did not reach significance.

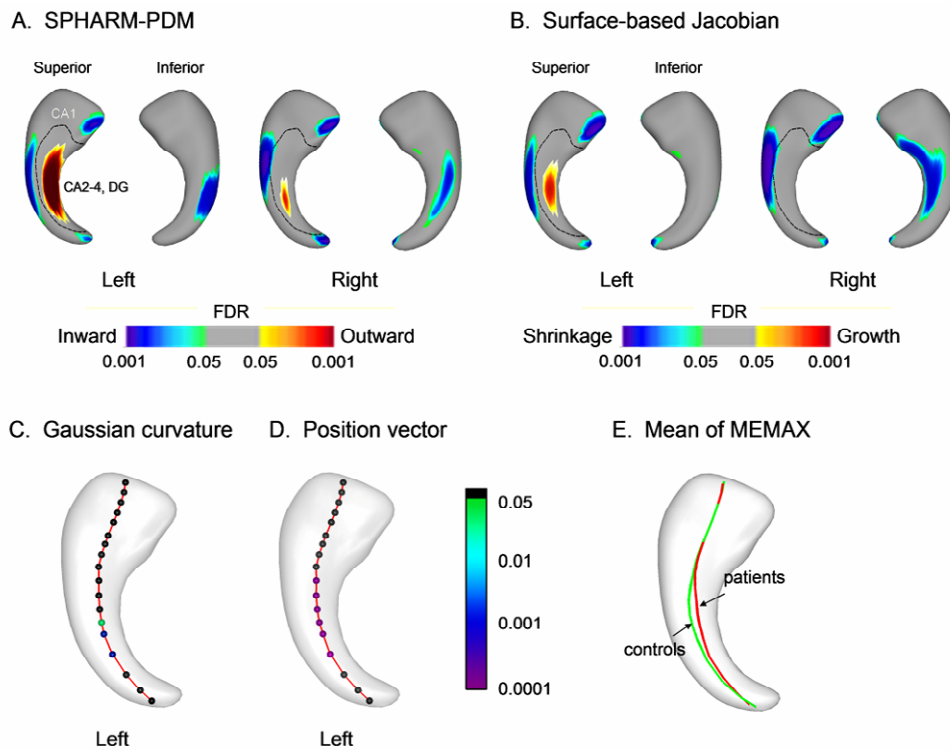


Figure 3.7. Group comparisons between patients with heterotopia and healthy controls. SPHARM-PDM (**A**), Surface-based Jacobian determinant (**B**), Gaussian curvature (**C**) and position vectors (**D**). The geometric means of MEMAX (**E**) is shown to facilitate the interpretation of C and D. Color-scales show FDR-corrected p-values.

Discussion

We presented a surface-based framework that enables to unambiguously disentangle volume from positional changes by quantifying independently these

morphological characteristics through the computation of Jacobian determinants and Gaussian curvatures on the mean meridian axis. We validated successfully our method on synthetic shapes, and studied two cohorts of epileptic patients with TLE and various malformations of cortical development.

Surface-based Jacobian determinant eases the interpretation of hippocampal pathology

Thickness-based measurements computed from medial surface and axis models have been used to measure local hippocampal volume changes (Bouix et al., 2005; Nicolson et al., 2006; Styner et al., 2004). As these approaches produce symmetrical measurements on facing surfaces, they tend to mirror local pathology to the counterpart regions and thus may conceal a biologically plausible interpretation of findings. Indeed, it is well known that histopathology in TLE (Babb and Brown, 1987) and other neurological conditions, such as Alzheimer's disease (Van Hoesen et al., 1990) and schizophrenia (Falkai and Bogerts, 1986; Kobayashi, 2009), is characterized by neuronal damage affecting hippocampal subfields in an uneven fashion. Alternatively, by computing vertex-wise displacement vectors between a given object and a template, SPHARM-PDM allows localizing asymmetrical shape changes (Styner et al., 2004). The signed surface normal components of these vectors signifying inward/outward deformations have been interpreted as local volume changes. In addition to volume changes, this metric captures overlapping positional differences. Indeed, by solving the heat equation using vertex-wise displacement vectors as a boundary condition, our method enabled the detection of *asymmetrical* volume changes independent of positioning, thus complementing SPHARM and providing insights to the interpretation of disease-related morphological processes. While in TLE these abnormalities were detected at the level of the hippocampal tail, in patients with MCD they occurred in the hippocampal body. In both groups, SPHARM-PDM showed mirrored deformations, whereas SJD detected atrophy and MEMAX unveiled medial shifting. In line with

histopathological data showing neuronal loss (Baulac et al., 1998; Raymond et al., 1995), in both patient groups SJD localized hippocampal atrophy corresponding mainly to the CA1 subfield. In addition, SJD showed subtle hypertrophy corresponding to CA2-4 and DG subfields in MCD patients, a finding distinctive of this group and previously reported on conventional MRI resulting from abnormal proliferation and apoptosis (Kuchukhidze et al., 2010; Montenegro et al., 2006).

Mean meridian axis quantifies fine-scale positional changes

In conventional medial axis models, morphological changes related to brain disorders were evaluated using only a small number of sample points (less than 10), aimed mainly at reducing registration errors (Joshi et al., 2002; Styner et al., 2003; Styner et al., 2004). Given the differences in datasets, it is difficult to compare directly the sensitivity of MEMAX model to detect positional changes with previously published skeletonization methods. Taking advantage of the geometric parameters of SPHARM (Styner et al., 2006), MEMAX allowed shape-constrained inter-subject correspondence without requiring a registration step. We found that modulating the number of sample points had an influence on the sensitivity to detect positional changes. Indeed, MEMAX detected the largest positional changes at a fine scale of 18 points.

We designed MEMAX to quantify positional changes of the hippocampus, a cylindrically shaped structure. Achieving this task *via* conventional medial representations would have required additional post-processing steps, such as pruning (Joshi et al., 2002; Styner et al., 2003) to eliminate undesirable secondary branches that would produce irregular skeleton topologies. Moreover, as our central path inherits the geometric parameters of SPHARM, it is applicable to the analysis of a variety of cylindrical structures, such as the amygdala, the caudate, the thalamus and ventricles.

In epilepsy, mesiotemporal malpositioning is thought to be a marker of neurodevelopmental deviance occurring during early phases of gestation (Baulac et al., 1998; Bernasconi et al., 2005b; Kim et al., 2008a; Voets et al., 2011). Disentangling shape from positioning may provide new insights in a variety of other neurological conditions in which these morphological anomalies coexist and a neurodevelopmental hypothesis has been postulated as a potential underlying pathogenic mechanism (Powell, 2010).

3.3 Manuscript 2

Presented at the Spring Hippocampal Research Conference in Verona (May 22-27th 2011)

Manuscript in preparation for *Brain*

Patterns of mesiotemporal subfield pathology in temporal lobe epilepsy: dynamics and relation to surgical outcome

Hosung Kim^{1,2}, Andrea Bernasconi², Boris C Bernhardt², Natalie L Voets²,
Neda Bernasconi²

¹Department of Biomedical Engineering, ²Department of Neurology and Neurosurgery and Brain Imaging Center, McGill University, Montreal Neurological Institute and Hospital, Montreal, Quebec, Canada

Abstract

For the last two decades, MRI volumetry has been the most commonly employed quantitative technique to assess mesiotemporal pathology in drug-resistant temporal lobe epilepsy (TLE). Since this method provides a metric for global volume, its sensitivity to detect subtle diffuse or focal anomalies is limited. Our objective was to investigate in vivo static and dynamic patterns of mesiotemporal subfield pathology in TLE using 3D surface-based shape modeling of high-resolution MRI. In addition, we assessed the yield of this approach to lateralize the seizure focus and predict seizure outcome after surgery. We studied 134 patients comprising 72 with hippocampal atrophy (TLE-HA) and 62 with normal hippocampal volumes (TLE-NV). Patients were compared to 47 age- and sex-matched healthy controls. Cross-sectional analysis revealed ipsilateral hippocampal-CA1 atrophy in both TLE-HA and TLE-NV, although extent and severity were less marked in the latter. Entorhinal cortex atrophy was bilateral in both TLE groups, involving mainly anterior subfields. Patients with TLE-HA displayed ipsilateral amygdalar atrophy located in the laterobasal nuclear group. Conversely, in TLE-NV we found areas of hypertrophy in the ipsilateral amygdalar laterobasal and centromedial nuclei. Additionally, this group presented with bilateral dentate gyrus hypertrophy. Longitudinal analysis in 31 patients mapped progression of atrophy bilaterally, with similar rates across structures and groups. The adverse effect of bi-hemispheric damage was further emphasized by contralateral atrophy predicting unfavorable post-surgical outcome in both TLE groups. While in vivo patterns of structure-specific atrophy are compatible with neuronal loss, hypertrophy suggests aberrant seizure-related plasticity. Timing and interplay between structural pathology and remodeling of neuronal circuitry may lead towards gliosis and neurogenesis, thus masking subtle neuronal loss on standard MRI volumetry in TLE-NV. The ability of 3D surface-based models to unveil anomalies not otherwise detected was further emphasized by a linear discriminant classifier that correctly lateralized the seizures focus in 94% of these patients.

Introduction

In temporal lobe epilepsy (TLE), hippocampal sclerosis is the histopathological term used to describe neuronal loss and astrogliosis in the hippocampus proper, particularly CA1 and CA4, and the dentate gyrus (Babb and Brown, 1987; de Lanerolle et al., 2003; Falconer et al., 1964; Margerison and Corsellis, 1966; Sagar and Oxbury, 1987; Sommer, 1880; Wolf et al., 1993). Although, these features are commonly examined at the level of the mid body of the hippocampus, there is significant variability in their extent and severity (de Lanerolle et al., 2003). In addition, as tissue obtained from surgical resections may be incomplete due to partial resections or fragmented as a result of sub-pial aspiration, a comprehensive evaluation of the mesiotemporal lobe structures is limited (Schramm and Clusmann, 2008). A simultaneous neuropathological assessment of the entire hippocampus, amygdala and entorhinal cortex in the same patients is thus rare. Nevertheless, when available, surgical specimens and *post-mortem* data have shown evidence for extended pathology involving the entorhinal cortex and amygdala (Bruton, 1988; Du et al., 1995; Du et al., 1993; Margerison and Corsellis, 1966; Wolf et al., 1997; Yilmazer-Hanke et al., 2000).

The increasing sophistication of MR image acquisition and processing methods allows whole-brain *in vivo* visualization and quantification of anatomy with exquisite details. For the last two decades, MRI volumetry has been the most commonly employed quantitative technique to assess mesiotemporal lobe pathology. In TLE, hippocampal atrophy is considered a surrogate marker of HS, as the degree of atrophy correlates with the severity of neuronal loss in the *cornu Ammonis*, particularly CA1 (Cascino et al., 1991). The clinical utility of hippocampal volumetry stems from its ability to correctly lateralize the seizure focus in 70-80% of patients (Cascino et al., 1992a; Cendes et al., 1997; Jack et al., 1992), and its value in predicting seizure outcome (Arruda et al., 1996; Berkovic et al., 1995; Cohen-Gadol et al., 2006; Jack et al., 1992; McIntosh et al., 2001; Schramm and Clusmann, 2008). Since this method provides a global estimate of atrophy, its sensitivity to detect subtle diffuse or focal anomalies is

limited. Indeed, in up to 30% of patients with unambiguous electroclinical features of drug-resistant TLE, hippocampal volumetry is unremarkable, despite the presence of mild degrees of sclerosis on histology (Bernasconi et al., 2001; Jackson et al., 1994). On the other hand, volumetry fails to predict a favorable outcome in about 30% of patients, even in the presence of hippocampal atrophy ipsilateral to the seizure focus (Antel et al., 2002b).

To investigate local volume changes, we recently developed and validated a statistical 3D surface-based method relying on spherical harmonics (Styner et al., 2006) and the vertex-wise computation of the Jacobian determinants of the displacement vectors between a given structure and a template (Kim et al., 2008b). Compared to conventional approaches (Csernansky et al., 2000; Hogan et al., 2004; Styner et al., 2006), our technique allows differentiating volume variations from positional changes.

Our objective was to investigate *in vivo* static and dynamic patterns of mesiotemporal subfield pathology in drug-resistant TLE using 3D surface-based shape modeling of high-resolution MRI. We first performed point-wise group comparisons between patients and healthy controls. Secondly, we tracked progression of mesiotemporal atrophy using a longitudinal design. Thirdly, we investigated the relationship between cross-sectional and longitudinal measures of structure-specific pathology and clinical variables, including surgical outcome. Lastly, we assessed the yield of surface-based data to lateralize the seizure focus.

Methods

Subjects

We randomly selected from our database 134 patients referred to our hospital for the investigation of drug-resistant TLE. None of the patients had a mass lesion (malformations of cortical development, tumor, or vascular malformations) or

traumatic brain injury. Demographic and clinical data were obtained through interviews with the patients and their relatives. TLE diagnosis and lateralization of the seizure focus into left TLE (LTLE; n=64) and right TLE (RTLE; n=70) were determined by a comprehensive evaluation including detailed history, neurological examination, review of medical records, video-EEG recordings and MRI evaluation in all patients.

We segmented manually the hippocampus, amygdala and entorhinal cortex on MRI according to our previously described protocol (Bernasconi et al., 2003b). Based on a volumetric assessment that takes into account absolute volume and inter-hemispheric asymmetry, we classified patients into those with hippocampal atrophy (TLE-HA, n=72) and normal hippocampal volume (TLE-NV, n=62). Patients with TLE-HA had younger age at seizure onset ($t=3.7$, $p<0.0005$), longer duration of epilepsy ($t=3.2$, $p<0.005$) and higher incidence of prolonged febrile seizures (Fisher's exact test, $p<0.0005$) than TLE-NV patients.

Within our TLE population, a subset of 31 patients (19 TLE-HA, 12 TLE-NV) refused to undergo surgery at the first evaluation made by our epilepsy team. These patients, however, agreed to have follow-up MRI scans. Sixteen of them eventually followed our recommendation and were subsequently operated.

Ninety patients underwent surgery. Mean follow-up time was 3.4 ± 3.1 years. We determined surgical outcome according to Engel's classification (Engel et al., 1993). Sixty-two (69%) patients had Class I outcome, 7 (8%) class II, 13 (14%) Class III, and 8 (9%) Class IV. Although the proportion of seizure-free patients was slightly higher in TLE-HA (76%) than in TLE-NV (54%), this difference was not significant ($p=0.08$, Fisher's exact test). Following qualitative histopathological analysis (Meencke and Veith, 1991), hippocampal sclerosis was detected in all 66 patients in whom specimens were available. In the remaining 24 patients, hippocampal specimens were either incomplete or unsuitable for examination due to subpial aspiration.

In total, 67 serial MRI scans with 2 to 4 scans per subject were available. All images were acquired on the same scanner. The interval between the first and

last MRI was 2.5 ± 1.4 years (range = 1 to 9.2 years). These scans were examined in the longitudinal analysis. We analyzed the remaining 103 patients together with the first scan of the longitudinal sample in the cross-sectional analysis.

The control group for cross-sectional analysis consisted of 47 age- and sex-matched (23 males; mean age 32 ± 12 years; range: 20 - 66 years) healthy individuals. Demographic and clinical data of all subjects are presented in the **Tables 3.1 and 3.2**.

The Ethics Committee of the Montreal Neurological Institute and Hospital approved the study and written informed consent was obtained from all participants.

Table 3.1. Demographic and clinical data of the cross-sectional cohort.

Group	Male	Age	Onset	FC	Surgery	Engel I
Controls (n=47)	23	32 ± 12 (20-66)	-	-	-	-
LTLE-NV (n=29)	13	37 ± 12 (17-57)	20 ± 13 (2-54)	2	11	5
LTLE-HA (n=35)	17	36 ± 11 (19-52)	14 ± 11 (1-35)	16	28	19
RTLE-NV (n=33)	12	33 ± 10 (17-63)	18 ± 12 (1-49)	1	17	10
RTLE-HA (n=37)	15	36 ± 10 (18-52)	13 ± 10 (1-38)	21	34	28

Age and onset of epilepsy in mean years \pm SD (range); HA/NV: patients with hippocampal atrophy/normal hippocampal volume; Engel I - seizure-free, i.e. Class I postsurgical outcome in Engel's classification

Table 3.2. Demographic and clinical data of the longitudinal cohort.

Group	Age	Males	Duration	HA	Surgery	Engel I
LTLE (n=12)	33 ± 12 (11-50)	8	16 ± 11 (1-42)	7 (58%)	4	2
RTLE (n=19)	33 ± 11 (18-46)	9	17 ± 12 (1-49)	12 (63%)	12	7

Age and duration of epilepsy in years ± SD (range); HA: Number of patients with hippocampal atrophy ipsilateral to the seizure focus (percentage of patients in the group); Engel I: seizure-free, *i.e.* Class-I post-surgical outcome in Engel's classification

MRI acquisition and image processing

MR images were acquired on a 1.5 T Gyroscan (Philips Medical Systems, Eindhoven, Netherlands) using a 3D T1-fast field echo sequence (TR=18 ms; TE=10 ms; NEX=1; flip angle=30°; matrix size=256 × 256; FOV=256; slice thickness=1mm) that provides isotropic 1 mm³ voxels. Each image underwent automated correction for intensity non-uniformity and intensity standardization (Sled et al., 1998).

All baseline images (*i.e.*, first scans of the longitudinal cohort and all scans from the cross-sectional cohort) were linearly registered into a standardized stereotaxic space based on the Talairach atlas (Collins et al., 1994). For the longitudinal analysis, follow-up scans were first linearly registered to the baseline scan in native space, then linearly registered to the stereotaxic space using the transformation parameters of their respective baseline scans, and finally non-linearly registered to the corresponding baseline scan using a piecewise elastic model that performs coarse-to-fine deformations in a hierarchical fashion (Collins et al., 1995). As the segmentation procedure was performed on the baseline scans, inverting the displacement vector fields (obtained in the non-linear

registration step) allowed segmenting automatically mesiotemporal structures on the follow-up scans. The accuracy of the segmentation was verified in all subjects prior to further analysis.

Surface-based mapping of mesiotemporal atrophy

We have developed and validated a method (Kim et al., 2008b) to measure local volume changes based on the computation of Jacobian determinants on surface-based displacement vectors between a given subject and a template surface (Styner et al., 2006). In brief, each set of the manually segmented labels were binarized and underwent a minimal smoothing operation before being converted to surface meshes for which a spherical parameterization (SPHARM) was computed using an area-preserving, distortion-minimizing mapping. Based on a uniform icosahedron-subdivision of the SPHARM, we obtained a point distribution model (PDM), allowing shape-inherent point correspondences across subjects. For each structure (*i.e.*, hippocampus, amygdala and entorhinal cortex) SPHARM-PDM surfaces of each individual were rigidly aligned to a template constructed from the mean surface of controls and patients with respect to the centroid and the longitudinal axis of the 1st order ellipsoid (Gerig et al., 2001). To correct for differences in overall interior head size across subjects, each individual surface were inversely scaled with respect to its intra-cranial volume (Styner et al., 2006). Vertex-wise displacement vectors were then calculated between each individual and the template (Styner et al., 2006). Displacement vectors were diffused within the volume enclosed by the surface using a heat equation, yielding a displacement vector field.

To assess local volume changes cross-sectionally, we calculated Jacobian determinants from these vector fields (Kim et al., 2008b). By linearly interpolating these Jacobian determinants, we obtained a metric of growth ($J > 0$) or shrinkage ($J < 0$) in a unit-size cube defined on each vertex. To localize longitudinal changes in volume, we projected (through a linear interpolation) the displacement vector field obtained between the follow-up and baseline scans to

the baseline SPHARM-PDM surface of each mesiotemporal structure. This procedure guaranteed point-wise correspondence across subjects. The signed surface-normal components of these vectors represent inward/outward deformations that we interpreted as atrophy/hypertrophy.

Statistical analysis

The analysis was done performed using the SurfStat toolbox (<http://www.math.mcgill.ca/keith/surfstat/>) for Matlab (R2007a, The Mathworks, Natick, MA, USA).

- a. *Cross-sectional analysis.* For each structure (*i.e.*, hippocampus, amygdala and entorhinal cortex) we assessed differences in local volume between each TLE group (*i.e.*, LTLE-HA, LTLE-NV, RTLE-HA, RTLE-NV) relative to controls using two-tailed t-tests at each vertex.
- b. *Longitudinal analysis.* To examine the effects of the inter-scan interval, we fitted linear mixed-effects models containing *time from baseline-scan* and *subject* intercept as effects on mesiotemporal structures whole-volumes / vertex-wise volumes, and tested for a negative effect of *time from baseline-scan*. To assess possible differences in rates of progression between TLE-HA and TLE-NV, we tested for interaction of *group* \times *scan interval*.
- c. *Clinical correlational analysis.* We used linear models to assess the relation between vertex-wise volume changes and febrile/generalized tonic-clonic seizures (cross-sectional cohort) and post-surgical outcome (cross-sectional and longitudinal cohorts). To increase statistical power, data from LTLE and RTLE were pooled and analyzed relative to the side of seizure focus (*i.e.*, ipsilateral and contralateral).
- d. *Seizure focus lateralization.* For each mesiotemporal structure, surface-based data of LTLE-NV and RTLE-NV were pooled relative to the side of the seizure focus. We calculated an asymmetry index (ipsilateral-contralateral) /

(ipsilateral+contralateral) at each vertex and assessed its significance using one-tailed paired t-tests (*i.e.*, ipsilateral volume is smaller than contralateral). To be unbiased by the choice of a statistical threshold, the analysis was iteratively done for p-values ranging from $\alpha = 0.05$ to 1. At each iteration asymmetry indices of all vertices with a p-value less than α were averaged. Mean asymmetry values for each patient were then used in a linear discriminant classifier to lateralize the focus. Cross-validation of the classification was performed using a leave-one-out approach. This procedure, by which an individual patient is lateralized using only the data of all other subjects, allows an unbiased assessment of lateralization performance for previously unseen TLE cases. We applied the same analysis to the standard volumetric data.

- e. *Correction for multiple comparisons.* In all vertex-wise surface analyses, significances were thresholded using the false discovery rate procedure (Benjamini and Hochberg, 1995), with $FDR < 0.05$. In the volumetric analysis, Bonferroni-adjustment (based on 3 structures \times 2 hemispheres) was applied to control the family-wise error rate.
- f. *Localization of findings.* According to histological parcellations, we schematically outlined hippocampal (Duvernoy, 2005), entorhinal (Insausti et al., 1995) subfields and amygdalar (Amunts et al., 2005) nuclear groups on each structure's surface template.

Results

Cross-sectional cohort: Group analysis

Table 3.3 displays the results of group comparisons of the conventional volumetric analysis.

Table 3.3. Volumetry of mesiotemporal structures in TLE.

Group	Hippocampus		Entorhinal cortex		Amygdala	
	Left	Right	Left	Right	Left	Right
LTLE-HA (n=35)	-4.0 ± 1.4	-0.3 ± 1.4	-2.5 ± 1.0	-0.6 ± 1.1	-0.8 ± 1.2	-0.3 ± 1.1
RTLE-HA (n=37)	-0.2 ± 1.3	-3.4 ± 1.2	-0.7 ± 1.1	-1.7 ± 1.0	0.1 ± 1.2	-0.8 ± 1.4
LTLE-NV (n=29)	0.3 ± 1.7	0.1 ± 1.1	-1.6 ± 0.9	-0.7 ± 1.1	0.6 ± 1.5	0.1 ± 1.4
RTLE-NV (n=33)	0.0 ± 1.1	0.1 ± 1.0	-1.0 ± 1.5	-1.3 ± 1.2	0.4 ± 1.6	0.8 ± 1.5

Volume measurements standardized relative healthy controls using a z-score transformation. Group-wise significances (in bold) thresholded at $p < 0.05$ after Bonferroni correction.

Results of vertex-wise group comparisons between TLE-NV and controls are shown in **Figure 3.8**. Patterns of atrophy in the mesiotemporal lobe structures were similar in LTLE-HA and RTLE-HA. In the hippocampus, ipsilateral atrophy was diffuse and distributed along the rostro-caudal extent ($-1.3 \pm 0.4 \text{ mm}^3$; **Figure 3.8A**) in vertices corresponding mainly to the CA1 subfield. Atrophy in regions corresponding to the CA2, CA3 and the dentate gyrus was considerably less marked ($-0.3 \pm 0.1 \text{ mm}^3$). Contralateral to the focus, we found small areas of mild CA1 atrophy ($-0.5 \pm 0.2 \text{ mm}^3$). In the entorhinal cortex, atrophy was observed bilaterally in its superficial layers; however, changes were more extensive and marked ipsilateral to the seizure focus (ipsilateral: $-0.9 \pm 0.12 \text{ mm}^3$,

contralateral: $-0.5 \pm 0.08 \text{ mm}^3$; **Figure 3.8B**). Amygdalar atrophy was located in the ipsilateral laterobasal nuclear group ($-0.9 \pm 0.2 \text{ mm}^3$; **Figure 3.8C**).

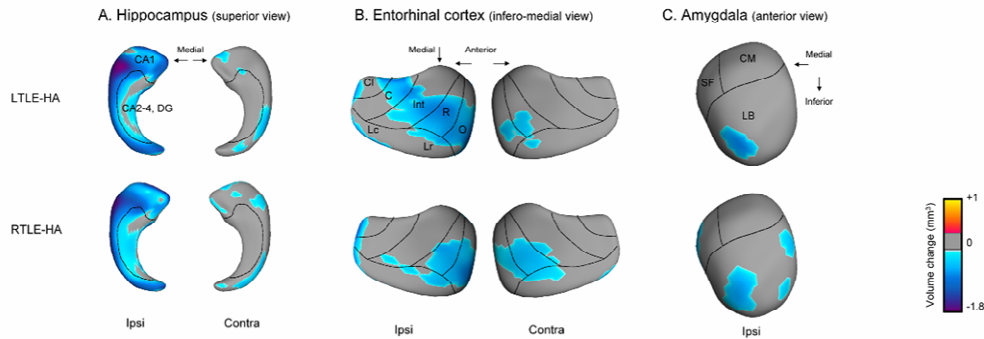


Figure 3.8. Cross-sectional vertex-wise analysis in TLE with hippocampal atrophy.

Regions of volume increase/decrease (in mm^3) relative to healthy controls are shown for the hippocampus (**A** - superior view), the entorhinal cortex (**B** - inferomedial view) and the amygdala (**C** - anterior view). Significances are thresholded at $FDR < 0.05$. For each structure, schematic boundaries of subdivisions are outlined on the template.

Abbreviations: Hippocampus: CA: cornu ammonis; DG: dentate gyrus. Entorhinal cortex: C: caudal; Cl: caudal limit; Int: intermediate; Lr: lateral rostral; Lc: lateral caudal; O: olfactory; R: rostral. Amygdala: CM: centromedial nuclear group; LB: laterobasal nuclear group including lateral, basolateral, basomedial, and accessory basal nuclei; SF: superficial nuclear group including cortical nuclei; Ipsi/Contra: ipsilateral/contralateral to seizure focus.

Results of vertex-wise group comparisons between TLE-NV and controls are shown in **Figure 3.9**. Patterns of atrophy were comparable in LTLE-NV and RTLE-NV. In the hippocampus, a mild degree of atrophy was observed in CA1 subfield ipsilateral to the focus ($-0.4 \pm 0.15 \text{ mm}^3$; **Figure 3.9A**). On the other hand, small areas of hypertrophy were observed bilaterally in the dentate gyrus ($+0.5 \pm 0.15 \text{ mm}^3$). Entorhinal cortex atrophy was present bilaterally in the anterior subdivisions (ipsilateral: $-0.7 \pm 0.12 \text{ mm}^3$, contralateral: $-0.4 \pm 0.1 \text{ mm}^3$, **Figure 3.9B**). We did not amygdalar atrophy. Instead, we found focal areas of hypertrophy in the laterobasal and centromedial nuclear groups ($+0.6 \pm 0.18 \text{ mm}^3$, **Figure 3.9C**).

We did not find any relation between febrile or generalized tonic-clonic seizures and local volume changes.

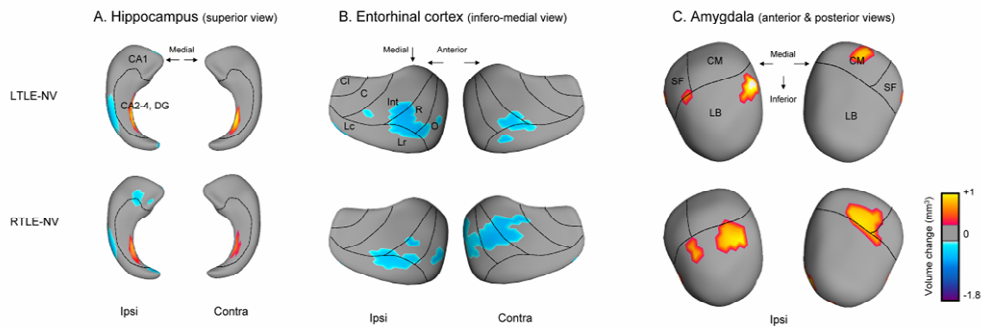


Figure 3.9. Cross-sectional vertex-wise analysis in TLE with normal hippocampal volume.

Regions of volume increase/decrease (in mm^3) relative to healthy controls are shown for the hippocampus (**A** - superior view), the entorhinal cortex (**B** - inferomedial view) and the amygdala (**C** - anterior and posterior views). Significances are thresholded at $FDR < 0.05$. For each structure, schematic boundaries of subdivisions are outlined on the template. See Figure 3.8 for abbreviations.

Longitudinal cohort: Effects of inter-scan interval

Volumetric analysis showed progressive atrophy in a bilateral and symmetric fashion in all three mesiotemporal structures, with an annual rate ranging from 4.9 to $13.1 \text{ mm}^3/\text{year}$ ($t > 2.8$, $FDR < 0.05$; **Figure 3.10**). Negative effects were highly similar in TLE-HA and TLE-NV; indeed, interaction analysis did not reveal any difference between the regression slopes ($t < 2.2$, $FDR < 0.2$).

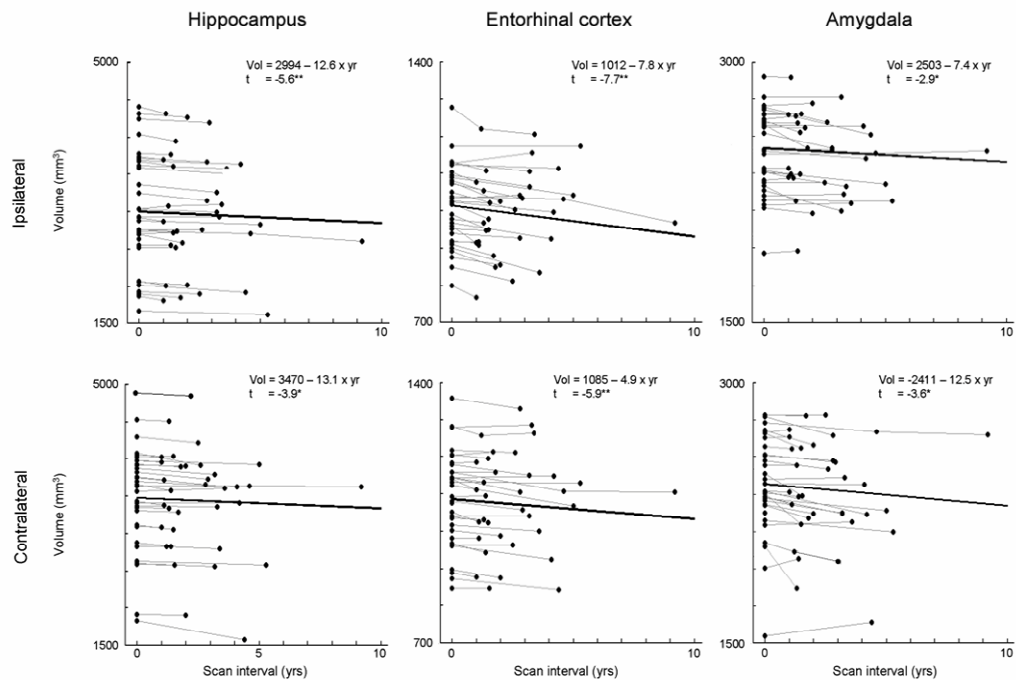


Figure 3.10. Longitudinal analysis of standard volumetry.

Plots show the effect of inter-scan interval on changes in mean hippocampal, entorhinal cortex and amygdalar volume. Gray lines connect the MR scans, indicated as black dots; the mixed-effects model is plotted as a solid black line (* $p < 0.05$; ** $p < 0.0005$).

Vertex-wise analysis localized bilateral symmetric areas of progressive atrophy in hippocampal CA1 (ipsilateral: -0.027 ± 0.006 mm/year; contralateral: -0.029 ± 0.013 mm/year; **Figure 3.11A**), entorhinal lateral rostral and caudal subfields (ipsilateral: -0.035 ± 0.012 mm/year, contralateral -0.021 ± 0.007 mm/year; **Figure 3.11B**), and the amygdalar laterobasal nuclear group (ipsilateral: -0.024 ± 0.007 mm/year, contralateral -0.029 ± 0.008 mm/year; **Figure 3.11C**). Comparing the rate of atrophy between the two TLE groups revealed a more marked ipsilateral progression in the hippocampus and amygdala of TLE-HA patients, whereas entorhinal atrophy progressed at a similar rate. There was no difference between the regression slopes in the contralateral hemisphere.

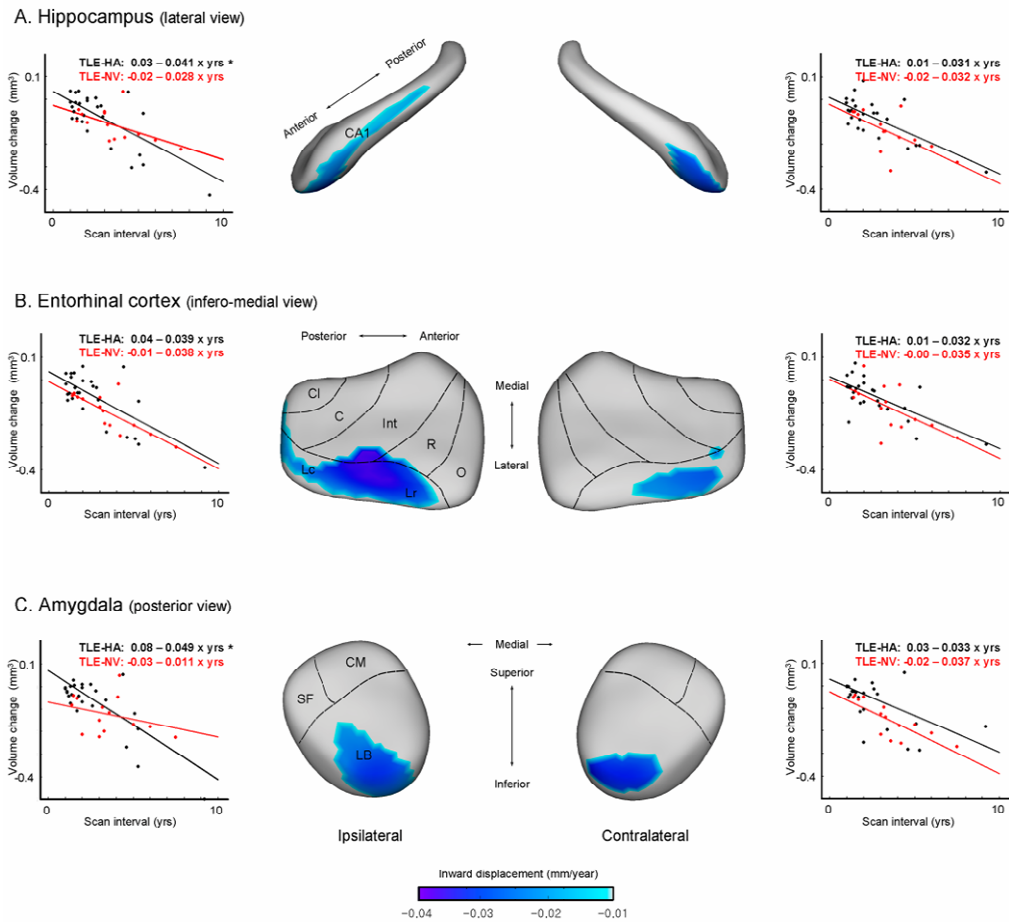


Figure 3.11. Longitudinal vertex-wise analysis.

Regions of significant atrophy (in mm/year) are mapped on the hippocampus (**A**), entorhinal cortex (**B**) and amygdala (**C**). For each cluster, plots of mixed-effects models are shown; the model for TLE-HA is plotted as a solid black line, the model for TLE-NV as a solid red line. Significances are thresholded at $FDR < 0.05$. The * indicates faster progression of atrophy in TLE-HA relative to TLE-NV. For each structure, schematic boundaries of subdivisions are outlined on the template. See **Figure 3.8** for abbreviations.

Predictors of outcome

In both TLE groups, patients who had residual seizures after surgery displayed areas of volume loss in the contralateral hippocampal CA1 and the laterobasal amygdalar nucleus ($t > 2.9$, $FDR < 0.03$; **Figure 3.12A**). On the other hand, we found a more marked pre-operative progression of atrophy in lateral subfields of the entorhinal cortex bilaterally in patients with residual seizures compared to those who became seizure-free (-0.04 mm/year vs. <-0.01 mm/year; $t > 2.8$; $FDR < 0.05$, **Figure 3.12B**).

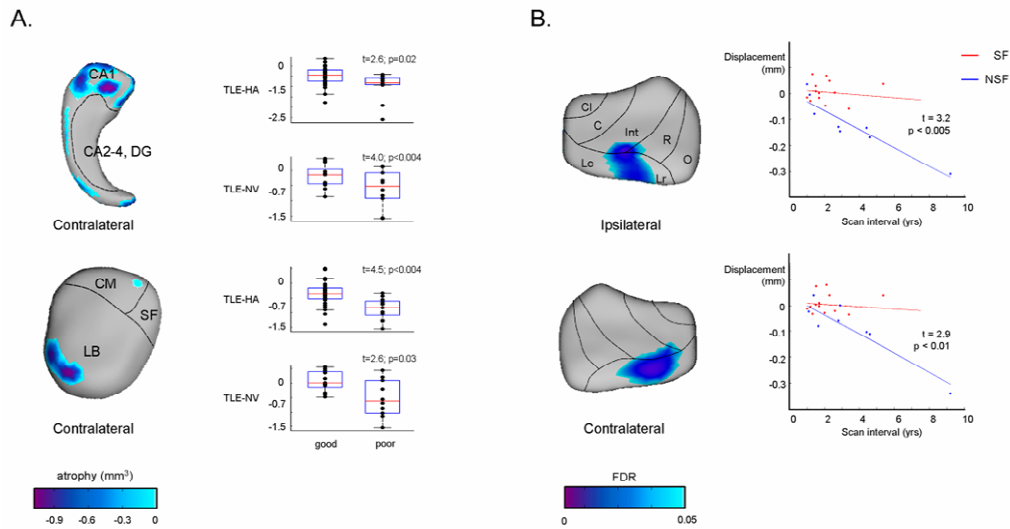


Figure 3.12. Predictors of post-surgical outcome.

A) Cross-sectional vertex-wise maps of contralateral hippocampal and amygdalar atrophy in patients with residual seizures (Engel Ib -IV, poor) compared to seizure free patients (Engel Ia, good). Significances are thresholded at $FDR < 0.05$. Box-and-whiskers plots display group-wise differences within clusters of atrophy. **B)** Longitudinal vertex-wise maps displaying bilateral entorhinal atrophy in patients with residual seizures. The graphs show the interaction between scan-interval and surgical outcome within clusters of bilateral accelerated progression in non seizure free patients (NSF - in blue) compared to those who became seizure free after surgery (SF - in red).

Lateralization of the seizure focus in TLE-NV

Results are shown in **Figure 3.13**. Linear discriminant function analysis on whole-volume asymmetry indices correctly lateralized the seizure focus in 52% (32/62) of patients using the hippocampus, 71% (44/62) using the entorhinal cortex, and 63% (39/62) using the amygdala. When all three structures were combined, 73% (45/62) of patients were correctly lateralized.

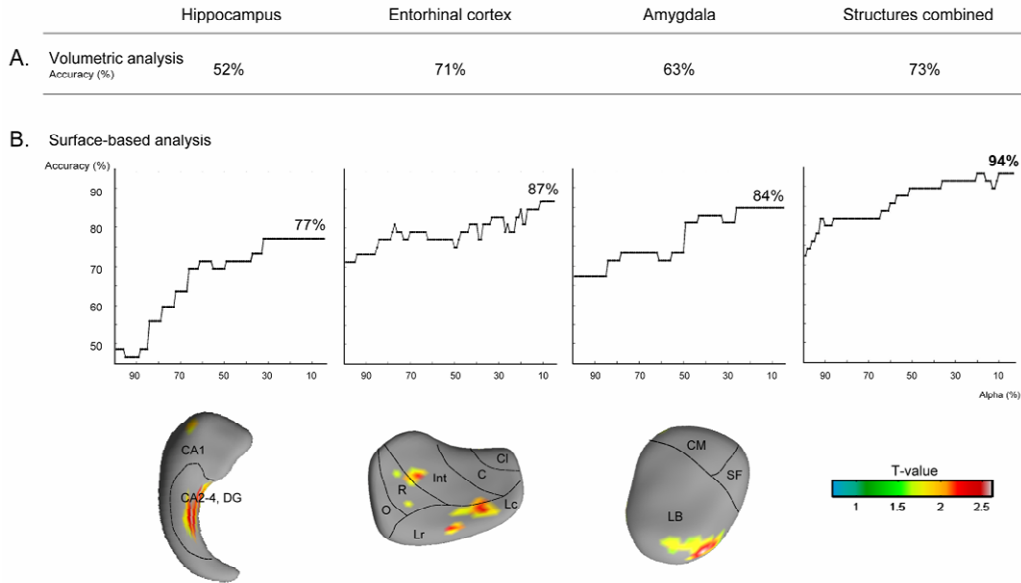


Figure 3.13. Seizure focus lateralization in TLE patients with normal hippocampal volume.

Lateralization accuracy of a linear discriminant classifier based on the separate and combined analysis of the three mesiotemporal structures using: **A)** standard volumetry; **B)** surface-based analysis. For each structure, regions contributing to the optimal vertex-wise lateralization performance (at $\alpha=10\%$) are shown.

Repeating this analysis using surface-based vertex-wise asymmetry indices correctly lateralized the focus in 77% (48/62) of patients using the hippocampus, in 87% (54/62) using the entorhinal cortex, and 84% (52/62) using the amygdala. Combined analysis of the three structures increased the lateralization rate to 94% (58/62). These findings were robust against variations of the percentile of t-

values (optimal classification at $\alpha = 0.05-0.13$). Vertices that yielded optimal lateralization at α of 0.05 were localized in CA2-4 subfields and the dentate gyrus for the hippocampus, in the laterobasal nucleus of the amygdala and caudal subdivisions of the entorhinal cortex.

Discussion

Using 3D surface mapping of high-resolution MRI, we statistically localized mesiotemporal subfield pathology across the spectrum of drug-resistant TLE. To the best of our knowledge, a comprehensive investigation using both cross-sectional and longitudinal designs to assess structure-specific damage, its progression and clinical relevance has not been previously performed.

Advanced surface-based shape models, including deformation-based mapping and spherical harmonics combined with point distribution models, have allowed localization of morphological changes that may not be readily visible (Styner et al., 2006), and identified hippocampal shape abnormalities in TLE (Hogan et al., 2004). The displacement metric provided by these approaches, however, does not allow differentiating volume from positional differences. Thus, a biologically meaningful interpretation of findings may be difficult, particularly when both morphological characteristics co-exist. Moreover, inter-subject shape variability may reduce statistical sensitivity to detect subtle pathology. Our method overcomes these limitations by quantifying volume changes only through the computation of surface-based Jacobian determinants of the displacement vectors (Kim et al., 2008b).

Compared to standard volumetry, our technique showed increased sensitivity by unveiling subtle ipsilateral hippocampal atrophy in TLE-NV, ipsilateral amygdalar and contralateral hippocampal and entorhinal pathology in both TLE groups. Longitudinal analysis mapped mesiotemporal atrophy that spatially overlapped with cross-sectional results, the progression rates being comparable among groups. Contralateral CA1 and amygdalar laterobasal atrophy, and bilateral

progressive entorhinal volume loss were predictive of unfavorable post-surgical outcome. Lastly, a combined surface-based analysis of all three mesiotemporal lobe structures correctly lateralized the seizure focus in 94% of patients with TLE-NV, as opposed to 73% using standard volumetry.

In vivo mapping of mesiotemporal sclerosis

The histopathological descriptions of hippocampal sclerosis stem from macroscopic examination of autopsy brain specimens (Margerison and Corsellis, 1966; Meencke and Veith, 1991), and have been refined through microscopic analysis (Bruton, 1988) and neuronal counts (Babb et al., 1984; Blümcke et al., 2007; de Lanerolle et al., 2003; Thom et al., 2002a). In a semi-quantitative study of a large number of hippocampal specimens obtained at surgery, unbiased clustering technique identified severe CA1 neuronal loss in the vast majority of cases, whereas the other subfields were only moderately affected (Blümcke et al., 2007). The extent of pathology seems to be fairly uniform along the longitudinal hippocampal axis (Thom et al., 2010; Thom et al., 2002a). Noteworthy, because of the inadequacy of the surgical specimen in many cases and difficulties in evaluating the complex anatomical organization of the amygdala and the entorhinal cortex, a combined analysis of these mesiotemporal structures has been rarely performed. Nevertheless, a study in patients with hippocampal sclerosis revealed prominent neuronal loss and gliosis in the amygdalar basolateral nucleus and across all layers of the entorhinal cortex (Yilmazer-Hanke et al., 2000).

Our findings of atrophy predominating in CA1, in the laterobasal amygdala and rostral the entorhinal cortex are in agreement with the above histopathological reports, emphasizing the ability of post-processing of anatomical MRI to unveil anomalies not otherwise detected on visual evaluation or volumetric analysis.

Similar to TLE-HA, patients with TLE-NV presented with ipsilateral CA1 atrophy, that was, however, less marked and widespread. Our results are consistent with the few reports on histopathology of TLE-NV showing a lesser degree of neuronal loss in CA1 compared to TLE-HA (Bernasconi et al., 2001; Cohen-Gadol et al., 2005; Jackson et al., 1994). On the other hand, our intriguing observation of concomitant dentate gyrus and amygdalar hypertrophy in TLE-NV is suggestive of aberrant structural plasticity. Indeed, while virtually all healthy mammals, including humans, exhibit neurogenesis throughout life in regions such as the dentate gyrus and the amygdala (Bernier et al., 2002), seizure-related altered dentate neurogenesis has emerged as a hallmark of TLE. This phenomenon has been reported in both animal models (see for review - (Parent, 2008; Scharfman and McCloskey, 2009) and post-surgical specimens of epileptic children (Mathern et al., 2002; Siebzehnrubl and Blumcke, 2008). Likewise, the rate of amygdalar neurogenesis might be altered by various conditions, such as stressful events and epileptic activity (Gould and Tanapat, 1999). Interestingly, a recent study showed that the proliferative capacity of cells derived from the dentate subgranular zone of adult TLE patients decreases with longer disease duration, and is almost absent in mesiotemporal sclerosis (Paradisi et al., 2010). In keeping with this observation, we did not find group-wise hippocampal hypertrophy in patients with TLE-HA, who have more severe hippocampal atrophy and longer duration of epilepsy than those with TLE-NV.

In experimental models of TLE, astrocytes and microglia cells in the hippocampus undergo hypertrophy following seizures (for review, see (Foresti et al., 2011)). Astrogliosis has been hypothesized to play a role in hyperexcitability and the occurrence of spontaneous seizures by altering synaptic and neuronal activity (Binder and Steinhauser, 2006). Gliosis in regions of neuronal loss is a well-recognized pathological feature of mesiotemporal sclerosis. While a lesser degree of neuronal loss in CA1 relative to TLE-HA is distinctive of TLE-NV, glial counts in CA2 and CA4 have been shown to be elevated to the same extent in both groups (King et al., 1996). Glial alterations, in addition, may participate to aberrant neurogenic changes (Shapiro et al., 2005) and even precede neuronal

damage (Kang et al., 2006). Considering data from animal models, human histopathology and our current MRI findings, it is tempting to speculate that timing and interplay between structural pathology and remodeling of neuronal circuitry may lead towards gliosis and neurogenesis, thus masking subtle neuronal loss in TLE-NV and resulting in normal standard MRI volumetry.

Mesiotemporal disease progression

There is compelling evidence that drug-resistant TLE is a progressive neurologic disorder that requires early and effective treatment (Bernhardt et al., 2009; Bonilha et al., 2006; Sutula, 2004; Tasch et al., 1999). Cross-sectional analyses have shown positive correlation between longer disease duration and atrophy (Bernasconi et al., 2005b; Theodore et al., 1999). Since patients with intractable seizures rarely refuse surgery, only one study has so far examined hippocampal volumes longitudinally (Fuerst et al., 2003) and provided evidence for progression of atrophy ipsilateral to the focus. Our longitudinal data, on the other hand, revealed bilateral and symmetric progressive atrophy not only in the hippocampus, but also the entorhinal cortex and amygdala over a mean interval of 2.5 years. The striking similarity in the dynamics of mesiotemporal atrophy between TLE-HA and TLE-NV parallels our recent observation in the neocortex, supporting the concept that these two entities are part of the same spectrum (Bernhardt et al., 2010). Increased sensitivity to bilateral atrophy is likely due to our methodological approach. Contrary to the above-cited longitudinal analysis that used paired t-tests, we opted for linear mixed-model regression, as it permits the inclusion of multiple measurements per subject, and irregular intervals between measurements, thereby increasing statistical power while controlling for within-individual variation. Further sensitivity may derive from our fully automated assessment of volumetric changes on repeated scans as opposed to manual segmentation of repeated scans.

Clinical implications of bilateral mesiotemporal atrophy

Unilateral hippocampal atrophy on MRI is generally considered a reliable predictor of favorable post-surgical outcome (Arruda et al., 1996; Berkovic et al., 1995; Cohen-Gadol et al., 2006; Jack et al., 1992; McIntosh et al., 2001; Schramm and Clusmann, 2008). However, residual seizures in about 30% of TLE patients (Schramm and Clusmann, 2008) are an incentive to search for more refined MRI markers. Our results show that atrophy in the contralateral hippocampal CA1, laterobasal nucleus of the amygdala, and progressive bilateral damage in the lateral entorhinal cortex predict unfavorable outcome. The adverse effect of bi-hemispheric damage is further supported by our recent findings showing bilateral neocortical atrophy (Bernhardt et al., 2009) and increased folding complexity (Voets et al., 2011) in patients with residual seizures after surgery.

Bilateral static and dynamic mesiotemporal damage may impact significantly cognition in TLE. It has been suggested that verbal and visuo-spatial functions have bi-hemispheric representations, likely as a natural evolution from symmetrical functional networks in lower primates (Milner, 1971). Damaged inter-hemispheric communication between mesiotemporal structures (and likely more widespread (Voets et al., 2009)) may impair memory function bilaterally, independent of stimulus type (Dobbins et al., 1998). This notion is supported by memory impairments following commissurotomy, not predicted by classical hemispheric specialization models (Dobbins et al., 1998). Our findings of progressive atrophy affecting contralateral mesiotemporal structures could thus conceivably contribute to the lack of consistent material-specific deficits often observed in TLE patients irrespective of the side of the seizure focus, even though clinical and task variables (such as nature and complexity of test stimuli) may play additional roles (Bell and Giovagnoli, 2007; Dobbins et al., 1998).

3.4 Manuscript 3

Published in *Neurology* 2008. 70(22 Pt2): 2159-2165

Basal temporal sulcal morphology in healthy controls and patients with temporal lobe epilepsy

Hosung Kim^{1 2}, Neda Bernasconi², Boris C. Bernhardt², Olivier
Colliot³, Andrea Bernasconi²

¹Department of Biomedical Engineering, ²Department of Neurology and
Neurosurgery and Brain Imaging Center, McGill University, Montreal
Neurological Institute and Hospital, Montreal, Quebec, Canada and ³Cognitive
Neuroscience and Brain Imaging Laboratory, CNRS, UPR 640, Université Paris 6,
Hôpital de la Salpêtrière, Paris, France

Abstract

The purpose of this study was to categorize morphological sulcal patterns of the basal temporal lobe in patients with temporal lobe epilepsy (TLE). We studied 51 healthy controls and 69 patients with TLE (37 left, 32 right TLE), including 35 with hippocampal atrophy and 34 with normal hippocampal volumes. Brain sulci were identified and labeled automatically on MRI using an automated algorithm based on a congregation of neural networks. 3D sulcal models mapped on the cortical surface were inspected visually. We used four sulcal patterns classes proposed by Ono (Ono et al., 1990) to describe the sulcal arrangement in the inferior surface of the temporal lobe in each subject: Type 1, i.e. single-branch, unbroken collateral sulcus (CS) connected with the rhinal sulcus (RS) anteriorly; Type 2, i.e. CS connected with the occipitotemporal sulcus (OTS), but separated from the RS; Type 3, i.e. CS separated from the OTS and RS, which are connected; and Type 4, i.e., CS, OTS and RS separated. Compared to controls, we found an increased frequency of Type 1 CS in TLE patients, both in the left (NC: 47%, TLE: 77%, $p = 0.004$) and the right hemispheres (NC: 41%, TLE: 72%, $p = 0.002$). On the other hand, we found a decreased frequency of Type 2 CS in TLE patients, both in the left (NC: 31%, TLE: 4%, $p = 0.00002$) and the right hemisphere (NC: 35%, TLE: 4%, $p < 0.00001$). We found no association between the sulcal patterns and the side of seizure focus, febrile seizures and hippocampal volume. A single-branch, unbroken CS is the predominant sulcal pattern found in TLE. This “simplified” arrangement may be a marker of altered corticogenesis and predispose the temporal lobe to be vulnerable to injuries during early gestation.

Introduction

The ventral and medial surfaces of the temporal lobe are organized into strips by two prominent rostro-caudally oriented sulci. The more lateral of the two is the occipitotemporal sulcus (OTS), which is often broken forming small, transverse gyri. The more medial is the collateral sulcus (CS) and marks the border between the parahippocampal gyrus and the occipitotemporal (i.e., fusiform) gyrus. The CS may be continuous rostrally with the rhinal sulcus (RS), although there is individual variability in the arrangement and depth of these sulci (Insausti and Amaral, 2004; Van Hoesen, 2002). The parahippocampal region is anatomically and functionally deeply related to the hippocampus (for review see (Witter et al., 2000)).

The vast majority of morphological MRI studies of the brain have been focused on assessing gray- and white matter volumes. Less attention has been paid to sulcal morphology. Studying the normal sulcal anatomy of the inferior surface of the temporal lobe in *postmortem* specimens of 25 non-diseased brains, Ono et al. (Ono et al., 1990) described four main patterns of sulcal arrangement based on the relationship between the CS and neighboring sulci, i.e. the RS and OTS. The sulcal patterns of the inferior temporal lobe have been rarely studied *in vivo* in healthy controls using MRI (Insausti et al., 1998; Pruessner et al., 2002). Morphological studies of sulcal patterns abnormalities in neurological disorders have shown reduced cortical folding in the temporal lobe relative to healthy subjects in schizophrenia (Jou et al., 2005; Kikinis et al., 1994; Kulynych et al., 1997; Sallet et al., 2003) and velo-cardio-facial syndrome (Schaer et al., 2006), lateral shifting of the CS in autism (Levitt et al., 2003) and reduction of CS depth in Williams syndrome, a rare genetic disorder (Kippenhan et al., 2005). In epilepsy, sulcal abnormalities have not been systematically studied. They have been occasionally reported in relation to malformations of cortical development, either in the presence of an obvious lesion or suggested to be a possible marker of subtle cortical dysgenesis (Bronen et al., 2000; Muntaner et al., 1997; Rakic,

1988). One study (Novak et al., 2002) categorized the CS in TLE patients into three types according to the relationship between the CS and the RS. In this study, which did not include healthy control subjects, no predominant sulcal pattern was found. Atypical morphologies of the CS, such as verticalization and increased depth, have been described in relation to shape and positioning abnormalities of the hippocampal formation in TLE (Barsi et al., 2000a; Baulac et al., 1998; Bernasconi et al., 2005a). These observations were based on the evaluation of CS characteristics on two-dimensional (2D) MRI in few coronal sections along the rostro-caudal extent of temporal lobe.

Although MRI offers an opportunity to complement labor-intensive post-mortem studies of gyrification, the complexity of the brain's convolution makes the visual identification of sulcal-gyral abnormalities difficult on orthogonal planes obtained in conventional MRI. Furthermore, extensive manual sulcal segmentation on MRI is prohibitive. To bypass the disadvantages, computer-based sulcal identification techniques have been implemented (Blanton et al., 2001; Le Goualher et al., 1999; Levitt et al., 2003; Thompson et al., 1996). In particular the method developed by Mangin (Mangin et al., 1995) and Riviere (Riviere et al., 2002) allows not only the inspection of sulcal and gyral patterns on brain surfaces, but also the automatic extraction, identification, and labeling of brain sulci. This method, which has proven to be precise and robust, greatly facilitates population-based studies of sulcal variability and has been successfully applied to evaluate temporal lobe sulcal patterns in schizophrenia (Bartrez-Faz et al., 2002) and Turner syndrome (Molko et al., 2003).

Our purpose was to categorize the CS morphological patterns in patients with TLE and healthy controls using an automated sulcal extraction method allowing the description of sulcal variability on brain surfaces on MRI.

Methods

Subjects

We randomly selected 69 patients with medically intractable TLE (33 males; mean age = 32 ± 9 years, range = 16-49) from our database. The TLE population was composed of 35 patients with unilateral hippocampal atrophy and 34 with normal hippocampal volumes as determined by volumetric MRI (see below). The control group consisted of 51 sex- and age-matched healthy subjects (25 males; mean age = 32 ± 11 years, range = 20-56).

Demographic and clinical data were obtained through interviews with the patients and their relatives, and by reviewing hospital charts. Seizure type and the site of seizure onset were determined by a comprehensive evaluation including seizure history and semiology, video-EEG telemetry, and neuropsychological evaluation in all patients. In TLE, the seizure focus was left-sided in 37 patients and right-sided in 32. The Ethics Committee of the Montreal Neurological Institute and Hospital approved the study and written informed consent was obtained from all participants.

MRI acquisition and image pre-processing

In all subjects, MR images were acquired on a 1.5 T Gyroscan (Philips Medical System, Eindhoven, Netherlands) using a 3D T1-fast field echo sequence (TR=18, TE=10, 1 acquisition average pulse sequence, flip angle= 30° , matrix size=256x256, FOV=256, slice thickness=1mm). This high-resolution T1-weighted 3D gradient-echo sequence provides exquisite anatomic details with an isotropic voxel size of 1x1x1 mm and features high signal-to-noise and contrast-to-noise (Antel et al., 2002a).

MR images were registered into a standardized stereotaxic coordinate space based on the Talairach atlas (Talairach and Tournoux, 1988) to adjust for

differences in total brain volume and brain orientation and to facilitate the identification of boundaries by minimizing variability in slice orientation (Collins *et al.*, 1994). This procedure uses an automatic, multi-scale feature-matching algorithm (Collins *et al.*, 1994) that performs a 9-parameter linear transformation to match each brain to a template brain. The reference image used for the linear registration and resampling was the ICBM 152 T1-weighted target, a voxel-by-voxel average of the 152 normal subjects previously registered in the Talairach-like stereotaxic space (Mazziotta *et al.*, 1995). Each image underwent automated correction for intensity non-uniformity and intensity standardization (Sled *et al.*, 1998). This correction produces consistent relative gray matter (GM), WM and cerebrospinal fluid (CSF) intensities.

Generation of brain surfaces and sulcal models

Images were processed using BrainVISA, a brain image analysis software which allows to reconstruct the surfaces corresponding to GM-WM and GM-CSF interfaces and to extract the brain sulci (Mangin *et al.*, 1995; Riviere *et al.*, 2002). To compute accurate cortical surfaces and brain sulcal folds, image processing includes the following steps: 1) histogram analysis and brain segmentation; 2) brain masking and dividing of brain regions into hemispheres, cerebellum, and brain stem; 3) classification of white matter, gray matter and CSF in each hemisphere; 4) skeletonization of the GM/CSF union using a homotopic erosion; 5) reconstruction of the surfaces corresponding to the GM-WM interface and GM-CSF interface using the classification maps generated in step 3); 6) extraction of the sulcal folds: this procedure segments the skeletonized GM/CSF interface into simple surfaces; 7) sulcal graph construction: the spatial and structural relationships of the sulcal ribbons are depicted as a graph model including the information essential to the sulcal recognition process.

Labeling sulci based on semi-automated sulcal recognition

After extraction, sulci are automatically labeled using the method proposed by Riviere et al. (Riviere et al., 2002). In brief, this technique relies on a congregation of neural networks trained on a manually identified database of sulci. Recognition of structures is achieved by maximizing similarity of sulci features and sulci relations. A trained observer (N.B.) inspected all images to check for any possible identification errors in the CS, RS and OTS to perform manual correction when needed.

Examination and categorization of sulcal patterns

Anatomist, the visualization tool provided by *BrainVISA*, allows a visualization of the brain surface and optimal identification of sulcal patterns by providing a spatial synchronization of the 2D MR images and the 3D surface rendering. This visualization tool allowed examining the brain hemispheres separately. **Figure 3.14** shows the various sulci on orthogonal MRI slices and a 3D MRI surface rendering.

We used the four sulcal patterns classes proposed by Ono (Ono et al., 1990) to describe the sulcal arrangement in the right and left basal surface of the temporal lobe in each subject as shown in **Figure 3.15**:

Type 1: single-branch, unbroken CS connected with the rhinal sulcus (RS) anteriorly

Type 2: CS connected with the occipitotemporal sulcus (OTS), but separated from the RS

Type 3: CS separated from the OTS and RS, which are connected

Type 4: CS, OTS and RS separated

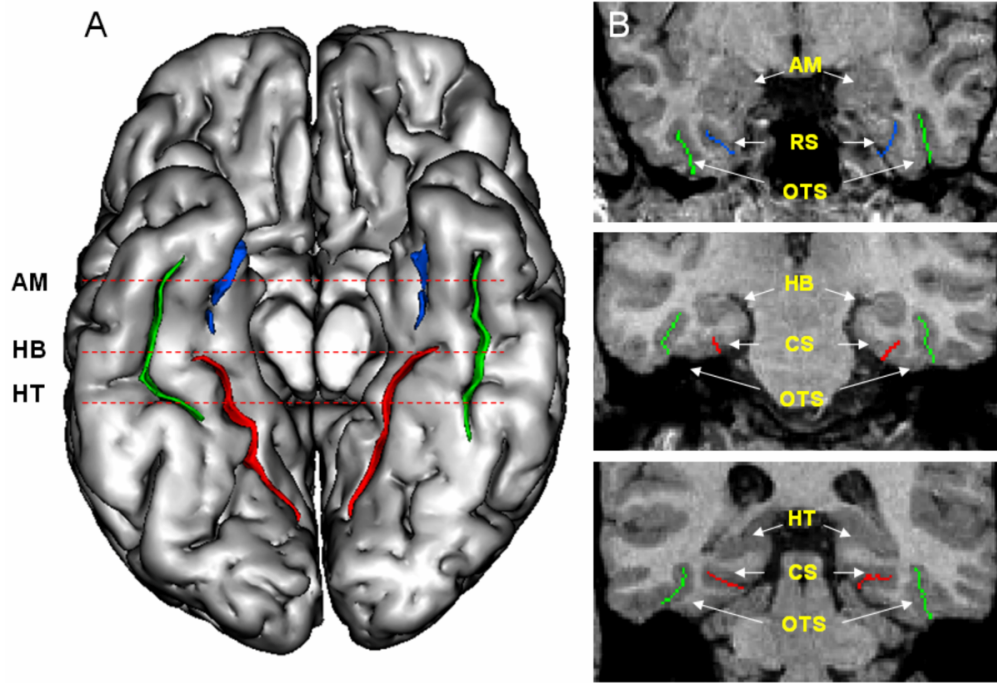


Figure 3.14. 3D surface rendering (A) and coronal MRI slices of the basal temporal lobe (B) showing the collateral sulcus (CS, red), rhinal sulcus (RS, blue) and occipitotemporal sulcus (OTS, green). AM = amygdala; HB = hippocampal body; HT = hippocampal tail.

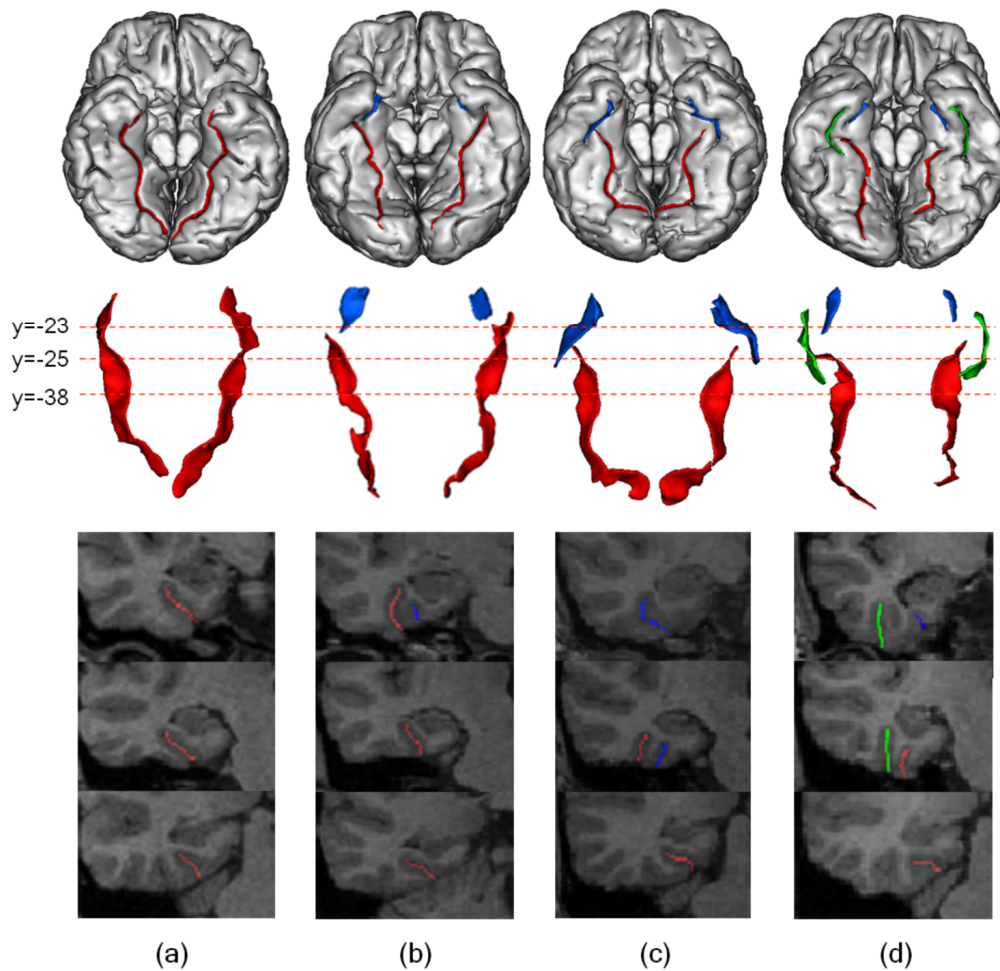


Figure 3.15. Upper panels show a basal view of the 3D MRI rendering of the brain with sulci mapped on the cortical surface.

Middle panels show the extracted sulci: collateral sulcus (CS, red), rhinal sulcus (RS, blue) and occipitotemporal sulcus (OTS, green). Lower panels show three consecutive coronal MRI slices with sulci marked at the level of hippocampal head, body, and tail at the level indicated by the Talairach coordinates in coronal plane on the middle panels (red dashed line; $y=-23$). Sulcal pattern classes used are: (a) one-branch CS connected with rhinal sulcus (RS); (b) two-branch CS connected with occipitotemporal sulcus (OTS) in its posterior portion; (c) two-branch CS having connection between RS and OTS in its anterior portion; (d) three-branch CS with no connection between the sulci.

MRI volumetry

Volumetric analysis of the hippocampus was performed in all subjects using hippocampal labels that were obtained by manual segmentation according to our previously published protocol (Bernasconi et al., 2003b). Based on a 2 SD cutoff from the mean of healthy controls, 35/69 (51%) TLE patients were determined to have hippocampal atrophy (TLE-HA) and 34/69 (49%) had normal hippocampal volume (TLE-NV).

Qualitative assessment of the hippocampal formation shape and positioning

Qualitative assessment of hippocampal shape and positioning was performed in all subjects. This evaluation was based on a set of eight previously published criteria (Bernasconi et al., 2005a). We considered the shape and positioning of the HF as abnormal if at least three out of the eight criteria were present in the same subject.

Statistical analysis. We evaluated associations between CS branch types in each hemispheres and groups (healthy controls and TLE patients), gender, and side of seizure focus and history of febrile seizures using χ^2 -test. Associations between CS branching types and hippocampal volume and positioning changes were also analyzed using χ^2 -test.

Two raters (HK and BB) independently analyzed 35 randomly selected subjects (i.e. 70 hemispheres), including patients of all categories and healthy controls. We assessed the chance-corrected inter-rater agreement between the two observers by computing Cohen's Kappa:

$\kappa = (p_o - p_e) / (1 - p_e)$, where p_o is the overall proportion of observed agreement, p_e is the overall proportion of chance-expected agreement (Cohen, 1960). Both quantities are calculated on the basis of the 4x4 contingency matrix that

expresses all joint proportions of all possible rating combinations (e.g. the proportion of all joint events - rater1: type 1, rater2: type 3- would be in the 1st row and 3rd column) (Fleiss et al., 2003).

Results

The two raters differed only in 3 of the 70 possible ratings. We obtained a chance-corrected Cohen's $\kappa = 0.84 (0.88 - 0.27)/(1 - 0.27)$, which represents excellent agreement (Fleiss et al., 2003).

Frequencies of the various sulcal patterns types in controls and TLE patients are presented in **Table 3.4**. In healthy controls, Type 1 and Type 2 were the most frequent patterns. 82% (42/51) of subjects had the same pattern in both temporal lobes. There was no association between any sulcal pattern type and gender.

Compared to controls, in TLE patients we found: *i*) an increased frequency in pattern Type 1 (single-branch, unbroken CS connected with the RS) in the left (77% vs. 47%; $\chi^2 = 8.2$, $df = 1$, $p = 0.004$) and right hemisphere (72% vs. 41%; $\chi^2 = 9.2$, $df = 1$, $p = 0.002$); *ii*) a decreased frequency of sulcal pattern Type 2 (CS connected with the OTS, but separated from the RS) in the left (4% vs. 31%; $\chi^2 = 17.0$, $df = 1$, $p = 0.00002$) and the right hemisphere (4% vs. 35%; $\chi^2 = 19.1$, $df = 1$, $p < 0.00001$). There was no difference among groups in the frequency of Type 3 and 4 sulcal patterns. 77% (53/69) of TLE patients had the same sulcal pattern in both temporal lobes.

There was no relationship between sulcal patterns and seizure focus lateralization, or any associations between CS sulcal patterns and hippocampal volume.

Table 3.4. Frequencies of sulcal patterns types in the basal temporal lobe in healthy normal controls (NC) and patients with temporal lobe epilepsy (TLE).

Sulcal pattern	NC (n=51)		TLE (n=69)	
	Left	Right	Left	Right
Type 1: CS connected with the RS				
	24/51 (47%)	21/51 (41%)	53/69 (77%)*	50/69 (72%)*
Type 2: CS connected with the OTS, but separated from the RS				
	16/51 (31%)	18/51 (35%)	3/69 (4%)**	3/69 (4%)**
Type 3: CS separated from the OTS and RS, which are connected				
	3/51 (6%)	2/51 (4%)	6/69 (9%)	8/69 (12%)
Type 4: CS, OTS and RS separated				
	8/51 (16%)	10/51 (20%)	7/69 (10%)	8/69 (12%)

*: p<0.005; **: p<0.00005

Table 3.5. Proportion of patients with childhood febrile seizures and shape and positioning changes of the hippocampal formation (HF) for each sulcal pattern.

Sulcal pattern	Febrile seizures (138 hemispheres)	HF shape and positioning changes (138 hemispheres)
Type 1	31/103 (30%)	45/103 (44%)
Type 2	1/6 (17%)	2/6 (33%)
Type 3	5/14 (36%)	7/14 (50%)
Type 4	3/15 (20%)	6/15 (40%)

We also found no association between sulcal patterns and the presence of hippocampal shape and positioning changes or a history of febrile seizures

(Table 3.5). In relation to gender, sulcal pattern Type 1 was more frequently associated with males (male: 58/66 = 88% vs. female: 45/72 = 63%; $p = 0.001$) and Type 4 with females (male: 4/66 = 6% vs. female: 14/72 = 19%; $p = 0.03$).

Discussion

Studying the morphological patterns of the inferior surface of the temporal lobe in healthy controls and TLE, we found that more than 70% of TLE patients exhibit a single-branch, unbroken CS connected with the RS. On the other hand, more than half of the controls presented with patterns displaying a lack of continuity between the CS and the RS. In particular, a CS connected with the OTS, but separated from the RS (corresponding to Type 2), was more common in healthy controls than in TLE patients. Overall, in the majority of subjects, the same sulcal pattern was observed in both temporal lobes.

Sulcal pattern variants in healthy controls

The precise mechanisms leading to cortical folding are not well known and possibly involve a combination of factors. Mechanical forces with increased brain size include forces resulting from different tension of growth between early cortical strata (Armstrong et al., 1991; Caviness, 1975), tension along axons, dendrites, and glial processes that reduce axonal length between interactive cortical areas to the shortest possible distance (Van Essen, 1997) and changes in subcortical connectivity patterns (Rakic, 1988; Welker, 1990). Sulcal patterns may also depend on non-uniform distribution of neuronal differentiation and neurite growth (Mima and Mikawa, 2004). Hemispheric sulcal morphology is thought to be primarily modulated by a variety of non-genetic factors, including intrauterine environment (Bartley et al., 1997; Lohmann et al., 1999; Mohr et al., 2004; Steinmetz et al., 1995; Wiesel, 1982). On the other hand, data from morphological analysis of individual sulci suggest genetic encoding (Le Goualher

et al., 2000; Molko et al., 2003). Most sulci and gyri develop during the third trimester, and the primary and secondary fissures are visible at birth (Chi et al., 1977; Ono et al., 1990). Typically, the major sulci continue to develop after birth (Jernigan et al., 1991) and during early childhood the degree of gyrification stabilizes (Zilles et al., 1988). The CS is among the deep sulci that appear early during human gestation, around the 23rd week' s gestation (Chi et al., 1977).

Although the basic topological pattern of gyri and sulci is maintained across humans, the precise topographic arrangement of each individual sulcus shows a high degree of variability between individuals (Bailey and Von Bonin, 1951). *Post mortem* studies have reported variable folding patterns in the inferior surface of the temporal lobe (Gloor, 1997; Ono et al., 1990). Studying 25 non-diseased brains, Ono et al. (Ono et al., 1990) described CS categories based on its connection patterns to the neighboring sulci and found that the CS was connected with the RS in 26% of the specimens. Examining five human brains of the Yakovlev Collection, which were serially sectioned in the frontal plane, Gloor (Gloor, 1997) found only one brain presenting an unbroken long collateral sulcus extending into the uncus region. The relatively low percentages of this pattern compared to our results could be partly explained by the limited number of brain specimens included in these studies. Our findings in 51 healthy controls are in agreement with previous *in vivo* MRI studies that used similar number of subjects and showing an unbroken single-branch CS connected with the RS in about 45% of individuals (Pruessner et al., 2002). These studies also reported comparable proportions of the other sulcal patterns, namely Type 2 and 3 in about 35% and Type 4 in 20% of subjects. This suggests that identification of sulcal patterns on MRI, in particular when using 3D surface models, can be reliable and as accurate as *postmortem* evaluations. Also, MRI and 3D rendering allow studies of increased number of cases compared to *ex vivo* analysis and are therefore suitable to assess sulcal variability.

We found a high inter-hemispheric similarity in sulcal arrangement in the basal temporal lobe. There are indications that the greatest inter-hemispheric sulcal pattern variability is found in the frontal and parieto-occipital regions (Luders et

al., 2004; Ono et al., 1990). However, previous studies in healthy controls (Ochiai et al., 2004; Sowell et al., 2002) and diseased populations (Kippenhan et al., 2005; Levitt et al., 2003) have been focused on inter-hemispheric asymmetries of sulcal length, depth, position, or angle and did not assess inter-hemispheric characteristics of inter-sulcal relations. Therefore, our results complement previously published data.

TLE is associated with a “simplified” sulcal anatomy of the basal temporal lobe

Type 1 single-branch, unbroken long CS connected with the RS was present in more than 70% of our TLE patients, while Type 2 (i.e., CS connected with the OTS, but separated from the RS) was found in only 4% of them.

To our knowledge, only one previous paper investigated individual variations in the sulcal anatomy of the basal temporal lobe in TLE (Novak et al., 2002). Using coronal MR images, the authors found a CS Type 1 only in 33% of the subjects. The low incidence may be explained by the use of low resolution MRI data with a slice thickness varying between 2 and 4 mm, which could lead to an incorrect determination of the sulcal depth, connectivity and interruption. The high-resolution MR images with isotropic voxels, no inter-slice gap and a 1mm thickness we used in this study allowed for a better identification of sulcal patterns. The use of advanced MR image processing enabled us not only to inspect brain surfaces in a similar way as in *postmortem studies*, but also to create 3D sulcal models that allow a comprehensive spatial evaluation of sulcal morphology. Finally, compared to the above study, the comparison with a set of healthy controls in our cohort, allowed us to establish that Type 1 CS is indeed the predominant sulcal pattern in TLE.

We did not find any association with sulcal patterns and the side of the seizure focus, indicating that the location of the epileptogenic focus and morphological changes may not necessarily overlap. Furthermore, the various patterns

occurred regardless of the presence of mesio-temporal atrophy on MRI. Expected effects of atrophy would rather be a displacement of the position of a sulcus without changes of its morphology (Molko et al., 2004).

“Simplified” temporal lobe sulcal pattern: a marker of abnormal connectivity?

Cortical complexity is usually used to describe the frequency of gyrification in a particular region of the brain (Luders et al., 2004; Zilles et al., 1988). Comparing the overall sulcal shape and organization in our subjects, Type 1 CS appears as “simplified”, since its relationship with the surrounding sulci produces a low degree of complex arrangement (**Figure 3.14**). The simplified sulcal arrangement may be the result of various overlapping mechanisms and could suggest an incomplete maturation of the inferior temporal lobe.

The pattern of folding is an effect of the massive expansion of cortical gray matter and the development of interconnecting circuits. Accordingly, cortical sulci form macroscopic landmarks of functional areas (Dumoulin et al., 2000; Yousry et al., 1997). It is generally assumed that a “normal” gyral pattern, albeit with a wide amount of variation, exists when neuronal connections are constructed properly during development. Variations in sulco-gyral patterns that exceed normal variance may therefore reflect deviations in cortical connections. Since the development of the temporal lobe is characterized by progressive folding involving several adjacent structures, a disruption in the genesis of any of these structures could potentially have consequences on the development of the others (Hines, 1922; Humphrey, 1967; Macchi, 1951). Experimental lesion studies in monkeys indicate that the disruption of afferent pathways, when occurring very early in pregnancy, can lead to the emergence of abnormal sulcal/gyral patterns (Rakic, 1988). We previously showed that the degree of volumetric reduction in densely interconnected temporal lobe regions is similar (Bernasconi et al., 2003b). Likewise, a modification in sulco-gyral pattern could occur via input alteration. Therefore, it is tempting to speculate that the relative simplification (or

loss of complexity) found in TLE could reflect variations in the underlying, possibly disturbed neuronal connectivity involving the subplate during the early stages of corticogenesis, particularly at the level of cortico-cortical connections. A modified connectivity in cortical areas adjacent to the CS known to be involved in the epileptogenic network in TLE, particularly the entorhinal and perirhinal cortices (Bartolomei et al., 2001; Bernasconi et al., 2003a; Bernasconi et al., 2003b; Bertram et al., 1998; Du et al., 1995), could lead to the distinctive sulcal pattern variant that we found to be typically associated with this form of epilepsy.

The first primordial entorhinal cortex can be detected towards the end of the third fetal month. The parahippocampal gyrus completes folding by the 6th month (Chi et al., 1977). The formation of the neighboring isocortex and the hippocampus is completed later. Which anatomical region represents the primary abnormality in our TLE patients remains unclear. However, it is plausible that an early lesion in the parahippocampal region could lead to a disturbance in the development of the sulco-gyral pattern of the basal temporal lobe.

Sulco-gyral patterns: an indicator of subtle dysplasia predisposing to TLE?

Our findings raise the question as to whether the characteristic sulcal arrangement in the basal temporal lobe of our TLE patients is a marker of a subtle malformation of cortical development.

A phenomenon yet unresolved is the overt discrepancy between the large percentage of TLE patients reporting initial precipitating insults and the fact that only few children experiencing such insults subsequently develop mesial TLE (Verity, 1998). In that context, several authors have proposed a second-hit hypothesis, where some pre-existing abnormality is constituting a susceptibility factor, predisposing the temporal lobe to a focal insult, thereby triggering the epileptogenic process. Cerebral dysplastic lesions have been suggested as candidates, because these are developmental malformations clearly present before the onset of epilepsy (Blumcke et al., 2002; Tassi et al., 2002; Thom et al.,

2002b) and often associated with intractable epilepsy. However, most cases of TLE show only MR signs of hippocampal sclerosis (Sloviter and Pedley, 1998). The concept, therefore, was expanded to include microscopical cortical dysplasia, which represents an increasingly recognized cause of TLE (Palmini et al., 2004; Tassi et al., 2002). The prototypes of these lesions are Type IA (architectural) and IB (cytoarchitectural) cortical dysplasia that are characterized by subtle cortical laminar dysorganization without cytoskeletal abnormalities or balloon cells (Palmini et al., 2004; Tassi et al., 2002). Such subtle cortical development abnormality, overlooked or not visible on MRI, may leave the temporal lobe more vulnerable to precipitating injuries occurring as early as the third trimester of gestation.

An early nature of the precipitating event is supported by our results showing the lack of relationship between sulcal morphology and history of febrile seizures in our TLE patients. The fact that this arrangement was present in more than 40% of our controls indicates that additional factors (i.e. genetic or environmental) are necessary for the emergence of the particular sulcal arrangement. Furthermore, the lack of relationship with hippocampal shape and positioning changes in our patients suggests that this phenomenon may occur independently from developmental changes in the mesial temporal areas.

In conclusion, the “simplified” sulco-gyral pattern of an unbroken CS in TLE may point to alterations in the course of corticogenesis, related either to a genetic or environmental influence, and be an important element when considering the time of origin of this disorder. It is possible that a developmentally abnormal temporal lobe may become vulnerable to injury in ways that a normal temporal lobe is not.

Chapter 4

Assessment of the impact of morphological abnormalities on automatic hippocampal segmentation in TLE

4.1 Preface

A vast number of automated hippocampal segmentation techniques have been developed to substitute the anatomical expertise-requiring, time-consuming and rater-biased manual procedures. To be suited to a clinical setting where surgical decisions are made on a patient-to-patient basis, the evaluation of sensitivity and specificity is critical prior to implementation. Recent studies have shown that segmentation performance of automated methods are satisfactory in healthy controls, reaching a degree of agreement with manual labelling that is

comparable to the inter-rater reliability (Aljabar et al., 2009; Chupin et al., 2009b; Collins and Pruessner, 2010).

In TLE, automatic segmentation algorithms have shown poorer agreement with manual labels than in healthy controls, with kappa indices ranging from 0.63 to 0.77 (Akhondi-Asl et al., 2011; Avants et al., 2010; Chupin et al., 2009b; Hammers et al., 2007; Heckemann et al., 2010; Pardoe et al., 2009). The inferior performance likely stems from factors other than atrophy, as previous approaches achieved performances similar to controls in patients with Alzheimer's disease, which is associated with marked hippocampal volume reduction (Barnes et al., 2008; Chupin et al., 2009a; Leung et al., 2010).

Using surface-based techniques developed in Chapter 3, our comprehensive analysis shows that in addition to hippocampal atrophy, malrotation, which is characterized by atypical positional changes, is present in a large percentage of TLE patients relative to controls. Moreover, we revealed an altered morphology of cortices surrounding the hippocampus in TLE.

In this chapter, we evaluated the impact of morphological abnormalities in the hippocampus and its surroundings on the performance of two state-of-the-art automated methods. We chose two algorithms previously used in this capacity (Chupin et al., 2009b; Pardoe et al., 2009): SACHA, a region growing-based approach that utilizes rule-based detection of anatomical landmarks (Chupin et al., 2009b), and FreeSurfer (Fischl et al., 2002), a freely available algorithm based on the non-linear warp of a target image to a probabilistic atlas. Segmentation accuracies were evaluated relative to manual volumetry using overlap indices and surface-based shape mapping. We then correlated these accuracy indices with 3D descriptive model-based metrics characterizing hippocampal malrotation. To guarantee high statistical power, we included a large dataset of patients and controls.

4.2 Manuscript 4

Submitted to *Neuroimage*.

Automatic hippocampal segmentation in temporal lobe epilepsy: impact of developmental abnormalities

Hosung Kim^{1,2}, Marie Chupin³, Olivier Colliot³, Boris C. Bernhardt², Neda Bernasconi², Andrea Bernasconi²

¹Department of Biomedical Engineering, ²Department of Neurology and Neurosurgery and Brain Imaging Center, McGill University, Montreal Neurological Institute and Hospital, Montreal, Quebec, Canada and ³Cognitive Neuroscience and Brain Imaging Laboratory, CNRS, UPR 640, Université Paris 6, Hôpital de la Salpêtrière, Paris, France

Abstract

In drug-resistant temporal lobe epilepsy (TLE), detecting hippocampal atrophy on MRI is important as it allows defining the surgical target. The performance of automatic segmentation in TLE has been so far considered unsatisfactory. In addition to atrophy, about 40% of patients show developmental abnormalities presenting as atypical morphologies of the hippocampus and collateral sulcus, referred to as malrotation. Our purpose was to evaluate the impact of malrotation and atrophy on the performance of two state-of-the-art automated algorithms. We segmented the hippocampus in 66 patients and 35 sex- and age-matched healthy subjects using SACHA, a region-growing algorithm constrained by anatomical priors, and FreeSurfer, a freely available atlas-based software. To quantify malrotation, 3D models were created from manual hippocampal labels and automatically extracted collateral sulci. Segmentation accuracy of automated techniques was evaluated relative to manual labeling using the Dice similarity index and surface-based shape mapping, for which we computed vertex-wise displacement vectors between automated and manual segmentations. We then correlated segmentation accuracy with malrotation features and atrophy. Although, SACHA outperformed FreeSurfer (mean Dice index: 79.4 ± 6.2 vs. 68.9 ± 5.4 ; $t=15.4$, $p<0.001$), both algorithms showed lower accuracy in patients compared to controls. Surface-based analysis of contour accuracy revealed that SACHA over-estimated the lateral convexity of the hippocampus in presence of malrotation ($r=0.61$; $p<0.0001$), but performed well in the presence of atrophy ($|r|<0.34$; $p>0.2$). Conversely, FreeSurfer was affected by both hippocampal malrotation ($r=0.57$; $p<0.02$) and atrophy ($r=0.78$, $p<0.0001$). Compared to manual volumetry, the automated procedures detected smaller effect sizes of atrophy (Cohen's d : manual: 1.68; SACHA: 1.1; FreeSurfer: 0.9, $p<0.0001$). In addition, they tended to less accurately lateralize the seizure focus in the presence of malrotation (manual: 64%; SACHA: 50%, $p=0.1$; FreeSurfer: 41%, $p=0.05$). Hippocampal developmental anomalies are prevalent not only in TLE, but may occur in neuro-psychiatric disorders in which the temporal lobe is implicated. Our results showing suboptimal performance of

automated methods in the presence of malrotation imply atypical morphologies to be taken into account when designing segmentation algorithms.

Introduction

Temporal lobe epilepsy (TLE) is the most frequent form of drug-resistant epilepsy. The majority of patients display hippocampal sclerosis, a lesion characterized by various degrees of neuronal loss and astrocytic gliosis (Babb and Brown, 1987). On MRI, hippocampal sclerosis generally appears as atrophy and signal changes (Jackson et al., 1990). Detecting hippocampal sclerosis is clinically relevant, as it allows to define the surgical target and is associated with favorable surgical outcome in more than 70% of patients (Schramm and Clusmann, 2008).

Manual delineation of the hippocampus is considered the gold standard, as it is accurate, reproducible and sensitive to detect atrophy (Bernasconi et al., 2003b; Jackson et al., 1993a; Kuzniecky et al., 1999). On the other hand, time requirement, rater-bias, and increased demand to study large cohorts of healthy and diseased populations have motivated the development of automated segmentation procedures. Most methods employ deformable (Kelemen et al., 1999; Yang and Duncan, 2004), appearance-based (Avants et al., 2010; Duchesne et al., 2002) or atlas-based approaches (Aljabar et al., 2009; Collins and Pruessner, 2010; Fischl et al., 2002; Khan et al., 2008; Lotjonen et al., 2010). Modeling spatial relationships and texture has improved segmentation accuracy (Avants et al., 2010; Chupin et al., 2009b). Although algorithms, study groups, imaging type and performance metrics vary across studies, results in healthy controls have generally been satisfactory, with kappa agreement indices ranging from 0.75 to 0.89 (Aljabar et al., 2009; Chupin et al., 2009b; Collins and Pruessner, 2010; Khan et al., 2008; Lötjönen et al., 2011).

In TLE, automatic segmentation algorithms have shown less good agreement with manual labels than in healthy controls, with kappa indices ranging from 0.63 to 0.77 (Akhondi-Asl et al., 2011; Avants et al., 2010; Chupin et al., 2009b; Hammers et al., 2007; Heckemann et al., 2010; Pardoe et al., 2009). The reduced performance likely stems from factors other than atrophy, as previous approaches achieved performances similar to controls in patients with

Alzheimer' s disease, a disorder associated with marked hippocampal volume reduction (Barnes et al., 2008; Chupin et al., 2009a; Leung et al., 2010). Indeed, in addition to atrophy, about 40% of TLE patients show atypical shape and positioning of the hippocampus (Bernasconi et al., 2005a; Voets et al., 2011). These features, commonly referred to as malrotation, are considered markers of neurodevelopmental anomalies (Baulac et al., 1998; Voets et al., 2011) and may contribute to the pathogenesis of this condition (Blumcke et al., 2002; Sloviter et al., 2004). They are mainly characterized by a rounder appearance and atypical orientation of the hippocampus, and an abnormally deep and verticalized collateral sulcus (Baulac et al., 1998; Bernasconi et al., 2005a). Malrotation features thus not only alter the hippocampal morphology, but also modify its spatial relationship with surrounding structures.

Our purpose was to evaluate the impact of malrotation, quantified through 3D descriptive models (Kim et al., 2006; Voets et al., 2011), on the performance of two fully automated hippocampal segmentation algorithms in TLE. We chose two algorithms previously used in this condition (Chupin et al., 2009b; Pardoe et al., 2009): SACHA, a region growing-based approach that utilizes rule-based detection of anatomical landmarks (Chupin et al., 2009b), and FreeSurfer (Fischl et al., 2002), a freely available algorithm based on the non-linear warp of a target image to a probabilistic atlas. Segmentation performance was evaluated relative to manual volumetry using overlap indices and surface-based shape mapping. In addition, we assessed the ability of automated methods to lateralize the seizure focus using linear discriminant analysis.

Methods

Subjects

We studied 66 consecutive patients (36 males; 16-44 years, mean age 36±10 years) referred to our hospital for the investigation of drug-resistant TLE.

Demographic and clinical data were obtained through interviews with the patients and their relatives. TLE diagnosis and lateralization of the seizure focus into left TLE (LTLE; n=35) and right TLE (RTLE; n=31) were determined by a comprehensive evaluation including video-EEG recordings and MRI evaluation in all patients. None of the patients had a mass lesion (tumor or vascular malformation), developmental malformation of the neocortex (cortical dysplasia, heterotopia or polymicrogyria), or traumatic brain injury. Forty-eight patients underwent surgery. Mean follow-up time was 3.1 ± 3.4 years. We determined surgical outcome according to Engel's modified classification (Engel et al., 1993). Thirty-four (71%) patients had Class I outcome, 5 (10%) Class II, 5 (10%) Class III and 4 (8%) Class IV. Following qualitative histopathological analysis (Meencke and Veith, 1991), hippocampal sclerosis was detected in 41/48 (85%) of patients in whom hippocampal specimen was available. In the remaining seven, hippocampal specimens were either incomplete or unsuitable for histopathology due to subpial aspiration.

The control group consisted of 35 age- and sex-matched healthy individuals (19 males; 20-56 years, mean age 32 ± 12 years). The Ethics Committee of the Montreal Neurological Institute and Hospital approved the study, and written informed consent was obtained from all participants.

MRI acquisition and processing

MR images were acquired on a 1.5 T Gyroscan (Philips Medical Systems, Eindhoven, The Netherlands) using a 3D T1-fast field echo sequence (TR=18 ms; TE=10 ms; NEX=1; flip angle=30°; matrix size=256×256; FOV=256×256 mm²; slice thickness=1 mm), providing an isotropic voxel of 1mm³ volume. Prior to processing, images underwent automated correction for intensity non-uniformity and intensity standardization (Sled et al., 1998).

Hippocampal segmentation

The hippocampus was segmented manually according to our previously published protocol (Bernasconi et al., 2003b). Prior to segmentation, MR images were linearly registered into a standardized stereotaxic space based on the Talairach atlas (Collins et al., 1994).

We performed automatic hippocampal segmentations in native space using SACHA (Chupin et al., 2009b) and FreeSurfer (Fischl et al., 2002) as detailed below.

- a. *SACHA*. This algorithm simultaneously segments the hippocampus and the amygdala based on a competitive region deformation that is constrained by automatically detected anatomical landmarks and probabilistic prior. To initialize the iterative deformation process, SACHA first warps probabilistic atlases of the hippocampus and amygdala (based on a sample of 16 healthy subjects) to a given target image in native space using ANIMAL a piece-wise linear coarse-to-fine deformation (Collins et al., 1995). We chose ANIMAL instead of the original nonlinear registration based on the discrete cosine basis (Ashburner and Friston, 1999) originally adopted in SACHA, because a recent study (Guizard et al., 2009) demonstrated that the performance of the former is comparable to diffeomorphic registration techniques. During the deformation, voxels along the boundaries of the object are iteratively reclassified to minimize a global energy functional. This process is constrained by anatomical priors derived from a set of landmarks (Chupin et al., 2007) and by the probabilistic atlases.
- b. *FreeSurfer*. In this approach, the hippocampus is segmented using a non-linear template matching (Fischl et al., 2002). The algorithm initially estimates the non-linear transformation between a given MRI and a probabilistic atlas of the hippocampus constructed from a cohort of 14 young and middle-aged subjects using a maximum likelihood criterion. Probabilistic atlas labels are warped back to the individual MRI using the inverse of this transform. The final segmentation is accomplished by maximizing the a

posteriori probability in the Bayes formula at each voxel, where probabilistic labels and their predicted image intensities serve as the prior probability term, while the intensity similarity between the target image and the template serves as the likelihood term.

We mapped automatically generated hippocampal labels to Talairach space using the linear transformation matrix generated for manual segmentation.

Models of hippocampal malrotation

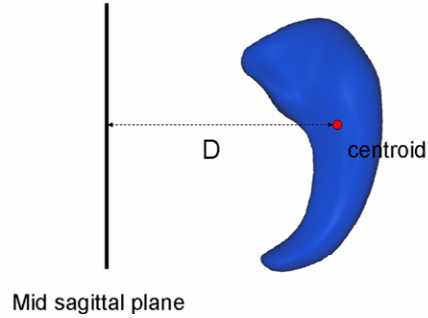
The most representative indicators of hippocampal malrotation are medial positioning, vertical orientation, and increased depth of the collateral sulcus (Baulac et al., 1998; Bernasconi et al., 2005a). To quantify these characteristics, 3D models of the left and right hippocampi in each subject were created from manual labels and automatically extracted sulci as previously described (Kim et al., 2008a; Voets et al., 2011) and detailed below.

- a. *Sagittal translation* (**Figure 4.1A**), measuring the position of the hippocampus relative to the midline, was calculated as the distance between the geometric centre of the hippocampus and the mid-sagittal plane.
- b. *Axial rotation* (\hat{e}_{axial} ; **Figure 4.1B**), reflecting a medial-lateral deflection of the hippocampus relative to its geometric centre, measured the degree of rotation with respect to the z-axis between the 1st principal (*i.e.*, longitudinal) axis ($\mathbf{v}_{1,T}$) of a given hippocampus and the 1st principal axis ($\mathbf{v}_{1,R}$) of a reference hippocampus (segmented manually on the MNI ICBM-152 template). \hat{e}_{axial} was positive, respectively negative, when the caudal portion of the hippocampus was more medially, respectively laterally, positioned relative to its rostral portion.
- c. *Longitudinal rotation* (\hat{e}_{long} ; **Figure 4.1C**), indicating a relative vertical deviation of the hippocampus from its normal horizontal orientation. By aligning the 1st principal axis of a target hippocampus ($\mathbf{v}_{1,T}$) to that of the reference ($\mathbf{v}_{1,R}$)

using a rotation matrix (so that $\mathbf{v}'_{1,T} = \mathbf{v}_{1,R}$), the 2nd principal axis of the target ($\mathbf{v}_{2,T}$) was rotated to $\mathbf{v}'_{2,T}$. \hat{e}_{long} was measured as the angle between the 2nd principal axis of the target ($\mathbf{v}'_{2,T}$) and the reference ($\mathbf{v}_{2,R}$). \hat{e}_{long} was positive, respectively negative, when the target hippocampus was more vertically oriented than the reference due to upward, respectively downward, rotation.

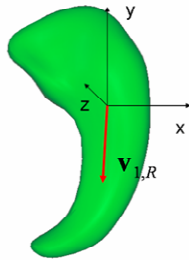
- d. *Collateral sulcus depth.* Using BrainVISA (Riviere et al., 2002), we reconstructed surfaces corresponding to GM-WM and GM-CSF interfaces and automatically extracted the collateral sulcus, that we converted into a binary set of voxels. The accuracy of the extraction was verified in all subjects prior to further analysis. To measure its depth, we first defined the sulcal bottom point on the coronal plane as the inner edge of the sulcus (Cachier et al., 2001). The depth of this point was determined by calculating the shortest distance computed using Chamfer's transform (Borgefors, 1986) from the outer cortical surface (Smith, 2002). Lastly, we averaged the depths of all sulcal bottom points on consecutive coronal slices within the extent of the hippocampus.

A Sagittal translation

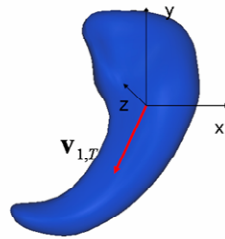


B Axial rotation

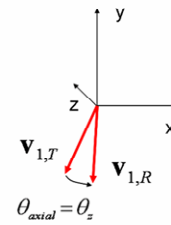
Reference hippocampus



Target hippocampus

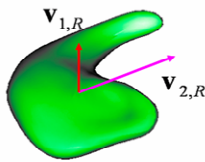


Axial rotation

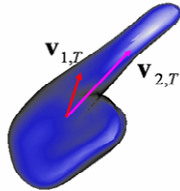


C Longitudinal rotation

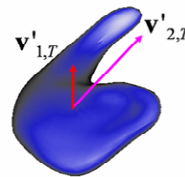
Reference hippocampus



Target hippocampus



Target after aligning $v_{1,T}$ to $v_{1,R}$



Longitudinal rotation

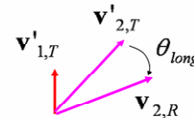


Figure 4.1. Models of hippocampal malrotation.

A) Sagittal translation (D); **B)** Axial rotation θ_{axial} ; **C)** Longitudinal rotation θ_{long}

Abbreviations: V_1 , V_2 : 1st and 2nd principal hippocampal axes, respectively; T , R : target and reference hippocampi, respectively.

Measurements were normalized through a z-transform relative to the corresponding distribution of healthy controls. A feature was considered abnormal if its z-score was 2 standard deviations (SD) above the mean of controls (**Table 4.1**).

Table 4.1. Prevalence of hippocampal malrotation based on a 2 standard deviation cutoff from the distribution of healthy controls.

	Sagittal translation		Axial rotation		Longitudinal rotation		Collateral sulcus depth	
	<i>Left</i>	<i>Right</i>	<i>Left</i>	<i>Right</i>	<i>Left</i>	<i>Right</i>	<i>Left</i>	<i>Right</i>
Controls (n=35)	1 (3%)	1 (3%)	2 (3%)	1 (3%)	1 (6%)	1 (3%)	2 (6%)	1 (3%)
LTLE (n=35)	10 (29%)	2 (6%)	9 (26%)	3 (9%)	8 (23%)	1 (3%)	12 (34%)	3 (9%)
RTLE (n=31)	7 (23%)	9 (29%)	6 (19%)	2 (6%)	1 (3%)	6 (19%)	11 (35%)	6 (19%)

LTLE/RTLE: left/right temporal lobe epilepsy

Performance evaluation of automated segmentation algorithms

- a. *Volume-based correlations.* To evaluate the ability of each automatic segmentation algorithm to capture variability in volume, we computed Pearson correlations between manual and automated labels.
- b. *Volume-based Dice index.* To quantify the accuracy of automatic segmentation, we computed the Dice similarity index:

$D = 2 \times v(M \cap A) / (v(M) + v(A))$, where M/A are the voxels comprising manual/automated labels; “M ∩ A” are voxels in the intersection of M and A; v (·) is the volume operator. For each algorithm, we compared Dice indices between patient groups (*i.e.* LTLE and RTLE) and controls using Student's t-tests. Inter-hemispheric differences were assessed using paired t-tests.

In a separate analysis, we assessed the sensitivity of the automatic algorithms to detect atrophy in TLE groups relative to controls by computing

Cohen's d (mean volume controls – mean volume TLE) / pooled SD), a measure that indicates the effect size of a between-group difference. We computed the significance of the observed effect using t-tests.

Significances were adjusted for multiple comparisons using Bonferroni-correction.

- c. *Surface-based analysis of contour accuracy.* To assess potential systematic shape bias, manual and automated labels were converted to surface meshes and parameterized using an area-preserving, distortion-minimizing mapping technique based on spherical harmonics (SPHARM) (Styner et al., 2006). Based on a uniform icosahedron-subdivision of the SPHARM, we obtained a point distribution model (PDM) with shape-inherent surface point (*i.e.*, vertex) correspondence across subjects. For each algorithm, we pooled controls and patients, computed the surface-normal component of the displacement vector between the automated and manual label at each vertex, and then employed vertex-wise t-tests on the differences (Morey et al., 2009). In addition, we mapped the SD of the displacement vector at each vertex. Differences in SD between SACHA and FreeSurfer were assessed using F-tests. Significances were thresholded at a false discovery rate < 0.05 (Benjamini and Hochberg, 1995).
- d. *Performance evaluation with respect to hippocampal atrophy and malrotation.* For both volume-based and surface-based analyses, we used linear models to investigate the effect of hippocampal atrophy and malrotation on variations of the Dice index.

Seizure focus lateralization

For each set of hippocampal labels (*i.e.*, manual and automated), we calculated an asymmetry ratio as $2(L - R) / (L + R)$, where L/R, stands for volume of the left/right hippocampus. This ratio was standardized using a z-transform relative to the distribution of controls. To lateralize the side of seizure focus in each patient, we input the standardized ratio into a linear discriminant analysis classifier. To

maximize the specificity of the classifier, we defined decision margins so that no classification fell within the asymmetry range of healthy controls. Cross-validation was performed using a leave-one-out approach. This procedure, by which an individual patient is lateralized using only the data of all other subjects, allows an unbiased assessment of lateralization performance for previously unseen TLE cases.

Results

Correlations between manual and automated labels showed that both automated algorithms generally captured the volume variability of manual segmentation (SACHA: $r=0.86$; FreeSurfer: $r=0.90$, $p<10^{-10}$; **Figure 4.2**).

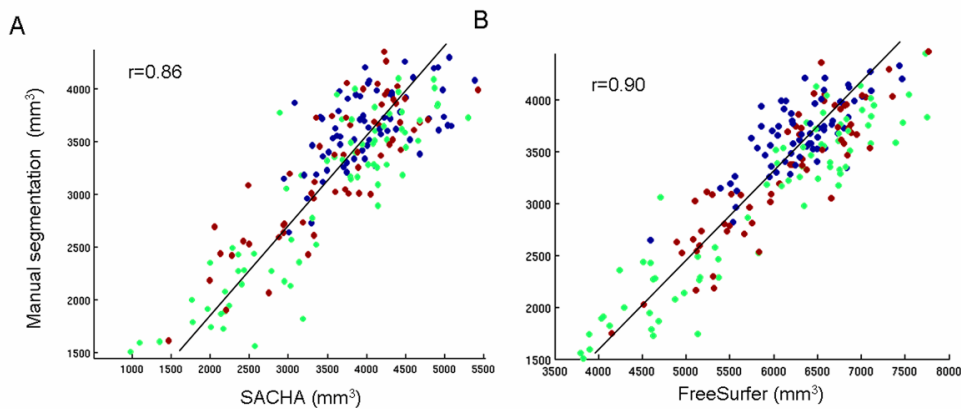


Figure 4.2. Correlation between manual and automated segmentation. SACHA (**A**) and FreeSurfer (**B**) in controls (blue), patients with left TLE (green) and right TLE (red).

Volume-based assessment of segmentation accuracy

Dice similarity indices between automated and manual hippocampal segmentations in healthy controls and TLE patients are detailed in **Table 4.2**.

Table 4.2. Evaluation of automated segmentation methods using Dice similarity index.

	SACHA		FreeSurfer	
	<i>Left</i>	<i>Right</i>	<i>Left</i>	<i>Right</i>
Controls (n=35)	81.2 (±3.3)	82.6 (±3.1)	70.1 (±2.5)* ^Δ	73.5 (±2.6)*
LTLE (n=35)	77.4 (±4.3)* ^Δ	80.8 (±3.0)	62.2 (±5.4)* ^Δ	70.4 (±3.4)*
RTLE (n=31)	79.9 (±4.9)	79.8 (±5.6)	68.2 (±3.9)*	68.4 (±5.5)*

Dice indices are presented in % mean (±SD); LTLE/RTLE: left/right temporal lobe epilepsy; (*) indicates differences in accuracy between the two algorithms; for each algorithm differences in accuracy between controls and patients is indicated in bold; (Δ) indicates hemispheric asymmetry; significances are thresholded at $p < 0.05$ after Bonferroni correction;

Although, overall SACHA outperformed FreeSurfer (mean Dice index: 79.4 ± 6.2 vs. 68.9 ± 5.4 ; $t=15.4$, $p < 0.001$), both algorithms showed lower accuracy in patients compared to controls.

For SACHA, Dice index in healthy controls did not correlate to variations in hippocampal volume or malrotation features ($|r| < 0.34$, $p > 0.2$). On the other hand, in patients, lower Dice index was correlated with increased degrees of hippocampal longitudinal rotation and collateral sulcus depth ($|r| > 0.5$; $p < 0.04$). While this effect was seen ipsilaterally in LTLE, correlations were bilateral in RTLE.

For FreeSurfer, Dice index in controls was positively correlated with the volume of the left hippocampus ($r=0.55$, $p=0.02$). In TLE patients, Dice index was influenced bilaterally by both atrophy ($r > 0.78$, $p < 0.001$) and longitudinal rotation ($|r| > 0.55$; $p < 0.02$; **Table 4.3**). Interaction analysis, however, showed that atrophy had a larger effect on the Dice than malrotation ($t > 5.4$ $p < 0.00001$).

Table 4.3. Correlations between automatic segmentation accuracy and hippocampal volume/malrotation features.

	Volume		Sagittal translation		Axial rotation		Longitudinal rotation		CS depth	
	<i>Left</i>	<i>Right</i>	<i>Left</i>	<i>Right</i>	<i>Left</i>	<i>Right</i>	<i>Left</i>	<i>Right</i>	<i>Left</i>	<i>Right</i>
SACHA										
<i>Controls</i>	0.18	0.09	-0.08	-0.06	-0.34	-0.22	-0.25	-0.32	-0.19	-0.13
<i>LTLE</i>	0.37	0.30	-0.12	-0.10	-0.35	-0.17	-0.51	-0.41	-0.55	-0.37
<i>RTLE</i>	0.31	0.43	-0.23	-0.04	-0.13	-0.11	-0.44	-0.52	-0.61	-0.68
FreeSurfer										
<i>Controls</i>	0.55	0.48	-0.05	0.03	0.05	-0.11	-0.04	-0.12	-0.24	-0.09
<i>LTLE</i>	0.77	0.79	-0.17	-0.12	-0.05	-0.33	-0.55	-0.45	-0.36	-0.31
<i>RTLE</i>	0.78	0.79	-0.13	0.05	-0.11	-0.03	-0.60	-0.55	-0.31	-0.35

Significances (in bold) are thresholded at $p < 0.05$ after Bonferroni correction for $|r| > 0.48$; LTLE/RTLE: left/right temporal lobe epilepsy

Shape analysis of segmentations

Shape differences between manual and automated hippocampal tracings are shown in **Figure 4.3**. SACHA's segmentation was similar to manual. However, SACHA systematically underestimated the supero-medial border (mean error: -0.9 ± 0.4 mm, $FDR < 0.05$) and overestimated the infero-medial region (mean error: 1.2 ± 0.8 mm, $FDR < 0.05$) corresponding to the subiculum. FreeSurfer, on the other hand, overestimated the hippocampus globally (mean error: 1.7 ± 2.1 mm, $FDR < 0.05$). Moreover, the SD of the displacement vectors was overall higher for FreeSurfer than SACHA (2.1 mm vs. 0.8 mm, $p < 0.00001$).

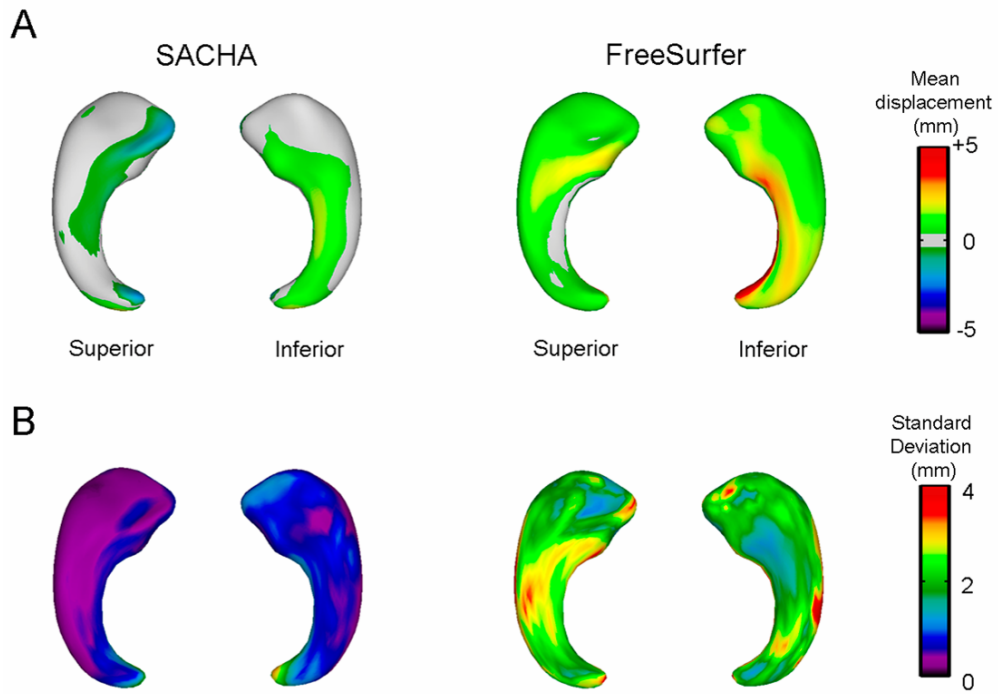


Figure 4.3. Shape differences between manual and automated tracings. For each method, maps of mean vertex-wise displacement (A) and standard deviation (B) averaged across all subjects are shown.

Impact of malrotation and atrophy upon segmentation accuracy

For SACHA, overestimation of the lateral convexity of left hippocampus was related to lower Dice index ($r=-0.67$; $FDR<0.001$, **Figure 4.4A**). In this region, we found a positive correlation between the segmentation error and the depth of the collateral sulcus ($r=0.61$; $FDR<0.001$, **Figure 4.4B**).

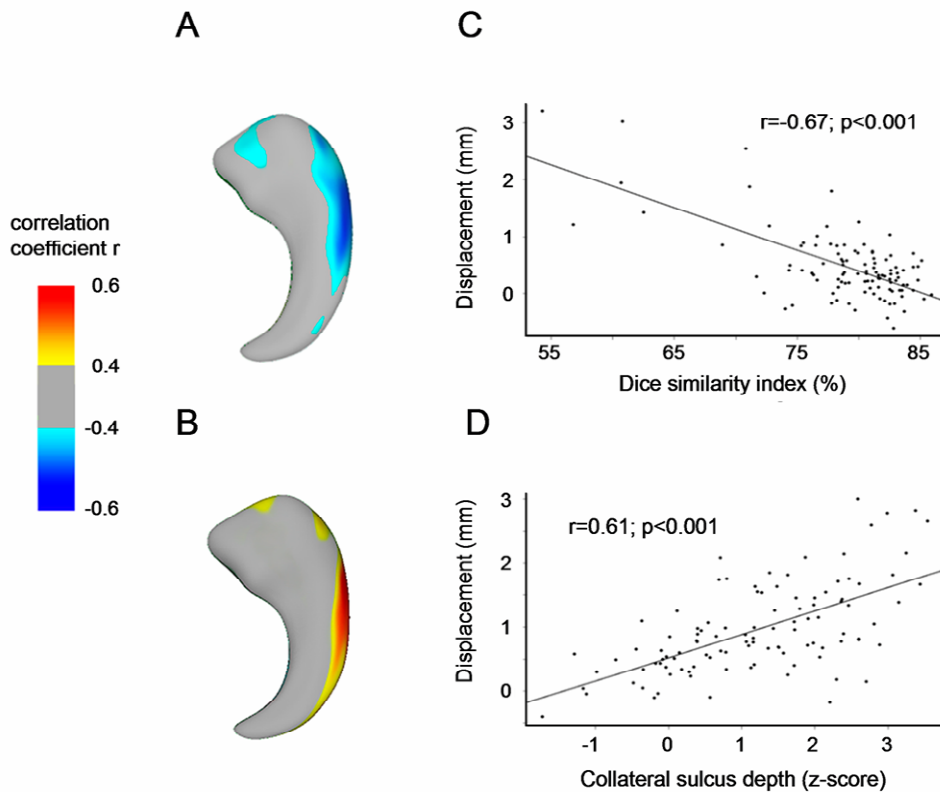


Figure 4.4. Surface-based analysis of contour accuracy.

Correlation maps and plots of vertex-wise surface-normal components of the displacement vectors between manual tracing and SACHA segmentation (*i.e.*, segmentation error) with Dice similarity index (A and C), and collateral sulcus depth (B and D).

As illustrated in **Figure 4.5**, the deeper the collateral sulcus, the more it protrudes vertically towards the wall of the lateral ventricle, thus coming in contact with the lateral border of the hippocampus. In this case, the automatic procedure tends to

erroneously include the fundus of the sulcus into hippocampal tracing. Atrophy on the other hand, did not have a negative impact on segmentation accuracy.

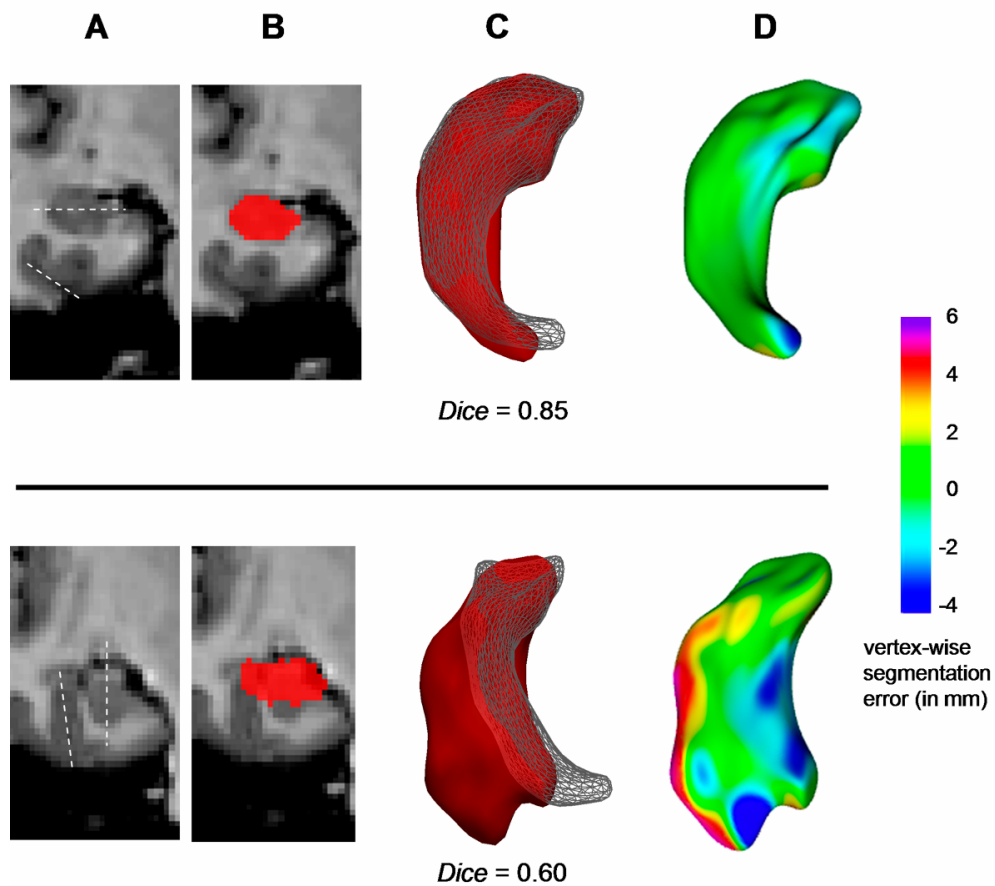


Figure 4.5. Impact of hippocampal malrotation on SACHA.

Two examples are shown: The upper panel shows a TLE patient with normally positioned hippocampus and collateral sulcus (dotted lines). The lower panel shows a patient with atypical positioning characterized by vertical orientation of both the hippocampus and the collateral sulcus. A) Coronal MRI sections; B) Hippocampal label overlaid on MRI; C) Parameterized surfaces of the automatic label (red) overlaid on the manual label (wireframe); D) Vertex-wise differences in contour (*i.e.*, segmentation error) between the two set of labels. While there is good agreement between manual and automatic segmentation when typical anatomical rules are maintained (Dice=0.85), SACHA shows poor performance in the presence of hippocampal malrotation (Dice=0.60).

For FreeSurfer, the overestimation of hippocampal volume was associated with lower Dice index across all vertices bilaterally ($r > -0.71$; $FDR < 0.001$). We also found a negative correlation between the segmentation error and volume, *i.e.* the more atrophic the hippocampus, the higher the segmentation error ($r = -0.78$; $FDR < 0.001$). There was no association between the segmentation error and malrotation ($r < 0.35$; $FDR > 0.1$).

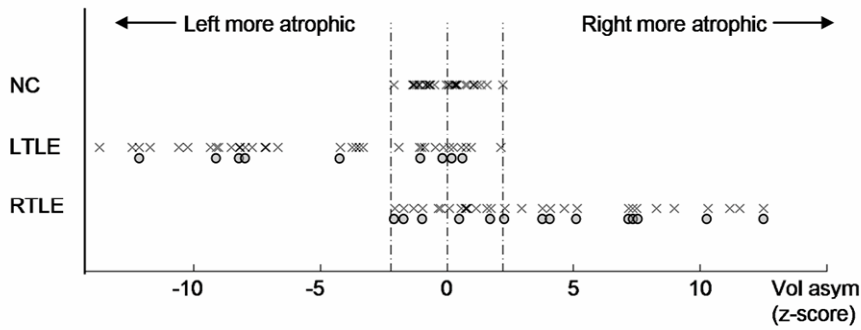
Ability of automated methods to lateralize the seizure focus

Group analysis. Both manual and automated approaches identified hippocampal atrophy ipsilateral to the seizure focus in TLE (**Table 4.3**). However, the effect size of atrophy was lower when using automated methods (Cohen's *d* LTLE/RTLE: SACHA=1.26/0.94, $t=5.2/3.8$; FreeSurfer=1.02/0.77, $t=3.9/3.6$; manual volumetry=1.96/1.41, $t=7.9/4.9$).

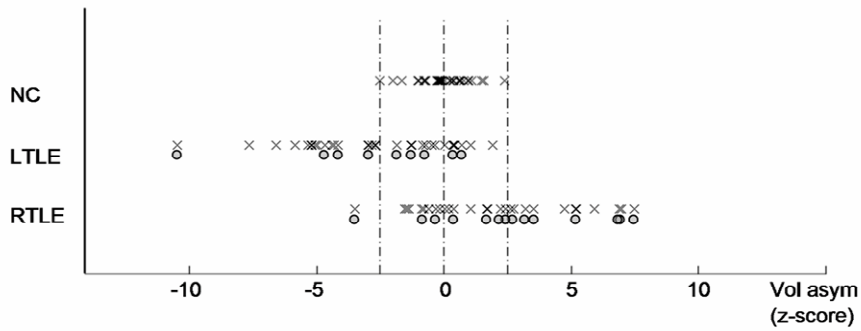
Individual analysis. Results are shown in **Figure 4.6**. Using decision margins that enforced non-classification of patients in whom asymmetry values fell within the range of healthy controls, manual volumetry correctly lateralized the side of the focus in 67% (44/66) of patients. Automated methods lateralized the seizure focus in fewer patients (SACHA: 61%=40/66, Fisher's exact test, $p=0.29$; FreeSurfer: 56%=37/66, Fisher's exact test, $p=0.14$). SACHA misclassified one RTLE patient as LTLE. In this patient with malrotation (longitudinal rotation: $z=2.1$), the volume of the right hippocampus was overestimated, because the fundus of the collateral sulcus was erroneously segmented as hippocampus.

Among the 23 patients with hippocampal malrotation, 14 (64%) were correctly lateralized using manual volumetry, 11 (50%) using SACHA and 9 (41%) using FreeSurfer (Fisher's exact test; SACHA: $p=0.15$; FreeSurfer: $p=0.05$).

A. Manual segmentation



B. SACHA



C. FreeSurfer

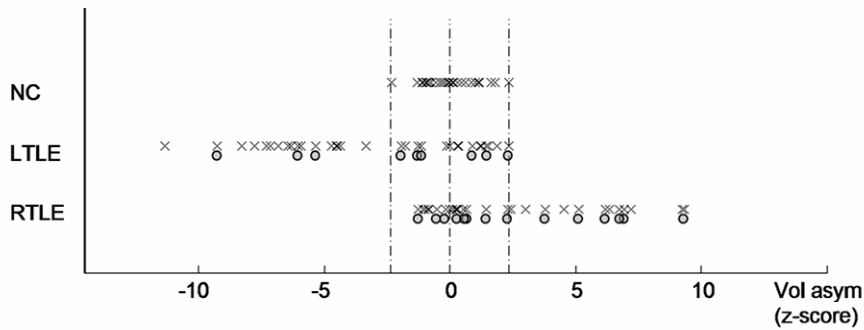


Figure 4.6. Seizure focus lateralization in TLE.

For each segmentation method, the hippocampal asymmetry ratio was standardized using z-transformation relative to the distribution of healthy controls and then fed into a linear discriminant function classifier. Crosses denote individuals in controls (NC) and patients with left/right temporal lobe epilepsy (LTLE/RTLE). Circles below the crosses identify patients with hippocampal malrotation. To maximize the specificity of the classifier, we defined decision margins (broken lines) so that no classification fell within the asymmetry range of controls.

Discussion

In this study, we quantitatively evaluated the influence of developmental shape and positioning anomalies on the performance of two state-of-the-art automatic segmentation algorithms, SACHA (Chupin et al., 2009b) and FreeSurfer (Fischl et al., 2002). Using a large database of controls and TLE patients, we observed that SACHA overestimated the volume of the lateral convexity of the hippocampus in cases with malrotation, but behaved relatively well in the presence of atrophy. The performance of FreeSurfer, on the other hand, was affected by both hippocampal malrotation and atrophy. We also found that the automated procedures detected smaller effect sizes of hippocampal atrophy and tended to be less accurate for seizure focus lateralization compared to manual volumetry. Our results suggest that the accuracy and clinical utility of automated methods are suboptimal in cases that grossly deviate from the range of normal shape variants, but also in case of marked atrophy.

Compared to manual segmentation, FreeSurfer performed relatively poorly in both healthy controls and TLE patients, a finding in agreement with two previous studies including smaller cohorts (Akhondi-Asl et al., 2011; Pardoe et al., 2009). While differences in segmentation protocols may have contributed to these unsatisfactory results (Konrad et al., 2009), consistently reduced performance across studies is more likely driven by the single averaged template constructed from only 14 healthy subjects used in this algorithm. Such template may not sufficiently capture structural variations within and beyond the distributions of controls. In addition, our results showing a downgrade in performance across the whole hippocampus in the presence of atrophy and malrotation makes a systematic bias related to segmentation protocols unlikely.

The recently developed SACHA software has been shown to be minimally affected by the presence of atrophy, as it performs with similar degrees of accuracy in patients with Alzheimer's disease and controls (Chupin et al.,

2009a). Our results are in line with this observation as SACHA performed relatively well in patients who presented with hippocampal atrophy as the predominant shape abnormality. On the other hand, hippocampal malrotation impaired the segmentation markedly. We hypothesize that the landmark models of SACHA, that are based on anatomical knowledge derived from healthy subjects, may be unsuitable when the hippocampus does not display the usual relationships with its surrounding. Indeed, surface-based shape mapping revealed segmentation errors in the presence of an unusually deep collateral sulcus. A deep, vertically oriented sulcus protrudes towards the wall of the lateral ventricle and tends to touch the lateral border of the hippocampus. In this scenario, the proximity between these two structures creates partial volume, which results in a thin and darkened parahippocampal white matter, thus decreasing its intensity gradients. As shown in **Figure 4.5**, the region growing process falsely penetrates the sulcus and includes its fundus into the tracing of the hippocampus. This type of intensity changes, however, is not likely to mislead manual delineation, since the white matter tissue remains visually distinguishable from the hippocampus. In addition, the rater generally utilizes multiple sources of information to determine anatomical landmarks.

High correlations between manual and automated procedures found in our study and in previous publications (Barnes et al., 2008; Crum et al., 2001; Morey et al., 2009; Pardoe et al., 2009) suggest that automated methods have the potential to capture volume variations to a degree similar to that of manual tracing, even in the presence of shape alterations. This may explain why, despite superior sensitivity of manual segmentation in detecting hippocampal atrophy, the proportion of TLE patients in whom the seizure focus was correctly lateralized did not statistically differ between approaches. Nevertheless, the automated methods did not determine the side of the focus in four (SACHA) and seven (FreeSurfer) patients who were correctly lateralized using manual volumetry. Moreover, their performance was further decreased by the presence of malrotation, leading to wrong focus lateralization in one patient. In a clinical

setting where decisions concerning surgery are taken on a patient-by-patient basis, even a relatively small decrease in sensitivity and lateralization performance is detrimental.

Hippocampal developmental anomalies are prevalent in TLE (Baulac et al., 1998; Bernasconi et al., 2005a; Depondt et al., 2002; Sloviter et al., 2004; Stiers et al., 2010; Voets et al., 2011), but also present in up to 60% of patient with malformations of cortical development (Baulac et al., 1998; Bernasconi et al., 2005a; Sato et al., 2001) and have been documented in schizophrenia (Connor et al., 2004). We believe therefore that atypical anatomical characteristic should be taken into account when designing automated segmentation methods. Recent algorithms based on template libraries and label fusion overcome the limitations of techniques based a single individual or averaged template (Aljabar et al., 2009; Collins and Pruessner, 2010; Hammers et al., 2007). The basic principle underlying these methods is to build expert priors-based models corresponding to shape variations (Coupé et al., 2011) and to select automatically those that best fit the structure to segment. To date, these techniques have been applied to segment healthy hippocampi. In the presence of malrotations, automatic approaches may fall into local minima when using a template or prior-knowledge based on healthy subjects. We are currently evaluating an automated segmentation based on multi-template library derived from a large cohort of healthy controls and patients that accounts for inter-subject variability, in particular shape variants.

Chapter 5

Automatic segmentation of hippocampal structures in TLE

5.1 Preface

The poor performance of automatic hippocampal segmentation in the presence of malrotation, as described by the preceding experiments, suggests that such atypical anatomical characteristics should be taken into account when designing automated segmentation methods.

As discussed in Chapter 2, recent algorithms based on a *template library and label fusion* (or *multi-template*) have the potential to overcome the inaccurate segmentation of shape variants (Aljabar et al., 2009; Collins and Pruessner, 2010; Hammers et al., 2007). The strategy underlying these approaches is the creation of a database of manual labels and their corresponding MR images (*i.e.*, atlas) (Coupé et al., 2011) and the automatic selection of those atlases that best fit the target structure to segment.

Yet, contemporary studies still have a few shortcomings. Intensity-based registration techniques used in multi-template approaches lack accurate point-wise inter-subject correspondences. Moreover, most approaches use template libraries including only healthy hippocampi, likely due to the difficulty of collecting pathological data.

We postulated that SPHARM-PDM based surface modeling and fitting (that we applied in Chapter 3) may surmount the limitation of intensity-based registration methods.

In this project, we designed a surface-based multi-template segmentation framework. To create a template library, we include a large database of healthy controls (n=40) and patients with TLE (n=144). We compared our segmentation results with those of state-of-the-art volume based single- and multi-template approaches. In addition, we evaluated the impact of hippocampal malrotation, quantified through 3D descriptive models developed in Chapter 4, on the performance of automated hippocampal segmentation algorithms.

5.2 Manuscript 5

Published in *Med. Image. Comp. Comp. Assist. Interv.* 2011. 6892

Submitted to *Neuroimage*.

Surface-based multi-template automated hippocampal segmentation: application to temporal lobe epilepsy

Hosung Kim^{1,2}, Tommaso Mansi³, Andrea Bernasconi², Neda Bernasconi²

¹Department of Biomedical Engineering, ²Department of Neurology and Neurosurgery and Brain Imaging Center, McGill University, Montreal Neurological Institute and Hospital, Montreal, Quebec, Canada and ³ Siemens Corporate Research, Image Analytics and Informatics, Princeton, NJ, USA

Abstract

The most frequent drug-resistant epilepsy is temporal lobe epilepsy (TLE) related to hippocampal atrophy. In addition, TLE is associated with atypical hippocampal morphologies referred to as malrotation. Automatic hippocampal segmentations have generally provided unsatisfactory results in this condition. We propose a novel segmentation method (SurfMulti) to statistically estimate locoregional texture and shape using a surface-based approach that guarantees shape-inherent point-wise correspondences. To account for inter-subject variability, including shape variants, we used a multi-template library derived from a large database of controls' (n=80) and patients' (n=288) hippocampi. We compared SurfMulti results to manual tracing and segmentations obtained using volume-based approaches. Lastly, we evaluated the impact of hippocampal malrotation, quantified through 3D descriptive models on the performance of the automated algorithms. SurfMulti outperformed state-of-the-art single- and multi-template approaches, with performances comparable to controls (Dice index: 86.1 vs. 87.5%). While segmentation results derived from volume-based approaches were hampered by hippocampal malrotation and atrophy ($|r| > 0.28$, $p < 0.05$), SurfMulti's performance was not influenced by either of these anomalies ($|r| < 0.20$, $p > 0.2$). Furthermore, the sensitivity of SurfMulti to detect atrophy was similar to that of manual volumetry (Cohen's d : 1.60 vs. 1.71; $p > 0.1$). Given that in TLE detecting hippocampal atrophy on MRI is clinically relevant as it allows defining the surgical target, the proposed automated algorithm assures to be a robust surrogate tool in the presurgical evaluation for the time-demanding manual procedure. Aside TLE, hippocampal atrophy and developmental anomalies may occur in epilepsy related to malformation of cortical development and a variety of other neurological and neuropsychiatric disorders such as schizophrenia and autism. The influence of these abnormalities to a broad range of disorders emphasizes the consideration of atypical anatomical characteristics when designing automated segmentation methods.

Introduction

The most frequent form of drug-resistant epilepsy is temporal lobe epilepsy (TLE) related to hippocampal sclerosis, which generally appears as atrophy on MRI (Bernasconi, 2006; Cascino, 2008; Cendes et al., 1993b; Jackson et al., 1990). Detecting hippocampal atrophy is clinically relevant as it allows lateralizing the side of seizure focus and defining the surgical target. Removing the diseased hippocampus is the only effective treatment, offering seizure freedom in up to 80% of patients (Cascino, 2004; Schramm and Clusmann, 2008).

Manual labeling is generally considered the gold standard to measure hippocampal volume, as it is accurate, reproducible, and sensitive (Bernasconi et al., 2003b; Jackson et al., 1993a; Kuzniecky et al., 1999). High time requirement and the demand to study large cohorts of healthy and diseased populations have motivated the automation of hippocampal volumetry.

Most segmentation methods employ approaches based on deformable models (Kelemen et al., 1999; Pitiot et al., 2004; Yang and Duncan, 2004), tissue appearance (Avants et al., 2010; Duchesne et al., 2002) or atlases (Aljabar et al., 2009; Collins and Pruessner, 2010; Fischl et al., 2002; Khan et al., 2008; Lotjonen et al., 2010). The use of deformable parametric surfaces based on locoregional features has improved performance in healthy controls (Pitiot et al., 2004). However, this approach estimates features on vertices arranged without anatomical correspondences that may produce inaccurate segmentation in the presence of topological discrepancies due to pathology.

In patients with TLE, automatic algorithms have generally yielded poorer results than in healthy subjects, with Dice similarity indices ranging from 0.63 to 0.77 (Akhondi-Asl et al., 2011; Avants et al., 2010; Chupin et al., 2009b). Reduced performance in TLE may stem from factors other than atrophy, as previous studies achieved results similar to controls in patients with Alzheimer's disease, a neurodegenerative disorder also associated with marked hippocampal atrophy (Chupin et al., 2009b). In fact, 40% of TLE patients show atypical morphologies

of the hippocampus and surrounding structures, referred to as malrotation (Baulac et al., 1998; Bernasconi et al., 2005a). In the presence of such abnormal anatomical variants, automatic approaches may fall into inaccurate local minima when using a template or prior-knowledge based on healthy subjects. Multi-template approaches offer a suitable framework to account for structural variability by selecting from a database a subset that best describe anatomical characteristics of the target structure. To date, these techniques have been volume-based and applied to segment healthy hippocampi (Aljabar et al., 2009; Collins and Pruessner, 2010). However, they rely on non-linear image registration, which may also fail in case of atypical morphology.

In this paper, we propose a novel hippocampal segmentation method based on a multi-template approach that relies on statistical parametric surface models and locoregional texture features (SurfMulti). We applied our method to large cohorts of healthy subjects and patients with TLE, and compared the results to manual tracing and segmentations obtained using volume based single- and multi-template approaches (Collins and Pruessner, 2010; Fischl et al., 2002). Lastly, we evaluated the impact of hippocampal malrotation, quantified through 3D descriptive models (Kim et al., 2006; Voets et al., 2011), on the performance of the automated algorithms.

Methods

Our approach consists of a template library construction stage and a segmentation stage, as illustrated in **Figure 5.1**. Each stage is detailed in the following sections.

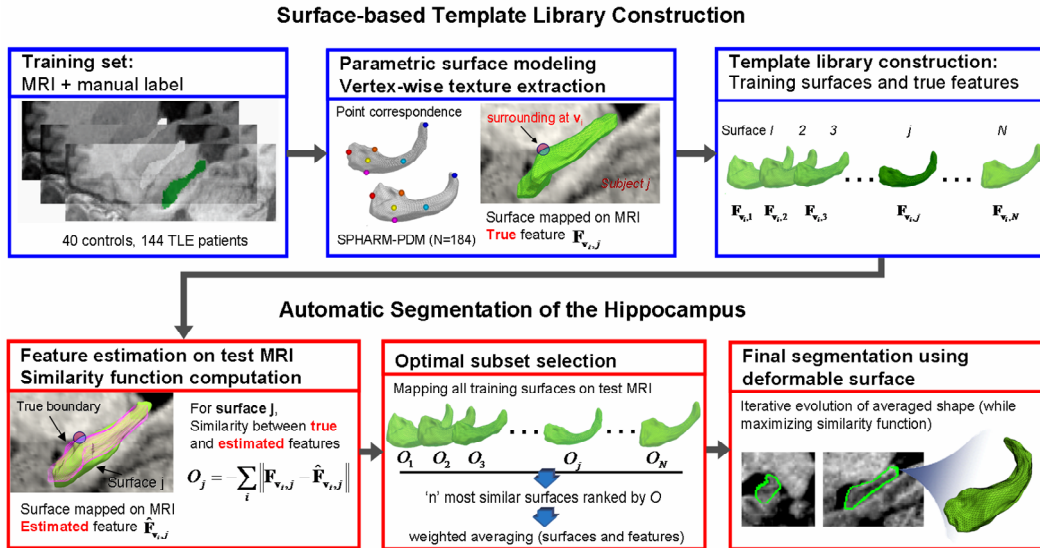


Figure 5.1. Flowchart of SurfMulti.

Our approach consists of a template library construction stage (panels outlined in blue) in which shape.

0 and texture features are trained from manual labels, and a segmentation stage (panels outlined in red) in which, for a given MRI, an optimal subset of training surfaces and features is selected based on a similarity function. The final segmentation is obtained by evolving the averaged surface of the selected subset. See text for details.

Template library construction

a. Surface extraction from manual labels

Manually segmented hippocampal labels were converted into surface meshes and parameterized using an area-preserving, distortion-minimizing mapping technique based on spherical harmonics (SPHARM). Using a uniform icosahedron-subdivision of the SPHARM, we obtained a point distribution model (PDM) with shape-inherent surface point (*i.e.*, vertex) correspondence across subjects (Styner et al., 2006).

b. Regional texture models

Each surface was mapped to its corresponding image to compute regional textures. For each vertex \mathbf{v}_i , a spherical neighborhood with various radii (3mm, 5mm, 7mm) was defined. The “inner region” (IR) and “outer region” (OR) of these local neighborhoods were determined with respect to the surface boundary. The following texture features were then computed for every \mathbf{v}_i :

- i. Normalized intensity (NI)* to capture regional tissue homogeneity. Let $\mu_{IR,i}$ and $\mu_{OR,i}$ be the mean of intensities within IR and OR at \mathbf{v}_i respectively, and $SD_{IR,i}$ and $SD_{OR,i}$ be the standard deviation. We defined $NI_{IR,i} = \mu_{IR,i} / SD_{IR,i}$ and $NI_{OR,i} = \mu_{OR,i} / SD_{OR,i}$.
- ii. Relative intensity (RI)* to assess the contrast between IR and OR voxels. RI was defined as $RI_i = 2 \times (\mu_{OR,i} - \mu_{IR,i}) / (\mu_{OR,i} + \mu_{IR,i})$.
- iii. Gabor energy (GE)* to capture image texture through a multi-channel filtering strategy (Grigorescu et al., 2002). Mimicking human visual perception, this feature portrays the complexity, directionality and repetition of the intensity distribution. Let x,y,z be the spatial coordinates and \mathbf{R}_θ a 3x3 rotation matrix whose 3D Euler angle θ defines the orientation of the normal to the parallel stripes of a Gabor function. The Gabor filter (Grigorescu et al., 2002) is defined by:

$$g_{\theta, \lambda, \sigma, \gamma, \varphi}(x, y, z) = \exp\left(-\frac{x'^2 + \gamma^2 y'^2 + \gamma^2 z'^2}{2\sigma^2}\right) \exp\left(-2\pi \frac{x'}{\lambda} + \varphi\right), \quad (x', y', z') = \mathbf{R}_{\theta}(x, y, z) \quad (1)$$

γ is the aspect constant that defines the elongation of the filter, φ is the phase offset that makes the filter asymmetric when it is non-zero and the ratio σ/λ describes the bandwidth, namely the filter size b according to:

$$b = \log_2 \frac{\pi\sigma / \lambda + \sqrt{0.5 \ln 2}}{\pi\sigma / \lambda - \sqrt{0.5 \ln 2}}, \quad \sigma / \lambda = \frac{1}{\pi} \sqrt{\frac{\ln 2}{2} \frac{2^b + 1}{2^b - 1}} \quad (2)$$

At a voxel $l(x, y, z)$, the Gabor energy is given by $GE_{\theta, \lambda, \sigma, \gamma, \varphi}(x, y, z) = \| g_{\theta, \lambda, \sigma, \gamma, \varphi}(x, y, z) * l(x, y, z) \|$, where $*$ is the convolution operator. In this work, we calculated the Gabor energy of the immediate surroundings only along the surface normal θ . We fixed φ as 0 (no offset) and γ as 1 (same amount of information horizontally and vertically). Multiscale texture analysis was performed by varying the bandwidth $b = \{0.5, 1, 2\}$.

iv. *Intensity gradient (IG)* to capture edge information. Gradients along x, y, z directions were computed and linearly interpolated on the vertices.

c. Regional shape models

The following features constrained the deformable model evolution within the range of the anatomical variability in the template.

i. *Distance between adjacent vertices* to prevent irregular vertex topology.

ii. *Gaussian curvature* to constrain local convexity/concavity.

iii. *Local orientation*. Manual tracing in regions where anatomical boundaries are not visible often rely on arbitrary oblique planes as geometric landmarks (e.g., the inferomedial border separating CA1 from the subiculum) (Konrad et al., 2009). To model this feature, we projected the surface normals to the

xy, yz and zx planes and computed their angles with respect to their orthogonal axis x, y and z-axis.

For each subject, texture and shape features were normalized across vertices using a z-transform and combined at each vertex \mathbf{v}_i into a vertex-wise vector.

$$\mathbf{F}_{\mathbf{v}_i} = \left[\mathbf{F}_{\text{texture}, \mathbf{v}_i} \quad \mathbf{F}_{\text{shape}, \mathbf{v}_i} \right]$$

Automatic Segmentation of the Hippocampus

a. Automatic selection of an optimal shape and feature template

Let $\mathbf{S}_j = [\mathbf{v}_1, \mathbf{v}_2 \dots \mathbf{v}_i \dots, \mathbf{v}_L]$ be a SPHARM-PDM surface of the template library, which is initially mapped on its own MR image. Let $\mathbf{F}_{\mathbf{v}_i, j}$ be the *true features*, i.e., the set of features computed at \mathbf{v}_i from the related MRI. Given a test image we mapped the templates $\mathbf{S}_1, \mathbf{S}_2 \dots \mathbf{S}_j \dots \mathbf{S}_N$, to the test image and computed a set of *estimated features* $\hat{\mathbf{F}}_{\mathbf{v}_i, j}$. For each mapping, we computed the following similarity measure:

$$O_j = -\sum_i \frac{\|\mathbf{F}_{\mathbf{v}_i, j} - \hat{\mathbf{F}}_{\mathbf{v}_i, j}\|}{\sqrt{\frac{1}{N} \sum_{k=1}^N (\mathbf{F}_{\mathbf{v}_i, k} - \bar{\mathbf{F}}_{\mathbf{v}_i})^2}}, \quad \bar{\mathbf{F}}_{\mathbf{v}_i} = \frac{1}{N} \sum_{k=1}^N \mathbf{F}_{\mathbf{v}_i, k} \quad (3)$$

Equation (3) represents a normalized similarity between the true-features of the j -th template and the estimated-features extracted from the test image. Based on (3), we were thus able to identify the closest templates to the test image. Two template selection approaches were investigated:

- i. *Equal weight approach.* Given a test image, we selected the n most similar templates (surfaces and their corresponding features) (Aljabar et al., 2009; Collins and Pruessner, 2010). We then averaged the n selected surfaces ($\mathbf{S}_{\text{opt } 1}, \mathbf{S}_{\text{opt } 2}, \dots, \mathbf{S}_{\text{opt } n}$) to generate an initial shape for the later segmentation process. Best results were obtained experimentally with $n=10$ templates. At each vertex, we also computed mean ($\bar{\mathbf{F}}_{\mathbf{v}_i}$) and SD

($\sigma_{F_{v_i}}$) of the true-features of the n selected surfaces (4) to compute the objective function (9) in the later segmentation stages.

$$\bar{\mathbf{F}}_{v_i} = \frac{1}{n} \sum_{j=1}^n \mathbf{F}_{v_i, opt j}, \quad \sigma_{F_{v_i}} = \frac{1}{n} \sqrt{\sum_{j=1}^n (\mathbf{F}_{v_i, opt j} - \bar{\mathbf{F}}_{v_i})^2} \quad (4)$$

ii. *Advanced adaptive approach.* Coupé et al. (Coupé et al., 2011) recently proposed a weighted averaging of the selected volume labels according to their global similarity measure. Even though our library includes a large number of pathological hippocampi, it may not cover the entire spectrum of morphological variability. Noteworthy, however, some shape and texture features in the subset may be similar to the target, and thus their separate modeling likely provides a more suitable strategy to create the optimal subset. Thus, we also investigated a weighted averaging strategy as follows:

Let \mathbf{w}_S and \mathbf{w}_F be $n \times 1$ weight vectors for optimal surfaces and features, respectively. We defined the new average surface as:

$$\bar{\mathbf{S}} = \sum_{j=1}^n w_{S,j} \mathbf{S}_{opt j}; \quad \sum w_{S,j} = 1 \quad (5)$$

Similarly, we defined the weighted mean and SD of features at vertex \mathbf{v}_i by:

$$\bar{\mathbf{F}}_{v_i} = \sum_{j=1}^n w_{F,j} \mathbf{F}_{v_i, opt j}; \quad \sum w_{F,j} = 1; \quad \sigma_{F_{v_i}} = \sqrt{\sum_{j=1}^n w_{F,j} (\mathbf{F}_{v_i, opt j} - \bar{\mathbf{F}}_{v_i})^2} \quad (6)$$

We re-defined the similarity function based on the n -top ranked subset to take into account the weights:

$$O_{subset} = -\sum_i \frac{\|\bar{\mathbf{F}}_{v_i} - \hat{\mathbf{F}}_{v_i, \bar{\mathbf{S}}}\|}{\sigma_F} \quad (7)$$

$\hat{\mathbf{F}}_{v, \bar{S}}$ is the *estimated* feature-set computed on the surface \bar{S} mapped on the test image. Finally, both weights were determined by maximizing the similarity between the current template-subset and the test image.

$$\mathbf{w} = [\mathbf{w}_S \ \mathbf{w}_F] = \arg \max_{\mathbf{w}} O_{subset} \quad (8)$$

We initially set all the components of \mathbf{w} as $1/n$. We then iteratively perturbed every w_j by $\pm\delta \cdot 1/n$ and updated it if the similarity function (7) increased. The step-size parameter δ was initialized to 1 and decreased by 0.1 at each iteration. This process stopped when either O_{subset} did not increase after the current iteration or 10 iterations were performed.

b. Automatic segmentation: evolution and objective function

The final segmentation was obtained as follows. We first linearly mapped the averaged template computed in the previous section to the test image. Then, we locally deformed the surface at each vertex along the surface normal based on a multi-level b-spline interpolation (Lee et al., 1997). We centered a b-spline function at a vertex on the current evolving surface. Using a coarse-to-fine hierarchy of control lattices, a 2D smooth scalar field was generated to adaptively interpolate the given deformation magnitude at the vertex. We then mapped these scalar values to their corresponding vertices for the later transformation. Previous multi-template approaches have shown that the shape averaged from the optimal subset produces good agreement with manual labeling (Aljabar et al., 2009; Collins and Pruessner, 2010). Therefore, the use of this averaged shape as an initial segmentation allows the subsequent local deformation to be robust against local minima and to reach convergence with few iterations.

In our algorithm, we empirically optimized the initial magnitude of deformation to be set as 5mm and decreased it at each iteration by 1mm. Inward and outward

deformations along the surface normal were tested at each vertex. The final deformation was achieved by maximizing a cost function.

Analogous to Eq. (6), the cost function was defined at iteration k as:

$$O_k = -\sum_i \left\| \bar{\mathbf{F}}_{v_i} - \hat{\mathbf{F}}_{v_i, \bar{S}_k} \right\| / \sigma_F \quad (9)$$

\bar{S}_k is a deformed surface at iteration k and $\hat{\mathbf{F}}_{v_i, \bar{S}_k}$ is its *estimated* feature vector. We maximized O_k using the gradient descent approach (Kiwiel, 2001).

Experiments and Results

Experiments

a. Subjects

Our training-set included 40 healthy controls (18 males; mean age 33 ± 12 yrs) and 144 consecutive patients (61 males; mean age 36 ± 11 yrs), referred to our hospital for the investigation of drug-resistant TLE. Demographic and clinical data were obtained through interviews with the patients and their relatives. TLE diagnosis and lateralization of the seizure focus into left TLE (LTLE; n=73) and right TLE (RTLE; n=71) were determined by a comprehensive evaluation including video-EEG recordings and MRI evaluation in all patients. None of the patients had a mass lesion (tumor, vascular malformation or malformation of cortical development), or traumatic brain injury.

The Ethics Committee of the Montreal Neurological Institute and Hospital approved the study, and written informed consent was obtained from all participants.

b. MRI acquisition and processing

MR images were acquired on a 1.5 T Gyroscan (Philips Medical Systems, Eindhoven, The Netherlands) using a 3D T1-fast field echo sequence (TR=18 ms; TE=10 ms; NEX=1; flip angle=30°; matrix size=256×256; FOV=256×256 mm²; slice thickness=1 mm), providing an isotropic voxel of 1mm³ volume.

Prior to processing, images underwent automated correction for intensity non-uniformity and intensity standardization (Sled et al., 1998) and were linearly registered into a standardized stereotaxic space based on the Talairach atlas (Collins et al., 1994). The hippocampus was segmented manually according to our previously published protocol (Bernasconi et al., 2003b). Using z-score normalization based on the distribution of healthy controls, we identified 91 (63%) patients with hippocampal atrophy (*i.e.*, $z < -2$) ipsilateral to the seizure focus.

c. Evaluation of template selection approaches

We evaluated the template selection using a leave-one out strategy. For each test data, we selected optimal subsets and built the initial shape and feature models using both the traditional and the adaptive approach. To quantify the accuracy of automatic segmentation, we computed the Dice similarity index: $D = 2 \times v(M \cap A) / (v(M) + v(A))$, where M/A are the voxels comprising manual/automated labels; “ $M \cap A$ ” are voxels in the intersection of M and A; $v(\cdot)$ is the volume operator. We then compared the segmentations resulting from each initialization using Dice index and paired t-tests.

d. Evaluation of feature contribution

To investigate the individual contribution of each feature to the segmentation performance, we segmented all healthy hippocampi (n=80) using all features of the feature vectors (described in Methods) but one. Using Dice index and paired t-test, each segmentation result was compared with the result when all features were included.

e. Comparison with volume-based single- and multi-template approaches

We obtained hippocampal segmentation using a volume-based single-template approach (FreeSurfer, (Fischl et al., 2002)), and a multi-template approach (Collins and Pruessner, 2010), henceforth named VolMulti. For VolMulti, we used ANIMAL as the non-linear registration method (Collins et al., 1994) and chose optimal subset of 11 templates as suggested by (Collins and Pruessner, 2010). For SurfMulti, an optimal subset of 10 templates produced the best segmentation accuracy.

For each automated algorithm, we compared Dice indices between patient groups (*i.e.* LTLE and RTLE) and controls using Student's t-tests.

In a separate analysis, we assessed the sensitivity of each algorithm to detect atrophy in TLE relative to controls by computing Cohen's d (mean volume controls – mean volume TLE) / pooled SD), a measure that indicates the effect size of a between-group difference.

We computed the significance of the observed effect using t-tests.

Significances of all statistical tests were adjusted for multiple comparisons using Bonferroni-correction.

f. Surface-based analysis of contour accuracy

To assess potential systematic shape bias between methods, automated segmentations produced by FreeSurfer and VolMulti were converted to surface meshes and parameterized using SPHARM-PDM (Styner et al., 2006) as described above. This process allowed shape-inherent vertex-wise correspondence across subjects and methods, thus enabling consistent comparison with the final segmentation returned by SurfMulti.

For each algorithm, after pooling controls and patients, we computed the normal component of the displacement vector between the automated and manual label at each vertex and then employed vertex-wise t-tests on the differences (Morey et al., 2009). In addition, we mapped the standard deviation (SD) of the displacement vector at each vertex. Differences in SD between automated segmentations were assessed using F-tests. Significances were thresholded at a false discovery rate of $FDR < 0.05$ (Benjamini and Hochberg, 1995).

g. Performance evaluation with respect to hippocampal atrophy and malrotation

The most representative indicators of hippocampal malrotation are medial positioning, vertical orientation, and increased depth of the collateral sulcus (Baulac et al., 1998; Bernasconi et al., 2005a). To quantify these characteristics, we created 3D metrics of the left and right hippocampi in each subject (Voets et al., 2011) from manual labels to determine: (i) sagittal translation, measuring the position of the hippocampus relative to the midline was calculated as millimeter distance between the geometric centre of the hippocampus and the mid-sagittal plane of the brain; (ii) axial rotation, reflecting a medial-lateral deflection of the hippocampus relative to its geometric centre; and (iii) longitudinal rotation, indicating a relative vertical deviation of the entire hippocampus from its normally horizontal orientation. Axial rotation and longitudinal rotation were measured in angles of deviation from the orientation of a reference average hippocampus, which was manually segmented on the ICBM-152 template. (iv) Collateral sulcus depth, representing the shortest distance in mm between the sulcal bottom point and the outer cortical surface, computed using Chamfer's transform (Borgefors, 1986). Each measurement was normalized through a z-transformation relative to the corresponding distribution of controls. In our controls and patients, prevalence of malrotation features that were greater than $z=2$ are shown in Table 5.1.

We used linear models to investigate the effect of hippocampal atrophy and malrotation on the performance of the automated methods.

Table 5.1. Prevalence of hippocampal malrotation in healthy controls and patients. Values were standardized relative to healthy controls distribution using the z-score transformation.

	Sagittal translation		Axial rotation		Longitudinal rotation		Collateral sulcus depth	
	Left	Right	Left	Right	Left	Right	Left	Right
Controls (n=35)	1 (3%)	1 (3%)	2 (3%)	1 (3%)	1 (6%)	1 (3%)	2 (6%)	1 (3%)
LTLE (n=73)	10 (29%)	2 (6%)	9 (26%)	3 (9%)	8 (23%)	1 (3%)	12 (34%)	3 (9%)
RTLE (n=71)	7 (23%)	9 (29%)	6 (19%)	2 (6%)	1 (3%)	5 (16%)	11 (35%)	6 (19%)

LTLE/RTLE: left/right temporal lobe epilepsy

Results

a. Volume-based assessment of segmentation accuracy

The adaptive template selection approach outperformed the traditional strategy (all groups: $p < 0.02$, **Table 5.2**). We therefore took as reference the adaptive approach for the following experiments.

Table 5.2. Segmentation accuracy as defined by Dice index (% mean \pm SD).

Group	FreeSurfer	VolMulti	SurfMulti	
			Equal weight	Advance adaptive weight
Controls	72.1 \pm 2.5	84.5 \pm 4.5	86.4 \pm 3.2	87.5 \pm 2.6
Ipsilateral	65.8 \pm 4.5	81.2 \pm 5.7	84.5 \pm 3.3	86.1 \pm 2.9
Contralateral	70.0 \pm 3.7	82.7 \pm 5.5	86.6 \pm 3.5	87.7 \pm 2.7

Ipsilateral and contralateral refer to the hemisphere of the seizure focus

b. Evaluation of feature contribution

Results are shown in **Figure 5.2**. Removing texture features dropped minimally ($p > 0.1$) the accuracy compared to the segmentation using all features.

Conversely, excluding shape constraints deteriorated significantly the performance of SurfMulti (Dice=82.4±5.1 vs. 87.1±2.8; $p<0.0001$).

c. Comparison with volume-based single- and multi-template approaches

In all groups, performance of SurfMulti (Dice=87.3±2.7) was superior to the two volume-based approaches (vs. FreeSurfer: 68.8±3.8, $p<10e-15$; vs. VolMulti: 82.5±5.4, $p<0.0004$, **Table 5.2**). Moreover, our algorithm performed equally well in TLE patients and controls ($p>0.1$), whereas volume-based approaches segmented poorly hippocampi in patients (FreeSurfer: $p<10e-6$; VolMulti: $p=0.02$).

Group-wise comparisons identified hippocampal atrophy ipsilateral to the seizure focus in TLE patients irrespective of the method, *i.e.*, manual or automated ($p<0.05$, **Table 5.3**). However, the effect size of atrophy detected using SurfMulti was the closest to manual labeling (Cohen's *d*: Manual=1.71, $t=7.6$; SurfMulti=1.60, $t=7.0$; VolMulti=1.38, $t=6.1$; FreeSurfer=0.91, $t=3.9$).

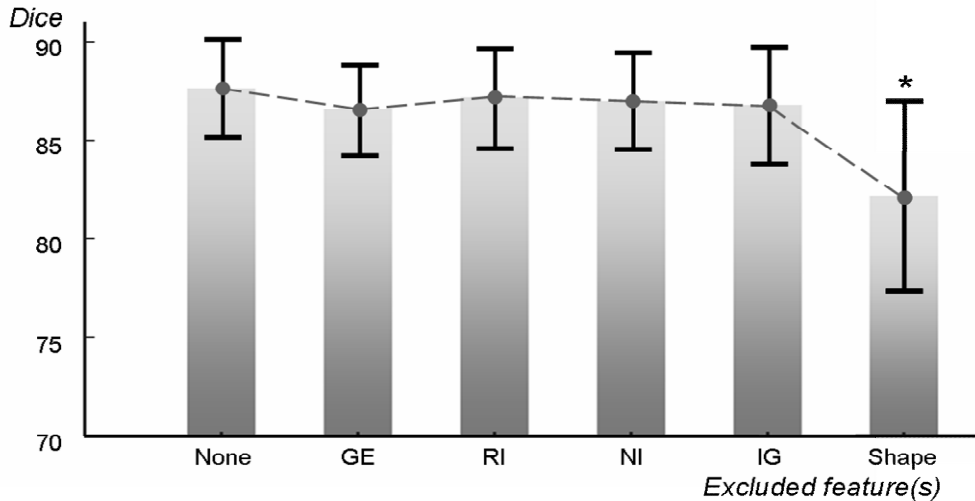


Figure 5.2. Contribution of texture and shape features to SurfMulti segmentation performance. Bars and whiskers present mean and standard deviation for each test. Abbreviations: GE=Gabor energy, RI=relative intensity, NI=normalized intensity, IG=intensity gradient, Shape=shape constraint features. Dice=Dice similarity index.

Table 5.3. Hippocampal volumetry. Values represent z-scores with respect to controls (mean±SD) and the effect size of atrophy as Cohen's d (within parentheses; 0.2 indicates a small effect, 0.5 a medium effect, and >0.8 is a large effect).

	Manual	FreeSurfer	VolMulti	SurfMulti
Ipsilateral	-2.41±1.85 (1.71)	-1.35±2.06 (0.91)	-1.49±1.40 (1.38)	-1.78±1.45 (1.60)
Contralateral	-0.65±1.40 (0.56)	-0.05±1.91 (0.03)	-0.22±1.29 (0.22)	-0.57±1.41 (0.47)

Ipsilateral and contralateral refer to the hemisphere of the seizure focus

d. Surface-based shape analysis of segmentations

Shape differences between manual tracing and automated methods are shown in **Figure 5.3**. Individual segmentation results are also illustrated in **Figure 5.4**. Among the three methods, segmentation using SurfMulti was most similar to manual labeling, with only sub-millimetric differences (mean error: 0.6mm±0.4, FDR<0.05) mainly at the lateral border. VolMulti showed overall increased mean and SD of shape displacements with respect to manual labels (absolute mean error: 1.2±1.0 mm, FDR<0.05). In addition to overestimating the lateral border (mean error: 0.9±1.1 mm, FDR<0.05), VolMulti underestimated a large area in superior and infero-medial surface (mean error: -1.3mm±0.9 mm, FDR<0.01). In contrast to the other two methods, FreeSurfer globally overestimated the volume (mean error: 1.7mm±2.1, FDR<0.05) and showed increased SD of the displacement vectors (vs. SurfMulti: p<0.00001; vs. VolMulti: p=0.002).

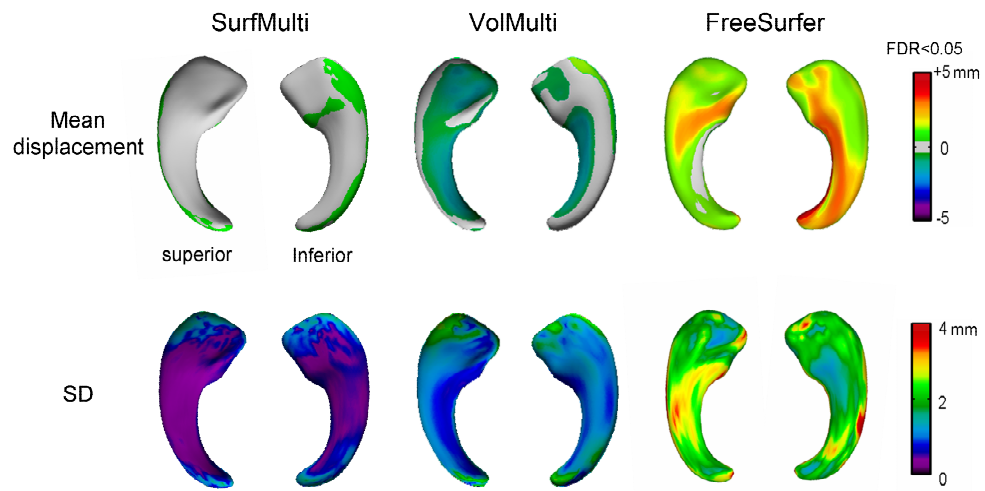


Figure 5.3. Shape analysis of automated segmentation algorithms. Vertex-wise maps of mean displacement and standard deviation averaged across all subjects.

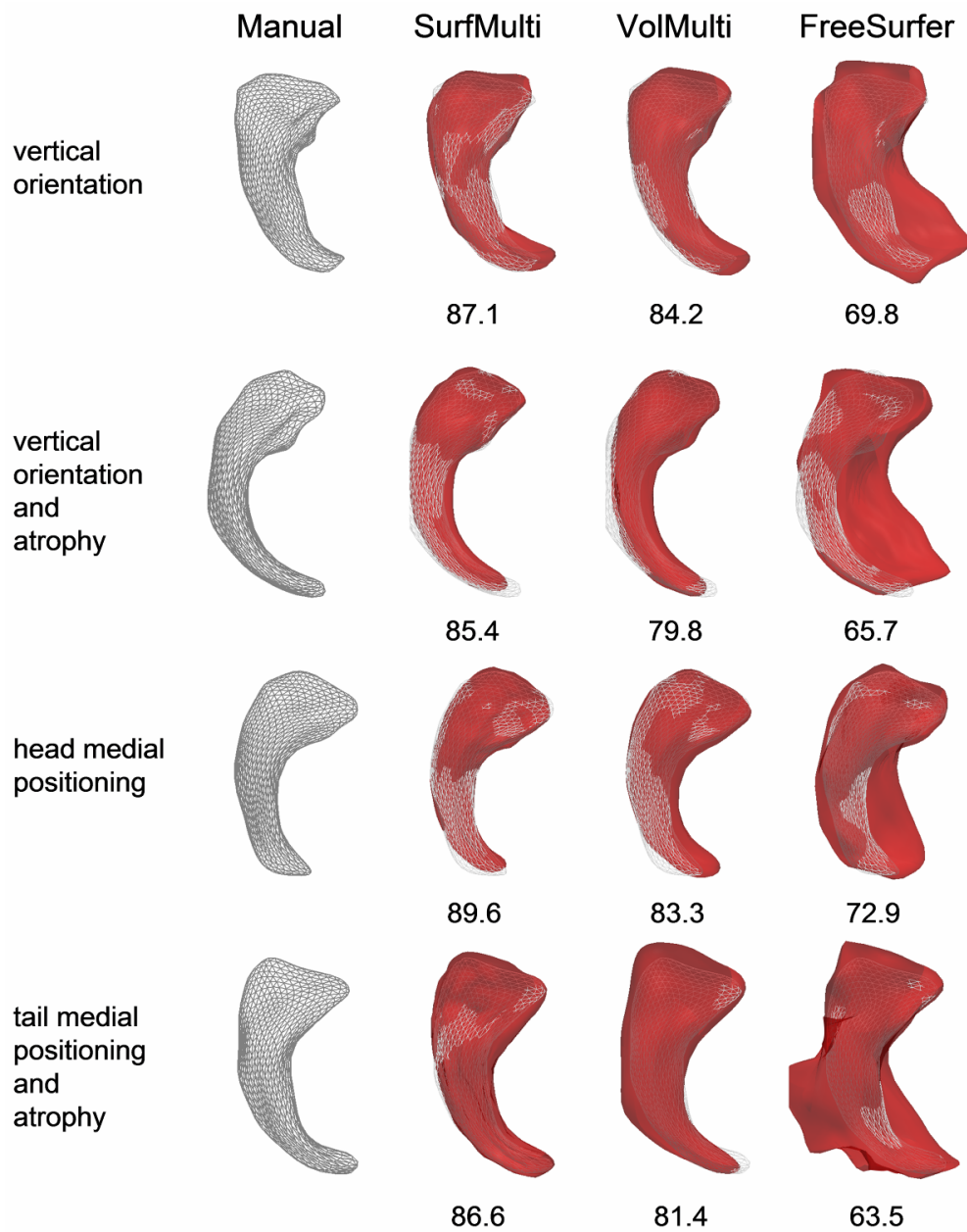


Figure 5.4. Representative examples of the automated segmentation algorithms. Each row presents automated segmentations (in red) overlapped with manual labels (wireframe) in case of shape anomalies associated with hippocampal malrotation and atrophy. The Dice index (in %) is indicated below each method.

e. *Impact of malrotation and hippocampal atrophy upon segmentation accuracy*

Results are shown in **Table 5.4**. While the Dice index of SurfMulti did not correlate with variations in hippocampal volume or malrotation features in any group ($|r| < 0.20$, $FDR > 0.2$), the segmentation accuracy of VolMulti was influenced by the axial rotation in all groups ($|r| > 0.28$, $FDR < 0.05$). For FreeSurfer, the Dice index in controls was positively correlated with hippocampal volume ($r = 0.55$, $p < 0.001$). Conversely, in TLE patients, the Dice index was influenced bilaterally by both atrophy ($r > 0.77$, $p < 0.0001$) and longitudinal rotation ($|r| > 0.55$; $p < 0.001$) and ipsilaterally by collateral sulcus depth ($|r| = 0.42$, $p = 0.002$). Interaction analysis however, showed that atrophy had a larger effect on the Dice than malrotation ($t > 5.4$ $FDR < 0.00001$).

Table 5.4. Association between automatic segmentation accuracy (as determined by Dice index) and hippocampal volume / malrotation features.

	Volume	Sagittal translation	Axial rotation	Longitudinal rotation	Collateral sulcus depth
SurfMulti					
Controls	-0.03	0.02	0.02	0.13	-0.20
Ipsilateral	0.16	0.03	-0.10	-0.19	-0.02
Contralateral	0.03	-0.07	0.15	-0.03	-0.11
VolMulti					
Controls	-0.17	0.27	-0.30	0.11	0.05
Ipsilateral	-0.12	-0.10	-0.35	-0.05	-0.04
Contralateral	0.24	-0.25	-0.28	-0.26	0.03
FreeSurfer					
Controls	0.55	-0.25	-0.04	0.06	-0.05
Ipsilateral	0.78	0.35	-0.07	-0.55	-0.42
Contralateral	0.77	-0.13	-0.03	-0.59	-0.13

Significances (in bold) are thresholded at $p < 0.05$ after Bonferroni correction for $|r| > 0.28$. Ipsilateral and contralateral refer to the hemisphere of the seizure focus.

Discussion

We proposed a novel hippocampal segmentation algorithm that integrates deformable parametric surfaces and multiple templates in a unified framework. Our technique achieved a level of accuracy in TLE patients virtually identical to healthy controls with a Dice index of 86.1% for the hippocampus ipsilateral to the seizure focus. To the best of our knowledge, such performance has not yet been paralleled in epilepsy populations. Vertex-wise shape mapping showed that SurfMulti with adaptive weight had an excellent overlap with manual labels, with sub-millimetric precision.

While the volume-based single- and multi-template approaches showed poorer performance in the presence of hippocampal malrotation and atrophy, SurfMulti was not influenced by either of these anomalies. Furthermore, our segmentation achieved the same sensitivity as manual volumetry in detecting atrophy ipsilateral to the seizure focus. Given that volumetry is superior to conventional MRI to detect hippocampal atrophy, our automated algorithm may constitute a robust surrogate tool for the time-demanding manual procedure in the presurgical evaluation.

To segment brain structures, multi-template algorithms use either mutual information (Collins and Pruessner, 2010) or entropy (Aljabar et al., 2009) as a measure of similarity between the target and the template. In these methods, if intensity distributions of the two images are different, segmentation may fail. Our features, on the contrary, capture intrinsic image characteristics by computing higher order semantic features from a given image, i.e. image homogeneity, contrast, gradient and texture. Moreover, they are weighted according to both mean and SD of the optimal subset. Our experiments demonstrated that the removal of any single texture feature did not weaken the performance of SurfMulti. The reduced performance when excluding shape features on the other

hand highlights the importance of such constraints, suggesting their capability to regulate the range of deformations within anatomical variabilities.

Our results showed that hippocampal malrotation influenced significantly the performance of state-of-the-art volume-based approaches we evaluated. Malrotation not only alter the shape of the hippocampus but also deforms its neighboring structures, potentially hampering their modeling. To capture anatomical variability, we created vertex-wise spherical neighborhoods and sampled separately inner and outer regions of structures that are within several millimeters of the hippocampal boundary. Multi-template approaches offer a suitable framework to account for structural variability by selecting from a database a subset that best describe anatomical characteristics of the target structure. To date, these techniques have been volume-based and applied to segment healthy hippocampi (Aljabar et al., 2009; Collins and Pruessner, 2010). However, they rely on non-linear image registration, which may also fail in case of atypical morphology.

To date template libraries (Aljabar et al., 2009; Collins and Pruessner, 2010; Hammers et al., 2007) have been constructed based on volume labels of healthy hippocampi where malrotation features are less prevalent. We believe that the good performance we obtained in both healthy and diseased populations results from the integration of surface-based shape-inherent point-wise correspondences guaranteed by SPHARM-PDM and our vertex-wise sampling scheme with respect to the surface boundary, allowing for a better characterization of locoregional texture and shape of structures neighboring the hippocampus. Finally, our multi-template library derived from a large cohort of healthy controls and patients accounts for inter-subject variability, in particular shape variants. Aside TLE, hippocampal atrophy and developmental anomalies occur in epilepsy related to malformation of cortical development (Baulac et al., 1998; Bernasconi et al., 2005a; Montenegro et al., 2006; Sato et al., 2001) and a variety of other neurological and neuropsychiatric disorders such as

schizophrenia (Connor et al., 2004; Narr et al., 2004; Pegues et al., 2003; Whitworth et al., 1998) and autism (Nicolson et al., 2006; Salmond et al., 2005). The influence of these abnormalities to a broad range of disorders emphasizes the consideration of atypical anatomical characteristics when designing automated segmentation methods.

Chapter 6

Summary and Conclusions

This dissertation portrays the development of a series of surface-based morphometric techniques and their clinical usefulness in assessing mesiotemporal shape variants in patients with pharmacologically intractable temporal lobe epilepsy (TLE).

The overall goal was to develop advanced morphometric methods to statistically model characteristics of pathology that have not been previously evaluated on MRI and that are not evident in measurement of total volume or in the visual assessment. To achieve this aim, we proposed a comprehensive surface-based analysis that independently assesses volumes and positions of the mesiotemporal structures and patterns of morphological changes occurring in the collateral sulcus. We minimized the human intervention in this procedure by designing an automated hippocampal tracing method that can segment shape variants almost as accurately as manual labelling.

Manuscript 1 described a design of a unified surface-based framework to analyze independently volume and position. In this framework, vertex-wise Jacobian

determinants were computed to quantify local volume variations. In addition, a medial axis model inheriting the shape-constrained point correspondence of SPHARM-PDM was constructed to quantify fine-scale local position and curvature. On synthetic shapes, our method unambiguously disentangled local volume from positional changes by quantifying independently both morphological characteristics. In TLE patients, atrophy and positional changes co-occurred at the level of the posterior hippocampus. Hippocampal malpositioning is believed to be a marker of neurodevelopmental deviance occurring during early phases of gestation. Disentangling volume from positioning may provide new insights in a variety of other neurological conditions in which these morphological anomalies coexist and neurodevelopmental abnormalities have been modeled as a potential underlying pathogenic mechanism.

In Manuscript 2, we assessed local volume changes in mesiotemporal structures using the surface-based Jacobian determinant developed in Manuscript 1. Our findings of atrophy preferentially affecting specific subfields emphasize the ability of post-processing of anatomical MRI to unveil anomalies not otherwise detected on visual evaluation or whole-structure volumetric analysis. In addition to atrophy, likely related to neuronal damage, we found hypertrophy in bilateral dentate gyrus as well as in the amygdala. Our results, in line with histopathological reports and experimental models, provide compelling evidence of aberrant seizure-related plasticity in TLE.

In Manuscript 3, analysis of basal temporal sulcal morphology revealed that the majority of TLE patients exhibit a single-branch, unbroken long collateral sulcus as compared to healthy controls. Given that developmental malformations are clearly present before the onset of epilepsy and often associated with intractable epilepsy, this “simplified” sulcal arrangement may be a biological marker of altered corticogenesis and predispose the temporal lobe to be vulnerable to injuries during early gestation.

In Manuscript 4, we assessed the influence of morphological anomalies on the performance of automated segmentation algorithms. We found that SACHA overestimated the volume of the lateral convexity of the hippocampus in cases with malrotation, but behaved relatively well in the presence of atrophy. The performance of FreeSurfer, on the other hand, was affected by both hippocampal malrotation and atrophy. The automated procedures detected smaller effect sizes of hippocampal atrophy and tended to be less accurate for seizure focus lateralization compared to manual volumetry. Sub-optimal performance of automated methods in the presence of malrotation implied atypical morphologies to be taken into account when designing segmentation algorithms.

Manuscript 5 presented a novel automatic hippocampal segmentation method combining deformable parametric surfaces and multiple templates in a unified framework. Our technique achieved a level of accuracy in TLE patients virtually identical to healthy controls, with a Dice index of 86.1%, a performance that has not yet been matched in epilepsy. Vertex-wise surface-based shape mapping showed that SurfMulti with adaptive weighting had an excellent agreement with manual labels. Furthermore, we achieved the same sensitivity as manual volumetry in detecting atrophy. The proposed automated algorithm promises to be a robust surrogate tool for the time-demanding manual procedure.

The significance of this thesis lies in the detection of aspects of pathology that have not been previously assessed using conventional MRI analyses. This was accomplished by the developed surface-based morphometric framework which statistically analyzes subtle and local morphological variations. Furthermore, it can prove useful in surgical target localization and post-surgical outcome prediction, the two main challenges of contemporary epilepsy surgery affecting 100,000 patients across Canada. Given that mesiotemporal morphological alterations are related to various neurological and neuropsychological disorders (Ballmaier et al., 2008; Burton et al., 2009; Ehrlich et al., 2010; Ho and Magnotta, 2010; Nicolson et al., 2006), the proposed morphometric framework may be of diagnostic value. Finally, the developed methodology and techniques that

enhance a universal surface model and model generic texture and shape features can be extended to the analysis of a variety of subcortical structures, such as the amygdala, the caudate, the thalamus and the ventricles.

메모 [h1]: corrected

Bibliography

Akhondi-Asl, A., Jafari-Khouzani, K., Elisevich, K., Soltanian-Zadeh, H., 2011. Hippocampal volumetry for lateralization of temporal lobe epilepsy: Automated versus manual methods. *Neuroimage* 54, S218-S226.

Aljabar, P., Heckemann, R.A., Hammers, A., Hajnal, J.V., Rueckert, D., 2009. Multi-atlas based segmentation of brain images: Atlas selection and its effect on accuracy. *Neuroimage* 46, 726-738.

Amunts, K., Kedo, O., Kindler, M., Pieperhoff, P., Mohlberg, H., Shah, N.J., Habel, U., Schneider, F., Zilles, K., 2005. Cytoarchitectonic mapping of the human amygdala, hippocampal region and entorhinal cortex: intersubject variability and probability maps. *Anat Embryol (Berl)* 210, 343-352.

Antel, S.B., Bernasconi, A., Bernasconi, N., Collins, D.L., Kearney, R.E., Shinghal, R., Arnold, D.L., 2002a. Computational models of MRI characteristics of focal cortical dysplasia improve lesion detection. *Neuroimage* 17, 1755-1760.

Antel, S.B., Li, L.M., Cendes, F., Collins, D.L., Kearney, R.E., Shinghal, R., Arnold, D.L., 2002b. Predicting surgical outcome in temporal lobe epilepsy patients using MRI and MRSI. *Neurology* 58, 1505-1512.

Armstrong, E., Curtis, M., Buxhoeveden, D.P., Fregoe, C., Zilles, K., Casanova, M.F., McCarthy, W.F., 1991. Cortical gyrification in the rhesus monkey: a test of the mechanical folding hypothesis. *Cereb Cortex* 1, 426-432.

Arruda, F., Cendes, F., Andermann, F., Dubeau, F., Villemeure, J.G., Jones-Gotman, M., Poulin, N., Arnold, D.L., Olivier, A., 1996. Mesial atrophy and outcome after amygdalohippocampectomy or temporal lobe removal. *Ann Neurol* 40, 446-450.

Ashburner, J., Friston, K.J., 1999. Nonlinear spatial normalization using basis functions. *Human Brain Mapping* 7, 254-266.

Ashburner, J., Friston, K.J., 2000. Voxel-based morphometry--the methods. *Neuroimage* 11, 805-821.

Ashburner, J., Friston, K.J., 2001. Why voxel-based morphometry should be used. *Neuroimage* 14, 1238-1243.

Ashburner, J., Hutton, C., Frackowiak, R., Johnsrude, I., Price, C., Friston, K., 1998a. Identifying global anatomical differences: Deformation-based morphometry. *Human Brain Mapping* 6, 348-357.

Ashburner, J., Hutton, C., Frackowiak, R., Johnsrude, I., Price, C., Friston, K., 1998b. Identifying global anatomical differences: deformation-based morphometry. *Hum Brain Mapp* 6, 348-357.

Avants, B.B., Yushkevich, P., Pluta, J., Minkoff, D., Korczykowski, M., Detre, J., Gee, J.C., 2010. The optimal template effect in hippocampus studies of diseased populations. *Neuroimage* 49, 2457-2466.

Babb, T.L., Brown, W.J., 1987. Pathological findings in epilepsy. In: Engel, J., Jr. (Ed.), *Surgical treatment of the epilepsies*. Raven, New York, NY, pp. 511-540.

Babb, T.L., Brown, W.J., Pretorius, J., Davenport, C., Lieb, J.P., Crandall, P.H., 1984. Temporal lobe volumetric cell densities in temporal lobe epilepsy. *Epilepsia* 25, 729-740.

Bailey, P., Von Bonin, G., 1951. *The isocortex of Man*. University of Illinois Press, Urbana.

Bajcsy, R., Lieberman, R., Reivich, M., 1983. A computerized system for the elastic matching of deformed radio-graphic images to idealized atlas images.

Bajic, D., Wang, C., Kumlien, E., Mattsson, P., Lundberg, S., Eeg-Olofsson, O., Raininko, R., 2008. Incomplete inversion of the hippocampus—a common developmental anomaly. *European Radiology* 18, 138-142.

Ballmaier, M., Narr, K.L., Toga, A.W., Elderkin-Thompson, V., Thompson, P.M., Hamilton, L., Haroon, E., Pham, D., Heinz, A., Kumar, A., 2008. Hippocampal morphology and distinguishing late-onset from early-onset elderly depression. *Am J Psychiatry* 165, 229-237.

Barnes, J., Foster, J., Boyes, R.G., Pepple, T., Moore, E.K., Schott, J.M., Frost, C., Scahill, R.I., Fox, N.C., 2008. A comparison of methods for the automated calculation of volumes and atrophy rates in the hippocampus. *Neuroimage* 40, 1655-1671.

Barsi, P., Kenez, J., Solymosi, D., Kulin, A., Halasz, P., Rasonyi, G., Janszky, J., Kaloczkai, A., Barcs, G., Neuwirth, M., Paraicz, E., Siegler, Z., Morvai, M., Jerney, J., Kassay, M., Altmann, A., 2000a. Hippocampal malrotation with normal corpus callosum: a new entity? *Neuroradiology* 42, 339-345.

Barsi, P., Kenez, J., Solymosi, D., Kulin, A., Halasz, P., Rasonyi, G., Janszky, J., Kaloczkai, A., Barcs, G., Neuwirth, M., Paraicz, E., Siegler, Z., Morvai, M., Jerney, J., Kassay, M., Altmann, A., 2000b. Hippocampal malrotation with normal corpus callosum: a new entity? , *Neuroradiology*, pp. 339-345.

Bartley, A.J., Jones, D.W., Weinberger, D.R., 1997. Genetic variability of human brain size and cortical gyral patterns. *Brain* 120, 257-269.

Bartolomei, F., Khalil, M., Wendling, F., Sontheimer, A., Regis, J., Ranjeva, J.P., Guye, M., Chauvel, P., 2005. Entorhinal cortex involvement in human mesial temporal lobe epilepsy: an electrophysiologic and volumetric study. *Epilepsia* 46, 677-687.

Bartolomei, F., Wendling, F., Bellanger, J.J., Regis, J., Chauvel, P., 2001. Neural networks involving the medial temporal structures in temporal lobe epilepsy. *Clin Neurophysiol* 112, 1746-1760.

Bartrez-Faz, D., Riviere, D., Le Provost, J.B., Artiges, E., Mangin, J.F., Paillere, F., Leboyer, M., Gallarda, T., Recasens, C., Martinot, J.L., 2002. Automatic recognition of cerebral sulci in schizophrenia using a congregation of neural networks. *European Neuropsychopharmacology*, pp. 330-331.

Baulac, M., De Grissac, N., Hasboun, D., Oppenheim, C., Adam, C., Arzimanoglou, A., Semah, F., Lehericy, S., Clemenceau, S., Berger, B., 1998. Hippocampal developmental changes in patients with partial epilepsy: magnetic resonance imaging and clinical aspects. *Ann.Neurol.* 44, 223-233.

Bell, B.D., Giovagnoli, A.R., 2007. Recent innovative studies of memory in temporal lobe epilepsy. *Neuropsychol Rev* 17, 455-476.

Benjamini, Y., Hochberg, Y., 1995. Controlling the false discovery rate: a practical and powerful approach to multiple testing. *J Royal Stat Soc* 57, 289-300.

Berkovic, S.F., Andermann, F., Olivier, A., Ethier, R., Melanson, D., Robitaille, Y., Kuzniecky, R., Peters, T., Feindel, W., 1991. Hippocampal sclerosis in temporal lobe epilepsy demonstrated by magnetic resonance imaging. *Ann Neurol* 29, 175-182.

Berkovic, S.F., McIntosh, A., Kalnins, R., Jackson, G.D., Fabinyi, G.C.A., Branzenor, G.A., Bladin, P.F., Hopper, J.L., 1995. Preoperative MRI predicts outcome of temporal lobectomy: an actuarial analysis. *Neurology* 45, 1358-1363.

Bernasconi, A., 2006. Magnetic resonance imaging in intractable epilepsy: focus on structural image analysis. *Adv Neurol* 97, 273-278.

Bernasconi, N., Andermann, F., Arnold, D.L., Bernasconi, A., 2003a. Entorhinal cortex MRI assessment in temporal, extratemporal, and idiopathic generalized epilepsy. *Epilepsia* 44, 1070-1074.

Bernasconi, N., Bernasconi, A., Andermann, F., Dubeau, F., Feindel, W., Reutens, D.C., 1999. Entorhinal cortex in temporal lobe epilepsy: a quantitative MRI study. *Neurology* 52, 1870-1876.

Bernasconi, N., Bernasconi, A., Caramanos, Z., Andermann, F., Dubeau, F., Arnold, D.L., 2000. Morphometric MRI analysis of the parahippocampal region in temporal lobe epilepsy. *Ann.N.Y.Acad Sci.* 911, 495-500.

Bernasconi, N., Bernasconi, A., Caramanos, Z., Antel, S.B., Andermann, F., Arnold, D.L., 2003b. Mesial temporal damage in temporal lobe epilepsy: a volumetric MRI study of the hippocampus, amygdala and parahippocampal region. *Brain* 126, 462-469.

Bernasconi, N., Bernasconi, A., Caramanos, Z., Dubeau, F., Richardson, J., Andermann, F., Arnold, D.L., 2001. Entorhinal cortex atrophy in epilepsy patients exhibiting normal hippocampal volumes. *Neurology* 56, 1335-1339.

Bernasconi, N., Khalili, N., Colliot, O., Elfassy, Y., Antel, S., Andermann, F., Bernasconi, A., 2004. Voxel-based analysis of gray matter in focal cortical dysplasia. *Epilepsia* 45, 366.

Bernasconi, N., Kinay, D., Andermann, F., Antel, S., Bernasconi, A., 2005a. Analysis of shape and positioning of the hippocampal formation: an MRI study in patients with partial epilepsy and healthy controls. *Brain* 128, 2442-2452.

Bernasconi, N., Natsume, J., Bernasconi, A., 2005b. Progression in temporal lobe epilepsy: differential atrophy in mesial temporal structures. *Neurology* 65, 223-228.

Bernhardt, B.C., Bernasconi, N., Concha, L., Bernasconi, A., 2010. Cortical thickness analysis in temporal lobe epilepsy: reproducibility and relation to outcome. *Neurology* 74, 1776-1784.

Bernhardt, B.C., Worsley, K.J., Kim, H., Evans, A.C., Bernasconi, A., Bernasconi, N., 2009. Longitudinal and cross-sectional analysis of atrophy in pharmaco-resistant temporal lobe epilepsy. *Neurology* 72, 1747-1754.

Bernier, P.J., Bedard, A., Vinet, J., Levesque, M., Parent, A., 2002. Newly generated neurons in the amygdala and adjoining cortex of adult primates. *Proc Natl Acad Sci U S A* 99, 11464-11469.

Bertram, E.H., Zhang, D.X., Mangan, P., Fountain, N., Rempe, D., 1998. Functional anatomy of limbic epilepsy: a proposal for central synchronization of a diffusely hyperexcitable network. *Epilepsy Res* 32, 194-205.

Binder, D.K., Steinhauser, C., 2006. Functional changes in astroglial cells in epilepsy. *Glia* 54, 358-368.

Blümcke, I., Pauli, E., Clusmann, H., Schramm, J., Becker, A., Elger, C., Merschhemke, M., Meencke, H.-J., Lehmann, T., von Deimling, A., Scheiwe, C., Zentner, J., Volk, B., Romstöck, J., Stefan, H., Hildebrandt, M., 2007. A new clinico-pathological classification system for mesial temporal sclerosis. *Acta Neuropathologica* 113, 235-244.

Blanton, R.E., Levitt, J.G., Thompson, P.M., Narr, K.L., Capetillo-Cunliffe, L., Nobel, A., Singerman, J.D., McCracken, J.T., Toga, A.W., 2001. Mapping cortical asymmetry and complexity patterns in normal children. *Psychiatry Res* 107, 29-43.

Blumcke, I., Thom, M., Wiestler, O.D., 2002. Ammon's horn sclerosis: a maldevelopmental disorder associated with temporal lobe epilepsy. *Brain Pathol* 12, 199-211.

Bonilha, L., Kobayashi, E., Rorden, C., Cendes, F., Li, L.M., 2003. Medial temporal lobe atrophy in patients with refractory temporal lobe epilepsy. *J Neurol Neurosurg Psychiatry* 74, 1627-1630.

Bonilha, L., Rorden, C., Appenzeller, S., Coan, A.C., Cendes, F., Li, L.M., 2006. Gray matter atrophy associated with duration of temporal lobe epilepsy. *Neuroimage* 32, 1070-1079.

- Bookstein, F.L., 1997. Landmark methods for forms without landmarks: morphometrics of group differences in outline shape. *Med Image Anal* 1, 225-243.
- Borgefors, G., 1986. Distance transformations in digital images. *Comp Vision Graph Im Proc* 34, 344-371.
- Bouix, S., Pruessner, J.C., Louis Collins, D., Siddiqi, K., 2005. Hippocampal shape analysis using medial surfaces. *Neuroimage* 25, 1077-1089.
- Braak, H., Braak, E., 1992. The human entorhinal cortex: normal morphology and lamina-specific pathology in various diseases. [Review]. *Neurosci Res* 15, 6-31.
- Brambati, S.M., Rankin, K.P., Narvid, J., Seeley, W.W., Dean, D., Rosen, H.J., Miller, B.L., Ashburner, J., Gorno-Tempini, M.L., 2009. Atrophy progression in semantic dementia with asymmetric temporal involvement: A tensor-based morphometry study. *Neurobiology of Aging* 30, 103-111.
- Brambati, S.M., Renda, N.C., Rankin, K.P., Rosen, H.J., Seeley, W.W., Ashburner, J., Weiner, M.W., Miller, B.L., Gorno-Tempini, M.L., 2007. A tensor based morphometry study of longitudinal gray matter contraction in FTD. *Neuroimage* 35, 998-1003.
- Bronen, R.A., Spencer, D.D., Fulbright, R.K., 2000. Cerebrospinal fluid cleft with cortical dimple: MR imaging marker for focal cortical dysgenesis. *Radiology* 214, 657-663.
- Bruton, C.J., 1988. *The neuropathology of temporal lobe epilepsy*. Oxford University Press, New York, NY.
- Burton, E.J., Barber, R., Mukaetova-Ladinska, E.B., Robson, J., Perry, R.H., Jaros, E., Kalaria, R.N., O'Brien, J.T., 2009. Medial temporal lobe atrophy on MRI differentiates Alzheimer's disease from dementia with Lewy bodies and vascular cognitive impairment: a prospective study with pathological verification of diagnosis. *Brain* 132, 195-203.

Cachier, P., Mangin, J.-F., Pennec, X., Rivière, D., Papadopoulos-Orfanos, D., Régis, J., Ayache, N., 2001. Multisubject non-rigid registration of brain MRI using intensity and geometric features. *Medical Image Computing and Computer-Assisted Intervention – MICCAI 2001*, pp. 734-742.

Cardenas, V.A., Studholme, C., Gazdzinski, S., Durazzo, T.C., Meyerhoff, D.J., 2007. Deformation-based morphometry of brain changes in alcohol dependence and abstinence. *Neuroimage* 34, 879-887.

Cardoso, M.J., Clarkson, M.J., Ridgway, G.R., Modat, M., Fox, N.C., Ourselin, S., 2011. LoAd: A locally adaptive cortical segmentation algorithm. *Neuroimage* 56, 1386-1397.

Carmichael, O.T., Aizenstein, H.A., Davis, S.W., Becker, J.T., Thompson, P.M., Meltzer, C.C., Liu, Y., 2005. Atlas-based hippocampus segmentation in Alzheimer's disease and mild cognitive impairment. *Neuroimage* 27, 979-990.

Cascino, G.D., 2004. Surgical treatment for epilepsy. *Epilepsy Research* 60, 179-186.

Cascino, G.D., 2008. Neuroimaging in Epilepsy: Diagnostic Strategies in Partial Epilepsy. *Semin Neurol* 28, 523,532.

Cascino, G.D., Jack, C.R., Jr., Hirschorn, K.A., Sharbrough, F.W., 1992a. Identification of the epileptic focus: magnetic resonance imaging. [Review] [31 refs]. *Epilepsy Research - Supplement* 5, 95-100.

Cascino, G.D., Jack, C.R., Jr., Parisi, J.E., Marsh, W.R., Kelly, P.J., Sharbrough, F.W., Hirschorn, K.A., Trennery, M.R., 1992b. MRI in the presurgical evaluation of patients with frontal lobe epilepsy and children with temporal lobe epilepsy: pathologic correlation and prognostic importance. *Epilepsy Res* 11, 51-59.

Cascino, G.D., Jack, C.R., Jr., Parisi, J.E., Sharbrough, F.W., Hirschorn, K.A., Meyer, F.B., Marsh, W.R., O'Brien, P.C., 1991. Magnetic resonance imaging-

based volume studies in temporal lobe epilepsy: pathological correlations. *Ann Neurol* 30, 31-36.

Caselles, V., Kimmel, R., Sapiro, G., 1997. Geodesic active contours. *Int J Comput. Vis* 22, 61-79.

Caviness, V.S., Jr., 1975. Mechanical model of brain convolutional development. *Science* 189, 18-21.

Cendes, F., Andermann, F., Gloor, P., Evans, A., Jones-Gotman, M., Watson, C., Melanson, D., Olivier, A., Peters, T., Lopes-Cendes, I., Leroux, G., 1993a. MRI volumetric measurement of amygdala and hippocampus in temporal lobe epilepsy. *Neurology* 43, 719-725.

Cendes, F., Andermann, F., Gloor, P., Lopes-Cendes, I., Andermann, E., Melanson, D., Jones-Gotman, M., Robitaille, Y., Evans, A., Peters, T., 1993b. Atrophy of mesial structures in patients with temporal lobe epilepsy: cause or consequence of repeated seizures ? *Ann Neurol* 34, 795-801.

Cendes, F., Caramanos, Z., Andermann, F., Dubeau, F., Arnold, D.L., 1997. Proton magnetic resonance spectroscopic imaging and magnetic resonance imaging volumetry in the lateralization of temporal lobe epilepsy: a series of 100 patients. *Ann Neurol* 42, 737-746.

Chan, T.F., Vese, L.A., 2001. Active contours without edges. *Image Processing, IEEE Transactions on* 10, 266-277.

Chetelat, G., Desgranges, B., De La Sayette, V., Viader, F., Eustache, F., Baron, J.C., 2002. Mapping gray matter loss with voxel-based morphometry in mild cognitive impairment. *Neuroreport* 13, 1939-1943.

Chi, J.G., Dooling, E.C., Gilles, F.H., 1977. Gyral development of the human brain. *Ann Neurol* 1, 86-93.

Chung, M.K., Worsley, K.J., Paus, T., Cherif, C., Collins, D.L., Giedd, J.N., Rapoport, J.L., Evans, A.C., 2001a. A unified statistical approach to deformation-based morphometry. *Neuroimage* 14, 595-606.

Chung, M.K., Worsley, K.J., Taylor, J., Ramsay, J., Robbins, S., Evans, A.C., 2001b. Diffusion Smoothing on the Cortical Surface. *Neuroimage*.

Chupin, M., Gérardin, E., Cuingnet, R., Boutet, C., Lemieux, L., Lehericy, S., Benali, H., Garnero, L., Colliot, O., 2009a. Fully automatic hippocampus segmentation and classification in Alzheimer's disease and mild cognitive impairment applied on data from ADNI. *Hippocampus* 19, 579-587.

Chupin, M., Hammers, A., Liu, R.S., Colliot, O., Burdett, J., Bardinet, E., Duncan, J.S., Garnero, L., Lemieux, L., 2009b. Automatic segmentation of the hippocampus and the amygdala driven by hybrid constraints: Method and validation. *Neuroimage* 46.

Chupin, M., Mukuna-Bantumbakulu, A.R., Hasboun, D., Bardinet, E., Baillet, S., Kinkingnehun, S., Lemieux, L., Dubois, B., Garnero, L., 2007. Anatomically constrained region deformation for the automated segmentation of the hippocampus and the amygdala: Method and validation on controls and patients with Alzheimer's disease. *Neuroimage* 34, 996-1019.

Cohen-Gadol, A.A., Bradley, C.C., Williamson, A., Kim, J.H., Westerveld, M., Duckrow, R.B., Spencer, D.D., 2005. Normal magnetic resonance imaging and medial temporal lobe epilepsy: the clinical syndrome of paradoxical temporal lobe epilepsy. *J Neurosurg* 102, 902-909.

Cohen-Gadol, A.A., Wilhelmi, B.G., Collignon, F., White, J.B., Britton, J.W., Cambier, D.M., Christianson, T.J., Marsh, W.R., Meyer, F.B., Cascino, G.D., 2006. Long-term outcome of epilepsy surgery among 399 patients with nonlesional seizure foci including mesial temporal lobe sclerosis. *J Neurosurg* 104, 513-524.

Cohen, J., 1960. A coefficient of agreement for nominal scales. *Educational and Psychological Measurement* 20, 37-46.

Collins, D., Pruessner, J., 2009. Towards accurate, automatic segmentation of the hippocampus and amygdala from MRI. *Medical Image Computing and Computer-Assisted Intervention – MICCAI 2009*, pp. 592-600.

Collins, D.L., Holmes, C.J., Peters, T.M., Evans, A.C., 1995. Automatic 3-D model-based neuroanatomical segmentation. *Human Brain Mapping* 3, 190-208.

Collins, D.L., Neelin, P., Peters, T.M., Evans, A.C., 1994. Automatic 3D intersubject registration of MR volumetric data in standardized Talairach space. *J Comput Assist Tomogr* 18, 192-205.

Collins, D.L., Pruessner, J.C., 2010. Towards accurate, automatic segmentation of the hippocampus and amygdala from MRI by augmenting ANIMAL with a template library and label fusion. *Neuroimage* 52, 1355-1366.

Connor, S.E.J., Ng, V., McDonald, C., Schulze, K., Morgan, K., Dazzan, P., Murray, R.M., 2004. A study of hippocampal shape anomaly in schizophrenia and in families multiply affected by schizophrenia or bipolar disorder. *Neuroradiology* 46, 523-534.

Cootes, T.F., Edwards, G.J., Taylor, C.J., 2001. Active appearance models. *Pattern Analysis and Machine Intelligence, IEEE Transactions on* 23, 681-685.

Coupé, P., Manjón, J.V., Fonov, V., Pruessner, J., Robles, M., Collins, D.L., 2011. Patch-based segmentation using expert priors: Application to hippocampus and ventricle segmentation. *Neuroimage* 54, 940-954.

Crum, W.R., Scahill, R.I., Fox, N.C., 2001. Automated hippocampal segmentation by regional fluid registration of serial MRI: validation and application in Alzheimer's disease. *Neuroimage*. 13, 847-855.

Csernansky, J.G., Wang, L., Jones, D., Rastogi-Cruz, D., Posener, J.A., Heydebrand, G., Miller, J.P., Miller, M.I., 2002. Hippocampal deformities in

schizophrenia characterized by high dimensional brain mapping. *Am J Psychiatry* 159, 2000-2006.

Csernansky, J.G., Wang, L., Joshi, S., Miller, J.P., Gado, M., Kido, D., McKeel, D., Morris, J.C., Miller, M.I., 2000. Early DAT is distinguished from aging by high-dimensional mapping of the hippocampus. *Dementia of the Alzheimer type. Neurology* 55, 1636-1643.

de Lanerolle, N.C., Kim, J.H., Williamson, A., Spencer, S.S., Zaveri, H.P., Eid, T., Spencer, D.D., 2003. A Retrospective Analysis of Hippocampal Pathology in Human Temporal Lobe Epilepsy: Evidence for Distinctive Patient Subcategories. *Epilepsia* 44, 677-687.

Depondt, C., Van Paesschen, W., Matthijs, G., Legius, E., Martens, K., Demaerel, P., Wilms, G., 2002. Familial temporal lobe epilepsy with febrile seizures. *Neurology* 58, 1429-1433.

Dobbins, I.G., Kroll, N.E.A., Tulving, E., Knight, R.T., Gazzaniga, M.S., 1998. Unilateral medial temporal lobe memory impairment: type deficit, function deficit, or both ? *Neuropsychologia* 36, 115-127.

Du, F., Schwarcz, R., Tamminga, C.A., 1995. Entorhinal cortex in temporal lobe epilepsy. *Am J Psychiatry* 152, 6.

Du, F., Whetsell, W.O., Abou-Khalil, B., Blumenkopf, B., 1993. Preferential neuronal loss in layer III of the entorhinal cortex in patients with temporal lobe epilepsy. *Epilepsy Res* 16, 223-233.

Duchesne, S., Pruessner, J., Collins, D.L., 2002. Appearance-based segmentation of medial temporal lobe structures. *Neuroimage* 17, 515-531.

Dumoulin, S.O., Bittar, R.G., Kabani, N.J., Baker, C.L., Jr., Le Goualher, G., Bruce, P.G., Evans, A.C., 2000. A new anatomical landmark for reliable identification of human area V5/MT: a quantitative analysis of sulcal patterning. *Cereb.Cortex* 10, 454-463.

- Duncan, J.S., 1997. Imaging and epilepsy. *Brain* 120, 339-377.
- Dunteman, G.H., 1989. *Principal Components Analysis*. Sage Publications, Inc, London.
- Duvernoy, H.M., 2005. *The human hippocampus: an atlas of applied anatomy* 3ed. Springer Verlag, New York.
- Ehrlich, S., Morrow, E.M., Roffman, J.L., Wallace, S.R., Naylor, M., Bockholt, H.J., Lundquist, A., Yendiki, A., Ho, B.C., White, T., Manoach, D.S., Clark, V.P., Calhoun, V.D., Gollub, R.L., Holt, D.J., 2010. The COMT Val108/158Met polymorphism and medial temporal lobe volumetry in patients with schizophrenia and healthy adults. *Neuroimage* 53, 992-1000.
- Engel, J., Jr., Van Ness, P.C., Rasmussen, T., Ojemann, L.M., 1993. Outcome with respect to epileptic seizures. In: Engel, J., Jr. (Ed.), *Surgical treatment of the epilepsies*. Raven, New York, pp. 609-621.
- Evans, L.C., 2010. *Partial Differential Equations: Second Edition*. American Mathematical Society.
- Falconer, M.A., Serafetinides, E.A., Corsellis, J.A.N., 1964. Etiology and pathogenesis of temporal lobe epilepsy. *Arch Neurol* 10, 233-248.
- Falkai, P., Bogerts, B., 1986. Cell loss in the hippocampus of schizophrenics. *European Archives of Psychiatry and Clinical Neuroscience* 236, 154-161.
- Fernandez, G., Effenberger, O., Vinz, B., Steinlein, O., Elger, C.E., Döhring, W., Heinze, H.J., 1998. Hippocampal malformation as a cause of febrile convulsions and subsequent hippocampal sclerosis. *Neurology* 50, 909-917.
- Fischl, B., Salat, D.H., Busa, E., Albert, M., Dieterich, M., Haselgrove, C., van der, K.A., Killiany, R., Kennedy, D., Klaveness, S., Montillo, A., Makris, N., Rosen, B., Dale, A.M., 2002. Whole brain segmentation. Automated labeling of neuroanatomical structures in the human brain. *Neuron* 33, 341-355.

Fisher, R.S., Boas, W.v.E., Blume, W., Elger, C., Genton, P., Lee, P., Engel, J., 2005. Epileptic Seizures and Epilepsy: Definitions Proposed by the International League Against Epilepsy (ILAE) and the International Bureau for Epilepsy (IBE). *Epilepsia* 46, 470-472.

Fleiss, J.L., Levin, B., Paik, C.M., 2003. The measurement of interrater agreement *Statistical methods for rates and proportions*. John Wiley & Sons, Inc. , pp. 598-626.

Foresti, M.L., Arisi, G.M., Shapiro, L.A., 2011. Role of glia in epilepsy-associated neuropathology, neuroinflammation and neurogenesis. *Brain Res Rev* 66, 115-122.

Friston, K.J., Ashburner, J., Frith, C.D., Kitney, R.I., Poline, J.B., Heathcote, J.D., Frackowiak, R.S.J., 1995. Spatial registration and normalization of images. *Annual meeting of the Organization for Human Brain Mapping*.

Fuerst, D., Shah, J., Shah, A., Watson, C., 2003. Hippocampal sclerosis is a progressive disorder: a longitudinal volumetric MRI study. *Ann Neurol* 53, 413-416.

Gerig, G., Styner, M., Jones, D., Weinberg, D.R., Lieberman, J., 2001. Shape analysis of brain ventricles using SPHARM. *MMBIA*, 171-178.

Ghanei, A., Soltanian-Zadeh, H., Windham, J.P., 1998. Segmentation of the hippocampus from brain MRI using deformable contours. *Comput.Med.Imaging Graph.* 22, 203-216.

Gloor, P., 1997. *The temporal lobe and limbic system*. Oxford University Press, New York.

Gloveli, T., Schmitz, D., Heinemann, U., 1998. Interaction between superficial layers of the entorhinal cortex and the hippocampus in normal and epileptic temporal lobe. *Epilepsy Res* 32, 183-193.

Gogtay, N., Lu, A., Leow, A.D., Klunder, A.D., Lee, A.D., Chavez, A., Greenstein, D., Giedd, J.N., Toga, A.W., Rapoport, J.L., Thompson, P.M., 2008. Three-dimensional brain growth abnormalities in childhood-onset schizophrenia visualized by using tensor-based morphometry. *Proceedings of the National Academy of Sciences* 105, 15979-15984.

Good, C.D., Johnsrude, I.S., Ashburner, J., Henson, R.N., Friston, K.J., Frackowiak, R.S., 2001. A voxel-based morphometric study of ageing in 465 normal adult human brains. *Neuroimage* 14, 21-36.

Gould, E., Tanapat, P., 1999. Stress and hippocampal neurogenesis. *Biol Psychiatry* 46, 1472-1479.

Gousias, I.S., Rueckert, D., Heckemann, R.A., Dyet, L.E., Boardman, J.P., Edwards, A.D., Hammers, A., 2008. Automatic segmentation of brain MRIs of 2-year-olds into 83 regions of interest. *Neuroimage* 40, 672-684.

Grigorescu, S.E., Petkov, N., Kruizinga, P., 2002. Comparison of texture features based on Gabor filters. *IEEE Trans. Image Process* 11, 1160-1167.

Guizard, N., Fonov, V., Collins, D.L., 2009. Symmetric optimization scheme versus constrained symmetrization for non-linear registrations. MICCAI workshop on "Medical Image Analysis on Multiple Sclerosis (validation and methodological issues)".

Hammers, A., Heckemann, R., Koepp, M.J., Duncan, J.S., Hajnal, J.V., Rueckert, D., Aljabar, P., 2007. Automatic detection and quantification of hippocampal atrophy on MRI in temporal lobe epilepsy: A proof-of-principle study. *Neuroimage* 36, 38-47.

Han, X., Jovicich, J., Salat, D., van der Kouwe, A., Quinn, B., Czanner, S., Busa, E., Pacheco, J., Albert, M., Killiany, R., Maguire, P., Rosas, D., Makris, N., Dale, A., Dickerson, B., Fischl, B., 2006. Reliability of MRI-derived measurements of human cerebral cortical thickness: The effects of field strength, scanner upgrade and manufacturer. *Neuroimage* 32, 180-194.

Heckemann, R.A., Hajnal, J.V., Aljabar, P., Rueckert, D., Hammers, A., 2006. Automatic anatomical brain MRI segmentation combining label propagation and decision fusion. *Neuroimage* 33, 115-126.

Heckemann, R.A., Keihaninejad, S., Aljabar, P., Rueckert, D., Hajnal, J.V., Hammers, A., 2010. Improving intersubject image registration using tissue-class information benefits robustness and accuracy of multi-atlas based anatomical segmentation. *Neuroimage* 51, 221-227.

Hines, M., 1922. Studies in the growth and differentiation of the telencephalon in man. The fissura hippocampi. *J Comp Neurol* 34, 73-171.

Ho, B.C., Magnotta, V., 2010. Hippocampal volume deficits and shape deformities in young biological relatives of schizophrenia probands. *Neuroimage* 49, 3385-3393.

Hogan, R.E., Carne, R.P., Kilpatrick, C.J., Cook, M.J., Patel, A., King, L., O'Brien, T.J., 2008. Hippocampal deformation mapping in MRI negative PET positive temporal lobe epilepsy. *Journal of Neurology, Neurosurgery & Psychiatry* 79, 636-640.

Hogan, R.E., Wang, L., Bertrand, M.E., Willmore, L.J., Bucholz, R.D., Nassif, A.S., Csernansky, J.G., 2004. MRI-based high-dimensional hippocampal mapping in mesial temporal lobe epilepsy. *Brain* 127, 1731-1740.

Hogan, R.E., Wang, L., Bertrand, M.E., Willmore, L.J., Bucholz, R.D., Nassif, A.S., Csernansky, J.G., 2006. Predictive Value of Hippocampal MR Imaging-Based High-Dimensional Mapping in Mesial Temporal Epilepsy: Preliminary Findings. *AJNR Am J Neuroradiol* 27, 2149-2154.

Hudson, L.P., Munoz, D.G., Miller, L., McLachlan, R.S., Girvin, J.P., Blume, W.T., 1993. Amygdaloid sclerosis in temporal lobe epilepsy. *Ann Neurol* 33, 622-631.

Humphrey, T., 1967. The development of the human hippocampal fissure. *J Anat* 101, 655-676.

Insausti, A.M., Amaral, D.G., 2004. Hippocampal formation. In: Paxinos, G., Mai, J.K. (Eds.), *The human nervous system*. Elsevier, San Diego, pp. 871-914.

Insausti, R., Juottonen, K., Soininen, H., Insausti, A.M., Partanen, K., Vainio, P., Laakso, M.P., Pitkanen, A., 1998. MR volumetric analysis of the human entorhinal, perirhinal, and temporopolar cortices. *AJNR Am J Neuroradiol* 19, 659-671.

Insausti, R., Tunon, T., Sobreviela, T., Insausti, A.M., Gonzalo, L.M., 1995. The human entorhinal cortex: a cytoarchitectonic analysis. *J Comp Neurol* 355, 171-198.

Jack, C.R., Jr., Sharbrough, F.W., Cascino, G.D., Hirschorn, K.A., O'Brien, P.C., Marsh, W.R., 1992. Magnetic resonance imaging-based hippocampal volumetry: correlation with outcome after temporal lobectomy. *Ann Neurol* 31, 138-146.

Jackson, G.D., Berkovic, S.F., Duncan, J.S., Connelly, A., 1993a. Optimizing the diagnosis of hippocampal sclerosis using MR imaging. *AJNR* 14, 753-762.

Jackson, G.D., Berkovic, S.F., Tress, B.M., Kalnins, R.M., Fabinyi, G.C., Bladin, P.F., 1990. Hippocampal sclerosis can be reliably detected by magnetic resonance imaging. *Neurology* 40, 1869-1875.

Jackson, G.D., Connelly, A., Duncan, J.S., Gr?ewald, R.A., Gadian, D.G., 1993b. Detection of hippocampal pathology in intractable partial epilepsy: increased sensitivity with quantitative resonance T2 relaxometry. *Neurology* 43, 1793-1799.

Jackson, G.D., Kuzniecky, R.I., Cascino, G.D., 1994. Hippocampal sclerosis without detectable hippocampal atrophy. *Neurology* 44, 42-46.

Jenkinson, M., Smith, S., 2001. A global optimisation method for robust affine registration of brain images. *Medical Image Analysis* 5, 143-156.

Jernigan, T.L., Trauner, D.A., Hesselink, J.R., Tallal, P.A., 1991. Maturation of human cerebrum observed in vivo during adolescence. *Brain* 114 (Pt 5), 2037-2049.

Joshi, S., Pizer, S., Fletcher, P.T., Yushkevich, P., Thall, A., Marron, J.S., 2002. Multiscale deformable model segmentation and statistical shape analysis using medial descriptions. *IEEE Trans Med Imaging* 21, 538-550.

Jou, R.J., Hardan, A.Y., Keshavan, M.S., 2005. Reduced cortical folding in individuals at high risk for schizophrenia: a pilot study. *Schizophr Res* 75, 309-313.

Jutila, L., Ylinen, A., Partanen, K., Alafuzoff, I., Mervaala, E., Partanen, J., Vapalahti, M., Vainio, P., Pitkanen, A., 2001. MR volumetry of the entorhinal, perirhinal, and temporopolar cortices in drug-refractory temporal lobe epilepsy. *AJNR Am J Neuroradiol* 22, 1490-1501.

Kang, T.C., Kim, D.S., Kwak, S.E., Kim, J.E., Won, M.H., Kim, D.W., Choi, S.Y., Kwon, O.S., 2006. Epileptogenic roles of astroglial death and regeneration in the dentate gyrus of experimental temporal lobe epilepsy. *Glia* 54, 258-271.

Kelemen, A., Szekely, G., Gerig, G., 1999. Elastic model-based segmentation of 3-D neuroradiological data sets. *IEEE Trans Med Imaging* 18, 828-839.

Keller, S.S., Roberts, N., 2008. Voxel-based morphometry of temporal lobe epilepsy: An introduction and review of the literature. *Epilepsia* 49, 741-757.

Keller, S.S., Wilke, M., Wiesmann, U.C., Sluming, V.A., Roberts, N., 2004. Comparison of standard and optimized voxel-based morphometry for analysis of brain changes associated with temporal lobe epilepsy. *Neuroimage* 23, 860-868.

Khan, A.R., Wang, L., Beg, M.F., 2008. FreeSurfer-initiated fully-automated subcortical brain segmentation in MRI using Large Deformation Diffeomorphic Metric Mapping. *Neuroimage* 41, 735-746.

Kikinis, R., Shenton, M.E., Gerig, G., Hokama, H., Haimson, J., O'Donnell, B.F., Wible, C.G., McCarley, R.W., Jolesz, F.A., 1994. Temporal lobe sulco-gyral pattern anomalies in schizophrenia: an in vivo MR three-dimensional surface rendering study. *Neurosci Lett* 182, 7-12.

Kim, H., Bernasconi, N., Bernhardt, B., Colliot, O., Bernasconi, A., 2006. Quantitative analysis of shape and positioning of the hippocampal formation in patients with temporal lobe epilepsy. *Epilepsia* 47, 72.

Kim, H., Bernasconi, N., Bernhardt, B., Colliot, O., Bernasconi, A., 2008a. Basal temporal sulcal morphology in healthy controls and patients with temporal lobe epilepsy. *Neurology* 70, 2159-2165.

Kim, H., Besson, P., Colliot, O., Bernasconi, A., Bernasconi, N., 2008b. Surface-based vector analysis using heat equation interpolation: a new approach to quantify local hippocampal volume changes. *Med Image Comput Comput Assist Interv* 5241, 1008-1015.

King, D., Spencer, S.S., Bouthillier, A., Kim, J., de Lanerolle, N.C., Bronen, R.A., McCarthy, G., Luby, M., Spencer, D.D., 1996. Medial temporal lobe epilepsy without hippocampal atrophy. *J Epilepsy* 9, 291-297.

Kippenhan, J.S., Olsen, R.K., Mervis, C.B., Morris, C.A., Kohn, P., Meyer-Lindenberg, A., Berman, K.F., 2005. Genetic contributions to human gyrification: sulcal morphometry in Williams syndrome. *J Neurosci* 25, 7840-7846.

Kiwiel, K.C., 2001. Convergence and efficiency of subgradient methods for quasiconvex minimization. *Mathematical Programming* 90, 1-25.

Kobayashi, K., 2009. Targeting the Hippocampal Mossy Fiber Synapse for the Treatment of Psychiatric Disorders. *Molecular Neurobiology* 39, 24-36.

Kochunov, P., Mangin, J.F., Coyle, T., Lancaster, J., Thompson, P.M., Riviere, D., Cointepas, Y., Regis, J., Schlosser, A., Royall, D.R., Zilles, K., Mazziotta, J., Toga, A., Fox, P.T., 2005. Age-related morphology trends of cortical sulci. *Human Brain Mapping* 26, 210-220.

Konrad, C., Ukas, T., Nebel, C., Arolt, V., Toga, A.W., Narr, K.L., 2009. Defining the human hippocampus in cerebral magnetic resonance images--an overview of current segmentation protocols. *Neuroimage* 47, 1185-1195.

Kuchukhidze, G., Koppelstaetter, F., Unterberger, I., Dobesberger, J., Walser, G., Zamarian, L., Haberlandt, E., Maier, H., Ortler, M., Gotwald, T., Gelpi, E., Czech, T., Feucht, M., Bauer, G., Delazer, M., Felber, S., Trinka, E., 2010. Hippocampal abnormalities in malformations of cortical development. *Neurology* 74, 1575-1582.

Kulynych, J.J., Luevano, L.F., Jones, D.W., Weinberger, D.R., 1997. Cortical abnormality in schizophrenia: an in vivo application of the gyrification index. *Biol Psychiatry* 41, 995-999.

Kuzniecky, R., Bilir, E., Gilliam, F., Faught, E., Martin, R., Hugg, J., 1999. Quantitative MRI in temporal lobe epilepsy: evidence for fornix atrophy. *Neurology* 53, 496-501.

Lötjönen, J., Wolz, R., Koikkalainen, J., Julkunen, V., Thurfjell, L., Lundqvist, R., Waldemar, G., Soininen, H., Rueckert, D., 2011. Fast and robust extraction of hippocampus from MR images for diagnostics of Alzheimer's disease. *Neuroimage* 56, 185-196.

Lau, J.C., Lerch, J.P., Sled, J.G., Henkelman, R.M., Evans, A.C., Bedell, B.J., 2008. Longitudinal neuroanatomical changes determined by deformation-based morphometry in a mouse model of Alzheimer's disease. *Neuroimage* 42, 19-27.

Le Goualher, G., Argenti, A.M., Duyme, M., Baare, W.F., Hulshoff Pol, H.E., Boomsma, D.I., Zouaoui, A., Barillot, C., Evans, A.C., 2000. Statistical sulcal shape comparisons: application to the detection of genetic encoding of the central sulcus shape. *Neuroimage*. 11, 564-574.

Le Goualher, G., Procyk, E., Collins, D.L., Venugopal, R., Barillot, C., Evans, A.C., 1999. Automated extraction and variability analysis of sulcal neuroanatomy. *IEEE Trans Med Imaging* 18, 206-217.

Lee, S., Wolberg, G., Shin, S.Y., 1997. Scattered Data Interpolation with Multilevel B-Splines. *Ieee Transactions on Visualization and Computer Graphics* 3, 228-244.

Leung, K.K., Barnes, J., Ridgway, G.R., Bartlett, J.W., Clarkson, M.J., Macdonald, K., Schuff, N., Fox, N.C., Ourselin, S., 2010. Automated cross-sectional and longitudinal hippocampal volume measurement in mild cognitive impairment and Alzheimer's disease. *Neuroimage* 51, 1345-1359.

Leventon, M., Grimson, E., Faugeras, O., 2000. Statistical shape influence in geodesic active contours. *IEEE Trans Med Imaging* 21, 525-537.

Levitt, J.G., Blanton, R.E., Smalley, S., Thompson, P.M., Guthrie, D., McCracken, J.T., Sadoun, T., Heinichen, L., Toga, A.W., 2003. Cortical sulcal maps in autism. *Cereb Cortex* 13, 728-735.

Lohmann, G., von Cramon, D.Y., Steinmetz, H., 1999. Sulcal variability of twins. *Cereb Cortex* 9, 754-763.

Lord, C., Cook, E.H., Leventhal, B.L., Amaral, D.G., 2000. Autism Spectrum Disorders. *Neuron* 28, 355-363.

Lotjonen, J.M., Wolz, R., Koikkalainen, J.R., Thurfjell, L., Waldemar, G., Soininen, H., Rueckert, D., 2010. Fast and robust multi-atlas segmentation of brain magnetic resonance images. *Neuroimage* 49, 2352-2365.

Luders, E., Narr, K.L., Thompson, P.M., Rex, D.E., Jancke, L., Steinmetz, H., Toga, A.W., 2004. Gender differences in cortical complexity. *Nat Neurosci* 7, 799-800.

Macchi, G., 1951. The ontogenetic development of the olfactory telencephalon in man. *J Comp Neurol* 95, 245-305.

MacMaster, F., Kusumakar, V., 2004. Hippocampal volume in early onset depression. *BMC Medicine* 2, 2.

Malladi, R., Sethian, J., Vemuri, B., 1995. Shape modelling with front-propagation: a level set approach. *IEEE Transaction on Pattern Analysis and Machine Intelligence* 17, 158-175.

Mangin, J.F., Frouin, V., Bloch, I., Regis, J., Lopez-Krahe, J., 1995. From 3D magnetic resonance images to structural representations of the cortex topography using topology preserving deformations. *J Math Imag and Vision* 5, 297-318.

Mangin, J.F., Riviere, D., Cachia, A., Duchesnay, E., Cointepas, Y., Papadopoulos-Orfanos, D., Scifo, P., Ochiai, T., Brunelle, F., Regis, J., 2004. A framework to study the cortical folding patterns. *Neuroimage* 23 Suppl 1, S129-138.

Margerison, J.H., Corsellis, J.A., 1966. Epilepsy and the temporal lobes. A clinical, electroencephalographic and neuropathological study of the brain in epilepsy, with particular reference to the temporal lobes. *Brain* 89, 499-530.

Mathern, G.W., Leiphart, J.L., De Vera, A., Adelson, P.D., Seki, T., Nader, L., Leite, J.P., 2002. Seizures Decrease Postnatal Neurogenesis and Granule Cell Development in the Human Fascia tDentata. *Epilepsia* 43, 68-73.

Mazziotta, J.C., Toga, A.W., Evans, A., Fox, P., Lancaster, J., 1995. A probabilistic atlas of the human brain: theory and rationale for its development. The International Consortium for Brain Mapping (ICBM). *Neuroimage*. 2, 89-101.

McIntosh, A.M., Wilson, S.J., Berkovic, S.F., 2001. Seizure outcome after temporal lobectomy: current research practice and findings. *Epilepsia* 42, 1288-1307.

Meencke, H.J., Veith, G., 1991. Hippocampal sclerosis in epilepsy. In: Lüders, H. (Ed.), *Epilepsy Surgery*. Raven Press, New York, pp. 705-715.

Miettinen, R., Kotti, T., Tuunanen, J., Toppinen, A., Riekkinen, P., Sr, Halonen, T., 1998. Hippocampal damage after injection of kainic acid into the rat entorhinal cortex. *Brain Res* 813, 9-17.

Milner, B., 1971. Interhemispheric differences in the localization of psychological processes in man. *Br Med Bull* 27, 272-277.

Mima, T., Mikawa, T., 2004. Folding of the tectal cortex by local remodeling of neural differentiation. *Dev Dyn* 229, 475-479.

Mohr, A., Weisbrod, M., Schellinger, P., Knauth, M., 2004. The similarity of brain morphology in healthy monozygotic twins. *Brain Res Cogn Brain Res* 20, 106-110.

Molko, N., Cachia, A., Riviere, D., Mangin, J.F., Bruandet, M., Le Bihan, D., Cohen, L., Dehaene, S., 2003. Functional and structural alterations of the intraparietal sulcus in a developmental dyscalculia of genetic origin. *Neuron*, (in press).

Molko, N., Cachia, A., Riviere, D., Mangin, J.F., Bruandet, M., LeBihan, D., Cohen, L., Dehaene, S., 2004. Brain anatomy in Turner syndrome: evidence for impaired social and spatial-numerical networks. *Cereb Cortex* 14, 840-850.

Montenegro, M.A., Kinay, D., Cendes, F., Bernasconi, A., Bernasconi, N., Coan, A.C., Li, L.M., Guerreiro, M.M., Guerreiro, C.A., Lopes-Cendes, I., Andermann, E., Dubeau, F., Andermann, F., 2006. Patterns of hippocampal abnormalities in malformations of cortical development. *J Neurol Neurosurg Psychiatry* 77, 367-371.

Morey, R.A., Petty, C.M., Xu, Y., Pannu Hayes, J., Wagner li, H.R., Lewis, D.V., LaBar, K.S., Styner, M., McCarthy, G., 2009. A comparison of automated segmentation and manual tracing for quantifying hippocampal and amygdala volumes. *Neuroimage* 45, 855-866.

Morra, J.H., Tu, Z., Apostolova, L.G., Green, A.E., Avedissian, C., Madsen, S.K., Parikshak, N., Hua, X., Toga, A.W., Jack Jr, C.R., Weiner, M.W., Thompson, P.M., 2008. Validation of a fully automated 3D hippocampal segmentation method using subjects with Alzheimer's disease mild cognitive impairment, and elderly controls. *Neuroimage* 43, 59-68.

Morra, J.H., Tu, Z., Apostolova, L.G., Green, A.E., Avedissian, C., Madsen, S.K., Parikshak, N., Hua, X., Toga, A.W., Jr., C.R.J., Schuff, N., Weiner, M.W.,

Thompson, P.M., Initiative, a.t.A.s.D.N., 2009. Automated 3D mapping of hippocampal atrophy and its clinical correlates in 400 subjects with Alzheimer's disease, mild cognitive impairment, and elderly controls. *Human Brain Mapping* 30, 2766-2788.

Morra, J.H., Tu, Z., Apostolova, L.G., Green, A.E., Toga, A.W., Thompson, P.M., 2010. Comparison of AdaBoost and support vector machines for detecting Alzheimer's disease through automated hippocampal segmentation. *IEEE Trans Med Imaging* 29, 30-43.

Muntaner, L., Perez-Ferron, J.J., Herrera, M., Rosell, J., Taboada, D., Climent, S., 1997. MRI of a family with focal abnormalities of gyration. *Neuroradiology* 39, 605-608.

Narr, K.L., Thompson, P.M., Szeszko, P., Robinson, D., Jang, S., Woods, R.P., Kim, S., Hayashi, K.M., Asuncion, D., Toga, A.W., Bilder, R.M., 2004. Regional specificity of hippocampal volume reductions in first-episode schizophrenia. *Neuroimage* 21, 1563-1575.

Nicolson, R., DeVito, T.J., Vidal, C.N., Sui, Y., Hayashi, K.M., Drost, D.J., Williamson, P.C., Rajakumar, N., Toga, A.W., Thompson, P.M., 2006. Detection and mapping of hippocampal abnormalities in autism. *Psychiatry Research: Neuroimaging* 148, 11-21.

Novak, K., Czech, T., Prayer, D., Dietrich, W., Serles, W., Lehr, S., Baumgartner, C., 2002. Individual variations in the sulcal anatomy of the basal temporal lobe and its relevance for epilepsy surgery: an anatomical study performed using magnetic resonance imaging. *J Neurosurg* 96, 464-473.

O'Brien, T.J., So, E.L., Meyer, F.B., Parisi, J.E., Jack, C.R., 1999. Progressive hippocampal atrophy in chronic intractable temporal lobe epilepsy. *Ann.Neurol.* 45, 526-529.

Ochiai, T., Grimault, S., Scavarda, D., Roch, G., Hori, T., Riviere, D., Mangin, J.F., Regis, J., 2004. Sulcal pattern and morphology of the superior temporal sulcus. *Neuroimage* 22, 706-719.

Ono, M., Kubik, S., Abernethy, C.D., 1990. Atlas of the cerebral sulci. Georg Thieme Verlag, Stuttgart.

Palmini, A., Najm, I., Avanzini, G., Babb, T., Guerrini, R., Foldvary-Schaefer, N., Jackson, G., Luders, H.O., Prayson, R., Spreafico, R., Vinters, H.V., 2004. Terminology and classification of the cortical dysplasias. *Neurology* 62, S2-8.

Paradisi, M., Fernandez, M., Del Vecchio, G., Lizzo, G., Marucci, G., Giulioni, M., Pozzati, E., Antonelli, T., Lanzoni, G., Bagnara, G.P., Giardino, L., Calza, L., 2010. Ex vivo study of dentate gyrus neurogenesis in human pharmacoresistant temporal lobe epilepsy. *Neuropathol Appl Neurobiol* 36, 535-550.

Paragios, N., 2002. Geodesic Active Regions and Level Set Methods for Supervised Texture Segmentation.

Pardoe, H.R., Pell, G.S., Abbott, D.F., Jackson, G.D., 2009. Hippocampal volume assessment in temporal lobe epilepsy: How good is automated segmentation? *Epilepsia* 50.

Parent, J.M., 2008. Persistent hippocampal neurogenesis and epilepsy. *Epilepsia* 49 Suppl 5, 1-2.

Pegues, M.P., Rogers, L.J., Amend, D., Vinogradov, S., Deicken, R.F., 2003. Anterior hippocampal volume reduction in male patients with schizophrenia. *Schizophrenia Research* 60, 105-115.

Pieperhoff, P., S?meyer, M., H?ke, L., Zilles, K., Schnitzler, A., Amunts, K., 2008. Detection of structural changes of the human brain in longitudinally acquired MR images by deformation field morphometry: Methodological analysis, validation and application. *Neuroimage* 43, 269-287.

Pitiot, A., Delingette, H., Thompson, P.M., Ayache, N., 2004. Expert knowledge-guided segmentation system for brain MRI. *Neuroimage* 23, S85-S96.

Pluta, J., Avants, B.B., Glynn, S., Awate, S., Gee, J.C., Detre, J.A., 2009. Appearance and incomplete label matching for diffeomorphic template based hippocampus segmentation. *Hippocampus* 19, 565-571.

Pohl, K.M., Bouix, S., Nakamura, M., Rohlfing, T., McCarley, R.W., Kikinis, R., Grimson, W.E.L., Shenton, M.E., Wells, W.M., 2007. A Hierarchical Algorithm for MR Brain Image Parcellation. *Medical Imaging, IEEE Transactions on* 26, 1201-1212.

Posener, J.A., Wang, L., Price, J.L., Gado, M.H., Province, M.A., Miller, M.I., Babb, C.M., Csernansky, J.G., 2003. High-dimensional mapping of the hippocampus in depression. *Am J Psychiatry* 160, 83-89.

Powell, S.B., 2010. Models of neurodevelopmental abnormalities in schizophrenia. *Curr Top Behav Neurosci* 4, 435-481.

Pruessner, J.C., Kohler, S., Crane, J., Pruessner, M., Lord, C., Byrne, A., Kabani, N., Collins, D.L., Evans, A.C., 2002. Volumetry of temporopolar, perirhinal, entorhinal and parahippocampal cortex from high-resolution MR images: considering the variability of the collateral sulcus. *Cereb Cortex* 12, 1342-1353.

Rakic, P., 1988. Defects of neuronal migration and the pathogenesis of cortical malformations. *Prog. Brain Res.* 73, 15-37.

Raymond, A.A., Fish, D.R., Sisodiya, S.M., Alsanjari, N., Stevens, J.M., Shorvon, S.D., 1995. Abnormalities of gyration, heterotopias, tuberous sclerosis, focal cortical dysplasia, microdysgenesis, dysembryoplastic neuroepithelial tumor and dysgenesis of archicortex in epilepsy. Clinical, EEG and neuroimaging features in 100 adult patients. *Brain* 118, 629-660.

Riviere, D., Mangin, J.F., Papadopoulos-Orfanos, D., Martinez, J.M., Frouin, V., Regis, J., 2002. Automatic recognition of cortical sulci of the human brain using a congregation of neural networks. *Med Image Anal* 6, 77-92.

Roch, C., Leroy, C., Nehlig, A., Namer, Izzie J., 2002. Predictive Value of Cortical Injury for the Development of Temporal Lobe Epilepsy in 21-day-old Rats: An MRI Approach Using the Lithium-pilocarpine Model. *Epilepsia* 43, 1129-1136.

Rohlfing, T., Brandt, R., Menzel, R., Maurer, C.R., 2004. Evaluation of atlas selection strategies for atlas-based image segmentation with application to confocal microscopy images of bee brains. *Neuroimage* 21, 1428-1442.

Rosin, P., 2003. Measuring shape: ellipticity, rectangularity, and triangularity. *Machine Vision and Applications* 14, 172-184.

Sagar, H.J., Oxbury, J.M., 1987. Hippocampal neuron loss in temporal lobe epilepsy: correlation with early childhood convulsions. *Ann.Neurol.* 22, 334-340.

Sallet, P.C., Elkis, H., Alves, T.M., Oliveira, J.R., Sassi, E., Campi de Castro, C., Busatto, G.F., Gattaz, W.F., 2003. Reduced cortical folding in schizophrenia: an MRI morphometric study. *Am J Psychiatry* 160, 1606-1613.

Salmond, C.H., Ashburner, J., Connelly, A., Friston, K.J., Gadian, D.G., Vargha-Khadem, F., 2005. The role of the medial temporal lobe in autistic spectrum disorders. *European Journal of Neuroscience* 22, 764-772.

Sato, N., Hatakeyama, S., Shimizu, N., Hikima, A., Aoki, J., Endo, K., 2001. MR evaluation of the hippocampus in patients with congenital malformations of the brain. *AJNR Am J Neuroradiol* 22, 389-393.

Schaer, M., Schmitt, J.E., Glaser, B., Lazeyras, F., Delavelle, J., Eliez, S., 2006. Abnormal patterns of cortical gyrification in velo-cardio-facial syndrome (deletion 22q11.2): an MRI study. *Psychiatry Res* 146, 1-11.

Scharfman, H.E., McCloskey, D.P., 2009. Postnatal neurogenesis as a therapeutic target in temporal lobe epilepsy. *Epilepsy Res* 85, 150-161.

Schramm, J., Clusmann, H., 2008. The surgery of epilepsy. *Neurosurgery* 62 Suppl 2, 463-481; discussion 481.

Schwarcz, R., Witter, M.P., 2002. Memory impairment in temporal lobe epilepsy: the role of entorhinal lesions. *Epilepsy Res* 50, 161-177.

Seber, G.A.F., 1984. *Multivariate Observations*. John Wiley & Sons Inc.

Seidenberg, M., Kelly, K.G., Parrish, J., Geary, E., Dow, C., Rutecki, P., Hermann, B., 2005. Ipsilateral and contralateral MRI volumetric abnormalities in chronic unilateral temporal lobe epilepsy and their clinical correlates. *Epilepsia* 46, 420-430.

Shapiro, L.A., Korn, M.J., Ribak, C.E., 2005. Newly generated dentate granule cells from epileptic rats exhibit elongated hilar basal dendrites that align along GFAP-immunolabeled processes. *Neuroscience* 136, 823-831.

Shen, D., Moffat, S., Resnick, S.M., Davatzikos, C., 2002. Measuring size and shape of the hippocampus in MR images using a deformable shape model. *Neuroimage* 15, 422-434.

Shenton, M.E., Gerig, G., McCarley, R.W., Szekely, G., Kikinis, R., 2002. Amygdala-hippocampal shape differences in schizophrenia: the application of 3D shape models to volumetric MR data. *Psychiatry Res* 115, 15-35.

Siebzehnruhl, F.A., Blumcke, I., 2008. Neurogenesis in the human hippocampus and its relevance to temporal lobe epilepsies. *Epilepsia* 49 Suppl 5, 55-65.

Silva, I., Lin, K., Jackowski, A.P., Centeno, R.d.S., Pinto, M.L., Carrete Jr, H., Yacubian, E.M., Amado, D., 2010. Absence of gender effect on amygdala volume in temporal lobe epilepsy. *Epilepsy & Behavior* 19, 501-503.

Sled, J.G., Zijdenbos, A.P., Evans, A.C., 1998. A nonparametric method for automatic correction of intensity nonuniformity in MRI data. *IEEE Trans Med Imaging* 17, 87-97.

Sloviter, R.S., Kudrimoti, H.S., Laxer, K.D., Barbaro, N.M., Chan, S., Hirsch, L.J., Goodman, R.R., Pedley, T.A., 2004. "Tectonic" hippocampal malformations in patients with temporal lobe epilepsy. *Epilepsy Research* 59, 123-153.

Sloviter, R.S., Pedley, T.A., 1998. Subtle hippocampal malformation: importance in febrile seizures and development of epilepsy. *Neurology* 50, 846-849.

Smith, S.M., 2002. Fast robust automated brain extraction. *Hum Brain Mapp* 17, 143-155.

Sommer, W., 1880. Erkrankung des Ammonshorns als aetiologisches Moment der Epilepsie. *Arch Psychiatrie Nervenkr* 10, 631-675.

Sowell, E.R., Thompson, P.M., Rex, D., Kornsand, D., Tessner, K.D., Jernigan, T.L., Toga, A.W., 2002. Mapping sulcal pattern asymmetry and local cortical surface gray matter distribution in vivo: maturation in perisylvian cortices. *Cereb.Cortex* 12, 17-26.

Spivak, M., 1999. A comprehensive introduction to differential geometry (3rd edition). Clothbound.

Steinmetz, H., Herzog, A., Schlaug, G., Huang, Y., Jancke, L., 1995. Brain (A) symmetry in monozygotic twins. *Cereb Cortex* 5, 296-300.

Stiers, P., Fonteyne, A., Wouters, H., D'Agostino, E., Sunaert, S., Lagae, L., 2010. Hippocampal malrotation in pediatric patients with epilepsy associated with complex prefrontal dysfunction. *Epilepsia* 51, 546-555.

Styner, M., Gerig, G., Lieberman, J., Jones, D., Weinberger, D., 2003. Statistical shape analysis of neuroanatomical structures based on medial models. *Medical Image Analysis* 7, 207-220.

Styner, M., Lieberman, J.A., Pantazis, D., Gerig, G., 2004. Boundary and medial shape analysis of the hippocampus in schizophrenia. *Medical Image Analysis* 8, 197-203.

Styner, M., Oguz, I., Xu, S., Brechbühler, C., Pantazis, D., Gerig, G., 2006. Statistical Shape Analysis of Brain Structures using SPHARM-PDM. MICCAI 2006 Opensource workshop.

Sutula, T.P., 2004. Mechanisms of epilepsy progression: current theories and perspectives from neuroplasticity in adulthood and development. *Epilepsy Res* 60, 161-171.

Tasch, E., Cendes, F., Li, L.M., Dubeau, F., Andermann, F., Arnold, D.L., 1999. Neuroimaging evidence of progressive neuronal loss and dysfunction in temporal lobe epilepsy. *Ann Neurol* 45, 568-576.

Tassi, L., Colombo, N., Garbelli, R., Francione, S., Lo, R.G., Mai, R., Cardinale, F., Cossu, M., Ferrario, A., Galli, C., Bramerio, M., Citterio, A., Spreafico, R., 2002. Focal cortical dysplasia: neuropathological subtypes, EEG, neuroimaging and surgical outcome. *Brain* 125, 1719-1732.

Theodore, W.H., Bhatia, S., Hatta, J., Fazilat, S., DeCarli, C., Bookheimer, S.Y., Gaillard, W.D., 1999. Hippocampal atrophy, epilepsy duration, and febrile seizures in patients with partial seizures. *Neurology* 52, 132-136.

Thom, M., Liagkouras, I., Elliot, K.J., Martinian, L., Harkness, W., McEvoy, A., Caboclo, L.O., Sisodiya, S.M., 2010. Reliability of patterns of hippocampal sclerosis as predictors of postsurgical outcome. *Epilepsia* 51, 1801-1808.

Thom, M., Sisodiya, S.M., Beckett, A., Martinian, L., Lin, W.R., Harkness, W., Mitchell, T.N., Craig, J., Duncan, J., Scaravilli, F., 2002a. Cytoarchitectural abnormalities in hippocampal sclerosis. *J Neuropathol Exp Neurol* 61, 510-519.

Thom, M., Sisodiya, S.M., Lin, W.R., Mitchell, T., Free, S.L., Stevens, J., Scaravilli, F., 2002b. Bilateral isolated hippocampal malformation in temporal lobe epilepsy. *Neurology* 58, 1683-1686.

Thompson, P.M., Giedd, J.N., Woods, R.P., MacDonald, D., Evans, A.C., Toga, A.W., 2000. Growth patterns in the developing brain detected by using continuum mechanical tensor maps. *Nature* 404, 190-193.

Thompson, P.M., Schwartz, C., Toga, A.W., 1996. High-resolution random mesh algorithms for creating a probabilistic 3D surface atlas of the human brain. *Neuroimage*. 3, 19-34.

Tosun, D., Dabbs, K., Caplan, R., Siddarth, P., Toga, A., Seidenberg, M., Hermann, B., 2011. Deformation-based morphometry of prospective neurodevelopmental changes in new onset paediatric epilepsy. *Brain* 134, 1003-1014.

Tsai, A., Yezzi, A., Jr., Wells, W., Tempany, C., Tucker, D., Fan, A., Grimson, W.E., Willsky, A., 2003. A shape-based approach to the segmentation of medical imagery using level sets. *Medical Imaging, IEEE Transactions on* 22, 137-154.

van der Lijn, F., den Heijer, T., Breteler, M.M.B., Niessen, W.J., 2008. Hippocampus segmentation in MR images using atlas registration, voxel classification, and graph cuts. *Neuroimage* 43, 708-720.

Van Essen, D.C., 1997. A tension-based theory of morphogenesis and compact wiring in the central nervous system. *Nature* 385, 313-318.

Van Hoesen, G.W., 2002. The human parahippocampal region in Alzheimer's disease, demential, and ageing. In: Witter, M.P., Wouterlood, F.G. (Eds.), *The parahippocampal region: organization and role in cognitivr function*. Oxford University Press, New York, pp. 271-295.

Van Hoesen, G.W., Hyman, B.T., J. Storm-Mathisen, J.Z., Ottersen, O.P., 1990. Hippocampal formation: anatomy and the patterns of pathology in Alzheimer's disease. *Progress in Brain Research*. Elsevier, pp. 445-457.

Van Paesschen, W., Duncan, J.S., Stevens, J.M., Connelly, A., 1998. Longitudinal quantitative hippocampal magnetic resonance imaging of adults with

newly diagnosed partial seizures - one year follow-up results. *Epilepsia* 39, 633-639.

Verity, C.M., 1998. Do seizures damage the brain? The epidemiological evidence. *Arch Dis Child* 78, 78-84.

Voets, N.L., Adcock, J.E., Stacey, R., Hart, Y., Carpenter, K., Matthews, P.M., Beckmann, C.F., 2009. Functional and structural changes in the memory network associated with left temporal lobe epilepsy. *Hum Brain Mapp* 30, 4070-4081.

Voets, N.L., Bernhardt, B.C., Kim, H., Yoon, U., Bernasconi, N., 2011. Increased temporolimbic cortical folding complexity in temporal lobe epilepsy. *Neurology* 76, 138-144.

Voss, K., Suesse, H., 1997. Invariant fitting of planar objects by primitives. *IEEE Transactions on Pattern Analysis and Machine Intelligence* 19, 80-84.

Wang, H., Das, S.R., Suh, J.W., Altinay, M., Pluta, J., Craige, C., Avants, B., Yushkevich, P.A., 2011. A learning-based wrapper method to correct systematic errors in automatic image segmentation: Consistently improved performance in hippocampus, cortex and brain segmentation. *Neuroimage* 55, 968-985.

Wang, L., Joshi, S.C., Miller, M.I., Csernansky, J.G., 2001. Statistical analysis of hippocampal asymmetry in schizophrenia. *Neuroimage* 14, 531-545.

Welker, W., 1990. Why does cerebral cortex fissure and fold? A review of determinants of gyri and sulci. In: Jones, E.G., Peters, A. (Eds.), *Cerebral cortex*. Plenum Press, New York, pp. 3-136.

Whitford, T.J., Grieve, S.M., Farrow, T.F.D., Gomes, L., Brennan, J., Harris, A.W.F., Gordon, E., Williams, L.M., 2007. Volumetric White Matter Abnormalities in First-Episode Schizophrenia: A Longitudinal, Tensor-Based Morphometry Study. *Am J Psychiatry* 164, 1082-1089.

Whitworth, A.B., Honeder, M., Kremser, C., Kemmler, G., Felber, S., Hausmann, A., Wanko, C., Wechdorn, H., Aichner, F., Stuppaeck, C.H., Wolfgang

Fleischhacker, W., 1998. Hippocampal volume reduction in male schizophrenic patients. *Schizophrenia Research* 31, 73-81.

Wiesel, T.N., 1982. Postnatal development of the visual cortex and the influence of environment. *Nature* 299, 583-591.

Wilke, M., Kowatch, R.A., DelBello, M.P., Mills, N.P., Holland, S.K., 2004. Voxel-based morphometry in adolescents with bipolar disorder: first results. *Psychiatry Res* 131, 57-69.

Witter, M.P., Wouterlood, F.G., Naber, P.A., Van Haeften, T., 2000. Anatomical organization of the parahippocampal-hippocampal network. *Ann N Y Acad Sci* 911, 1-24.

Wolf, H.K., Aliashkevich, A.F., Blumcke, I., Wiestler, O.D., Zentner, J., 1997. Neuronal loss and gliosis of the amygdaloid nucleus in temporal lobe epilepsy. A quantitative analysis of 70 surgical specimens. *Acta Neuropathol* 93, 606-610.

Wolf, H.K., Campos, M.G., Zentner, J., Hufnagel, A., Schramm, J., Elger, C.E., Wiestler, O.D., 1993. Surgical pathology of temporal lobe epilepsy. Experience with 216 cases. *J Neuropathol Exp Neurol* 52, 499-506.

Woods, R.P., Grafton, S.T., Holmes, C.J., Cherry, S.R., Mazziotta, J.C., 1998. Automated Image Registration: I. General Methods and Intrasubject, Intramodality Validation. *Journal of Computer Assisted Tomography* 22, 139-152.

Wozny, C., Gabriel, S., Jandova, K., Schulze, K., Heinemann, U., Behr, J., 2005. Entorhinal cortex entrains epileptiform activity in CA1 in pilocarpine-treated rats. *Neurobiology of Disease* 19, 451-460.

Yang, J., Duncan, J.S., 2004. 3D image segmentation of deformable objects with joint shape-intensity prior models using level sets. *Medical Image Analysis* 8, 285-294.

Yilmazer-Hanke, D.M., Wolf, H.K., Schramm, J., Elger, C.E., Wiestler, O.D., Blumcke, I., 2000. Subregional pathology of the amygdala complex and

entorhinal region in surgical specimens from patients with pharmaco-resistant temporal lobe epilepsy. *J.Neuropathol.Exp.Neurol.* 59, 907-920.

Yousry, T.A., Schmid, U.D., Alkadhi, H., Schmidt, D., Peraud, A., Buettner, A., Winkler, P., 1997. Localization of the motor hand area to a knob on the precentral gyrus. A new landmark. *Brain* 120, 141-157.

Zilles, K., Armstrong, E., Schleicher, A., Kretschmann, H.J., 1988. The human pattern of gyrification in the cerebral cortex. *Anat Embryol (Berl)* 179, 173-179.